INVESTIGATION OF HEAT TRANSFER IN DROPWISE CONDENSATION FACILITATED BY A HUMID AIRFLOW

MILAD SHAKERI BONAB

A DISSERTATION SUBMITTED TO
THE FACULTY OF GRADUATE STUDIES
IN PARTIAL FULFILLMENT OF THE REQUIREMENTS
FOR THE DEGREE OF
DOCTOR OF PHILOSOPHY

GRADUATE PROGRAM IN MECHANICAL ENGINEERING
YORK UNIVERSITY
TORONTO, ONTARIO
MARCH 2022

ABSTRACT

It is necessary to understand humid air condensation because of its various applications, such as water harvesting, and environment control and life support systems. Improvement of the heat transfer rate by facilitating condensate removal (shedding of droplets) from the surface can decrease operational costs. Droplets can be shed by using airflow. Parameters such as relative humidity (RH), airflow velocity, and subcooling (T_{sc}) play a substantial role in condensation and heat transfer rate. Therefore, understanding the effect of these parameters is essential to analyze and evaluate the performance of the systems reliant on condensation. Firstly, this work is dedicated to investigating the influence of airflow on the condensation heat transfer coefficient (HTC) of humid air on a horizontal surface. A mini closed-looped wind tunnel was used to simulate the condensation environment and control condensation parameters. Airflow velocities from 1 to 15 m/s were investigated because the condensate's shedding usually happens in this range. Also, an RH of 10–80% and T_{sc} of 0–10°C were used to achieve both single-phase and condensation regimes. Transient and instantaneous heat flux measurements were required to study the relationship between condensate morphology and HTC. To facilitate this, a transient inverse heat conduction method was used to characterize the time-varying surface heat flux and associated HTC. A 5-fold decrease in response time was found for the transient method compared to the steady-state method. The effect of condensation parameters on the HTC and the relationship between condensate morphology and HTC is discussed. The results show that HTC for the subcooling of T = 0°C is smaller than for other temperatures. Also, the effect of RH on condensation was investigated, and higher HTC was found for higher RHs. The results clearly show that the shedding of condensate kept the average droplet size low and doubled heat transfer performance improvement.

Shedding of droplets from a surface is critical part of the dropwise condensation process for improving heat transfer. Because gravity as a droplet removal technique is not available in space, the use of airflow to shed droplets can be considered for condensing heat exchangers in environmental control and life support systems. Different surface coatings can be used to reduce the energy requirements for this process. The adhesion of droplets that form because of condensation depends on surface properties and the condensing period. Therefore, this study also investigates the shedding kinematics of water droplets in a condensation environment when exposed to aerodynamic forces in microgravity. The experiments were performed at zero gravity in the 73rd European Space Agency (ESA) parabolic flight campaign framework. We tested four different surfaces (PMMA, PS, PTFE, and SHS) and various droplet sizes (80, 60, and 40 µL) to understand the effect of gravity on the shape-dislodging kinematics of droplets. First, the droplet shape was analyzed to understand shedding behaviour. A droplet in microgravity was shed in an airflow 7% lower than that necessary in normal gravity. Second, the effect of the droplet size was investigated for both microgravity and normal gravity; the shedding velocity was lower for microgravity, and it decreased according to the size of the droplet. Also, increasing hydrophobicity decreased critical velocity. As a result of lower adhesion and higher drag, droplets on a PTFE coating experienced lower shedding velocity. Finally, for superhydrophobic surfaces in microgravity, droplets were found to detach. The observational outcome from experiments is to determine the coating that provides the minimal required air velocity for the shedding of the droplets without causing the droplet to lift off the surface. Such knowledge allows us to properly design condensers that work under microgravity conditions and dropwise condensation mode. Therefore, this work also investigates the shedding kinematics of water droplets in a condensation environment when exposed to aerodynamic forces in microgravity.

Hydrophobic and superhydrophobic surfaces facilitate condensate mobility and lower resistance to shedding, resulting in dropwise condensation mode. However, these surfaces are fabricated by modifying the chemical or topographical patterning of the substrate passively to promote condensate mobility. Apart from passive approaches, an alternating (AC) electric field has been used to promote condensation heat transfer by actively controlling droplets dynamics. Lastly, this work investigates the influence of EW-based surfaces on droplet shedding and heat transfer enhancement during humid air condensation. A mini closed-looped wind tunnel was used to simulate the condensation environment and control condensation parameters. AC electric field with the frequencies of 1 and 10 kHz was applied and compared with the control case (no voltage). The transient inverse heat conduction method was used to determine HTC, and heat transfer measurements were synchronized to a high-resolution camera to monitor the condensation dynamics. The results show that the area-weighted average droplet radius was increased by 61% and 84% for 1 kHz and 10 kHz, respectively, compared to the control case for 1 m/s airflow. It can be clearly seen that the 10 kHz case results in shorter shedding time, which became significant by the airflow. Higher frequency for condensation due to lower shedding time increases heat transfer performance. In addition, HTC was found to be higher at 10 kHz in the presence of shedding, and the difference became significant for airflow of 15 m/s where the shedding is prominent, and HTC increased by 35% compared to the control case. This foundation may help one to use EW to improve heat transfer and condensate shedding under shear flow.

DEDICATION

سپاس بی کران پروردگار یکتا را که هستی مان بخشید و به طریق علم و دانش رهنمونمان شد و به همنشینی رهروان علم و دانش مفتخرمان نمود و خوشه چینی از علم و معرفت را روزیمان ساخت.

خدای را بسی شاکرم که از روی کرم پدر و مادری فداکار نصیبم ساخته تا در سایه درخت پربار وجودشان بیاسایم و از ریشه آنها شاخ و برگ گیرم و از سایه وجودشان در راه کسب علم و دانش تلاش نمایم.

با سپاس از سه وجود مقدس:

آنان که ناتوان شدند تا ما به توانایی برسیم...

موهایشان سپید شد تا ما روسفید شویم...

و عاشقانه سوختند تا گرمابخش وجود ما و روشنگر راهمان باشند...

پدرانمان

مادرانمان

استادانمان

****

To God Almighty, my creator, my strong pillar, my source of inspiration, wisdom, knowledge and understanding.

To my parents, whose prayers always surrounded me until I became what I am now. They were always with me through the journey of struggles and the moments of success.

And finally, to my family, friends and all who are proud of my achievements.

ACKNOWLEDGMENTS

When I decided to start my PhD journey, I had big question marks in my mind that how PhD life would look like, especially as an international student in a new country, and I was dreaming about it. Now, if I had this chance to go back and wish the best journey ever, I can not think better than what I had in the last four years. But, of course, it would not have been possible without the continuous support from my supervisors, committee members, colleagues, mentors, family, and friends. Therefore, I would like to take this opportunity to express my sincere gratitude to these wonderful people who made my lifelong dream of being a researcher become real.

First and foremost, I am incredibly grateful to my PhD supervisors, Prof. Alidad Amirfazli and Prof. Roger Kempers, for their invaluable advice, endless support, thoughtful comments, and patience throughout these past four years. Words cannot express how truly thankful I am for their efforts in cranking out this dissertation. Furthermore, it was my great honor to be part of two wonderful research groups and laboratories, SEiL (Surface Engineering and Instrumentation Lab) and TF-Lab (Thermo-Fluid Lab). Prof. Amirfazli and Prof. Kempers continuously encouraged and were always willing and enthusiastic to assist and support me in any way they could throughout my PhD journey and other sides of my life. THANK YOU!

I would like to thank my committee members, Prof. Thomas Cooper, and Prof. Hossam Sadek, for their constructive and informative feedback in my annual committee meetings. I also want to thank Prof. Shooka Karimpour for accepting my comprehensive examination's external referee. I am thankful to all the Mechanical Engineering faculty members for letting me be part of this fantastic department.

I am thankful to Prof. Qiu-Sheng Liu and his research group in the National Microgravity Laboratory at the Chinese Academy of Sciences for their excellent hospitality during my research internship in 2019. I learned to be gentle, kind, supportive, helpful, and a dedicated and hardworking researcher. I also acknowledge the China Manned Space Agency for their financial support of the international collaborative project.

I would like to express my deep appreciation to Prof. Carlo Saverio Iorio and his research group in the Microgravity Research Center at the Université libre de Bruxelles for their excellent hosting during my research internship in 2020. Prof. Iorio is a great mentor, supportive, helpful and kind. Also, I was honoured to be one of the participants in the 73rd European Space Agency (ESA) parabolic campaign held in Paderborn, Germany, from Oct 28th to Nov 5th, 2020. Special thanks to ESA and Novespace for hosting and organizing this campaign which was a unique experience for me.

I am grateful to my colleagues and friends in the SEiL lab, Constantine Papakonstantinou, Hamed Almohammadi, Huanchen Chen, Hossein Banitabaei, Salman Buksh, Ali Mozaffari, and Gurdeep Saini. They have helped me settle down and get to know the lab equipment in the first days. All the respect and many thanks to SEiL lab members especially, Khaled Yousef, Esmail Alkhomi, Yating Hu, Ahmed Azzam, for their continuous support and help throughout my PhD. I am thankful to my colleagues and friends in the TF-lab, Ahmed Elkholy, Kapil Narwal, Yehia Ezzat, Omar Khaled, who have helped me technically and thoughtfully.

I am also thankful to all the students and friends in the mechanical engineering department at York University for their wonderful friendship and all the fun moments we had together. These people made my life and PhD studies enjoyable. Too many to mention, but I would like to thank Amin Shams, Nima Talebzadeh, Alireza Zabihihesari.

I would like to acknowledge all funding received throughout my PhD from Ontario Government for offering me the Ontario Trillium Scholarship for four consecutive years, European Space Agency (ESA) for grants awarded to Prof. Amirfazli, Mitacs for providing me with the Mitacs Globalink Research Award, Parya Foundation for supporting me with Darvish Scholarship.

Finally, I would like to acknowledge that I would have never been close to this dissertation without continuous help and selfless support from my whole family, dad, mom, sister, and little brother. They endured this long process with me, always offering support and love. In addition, I would not have been where I am now without the motivation of my dad. I am blessed to have both a father and a friend in you. He is my sample model from childhood, and I hope to be half the man he is one day. Words cannot convey how much I love him and how deeply I appreciate his supports. No matter how tall I grow, I still look up to you.

TABLE OF CONTENTS

LIST OF FIGURES

Author Contributions

- **Journal Papers:**

1. **M. Shakeri Bonab**, R. Kempers, A. Amirfazli, " Determining Transient Heat Transfer Coefficient for Dropwise Condensation in the Presence of an Air flow", Int. J. Heat Mass Trans 2021.

- **Conference Presentations:**

1. **Milad Shakeri Bonab**, Roger Kempers, Alidad Amirfazli, Dropwise Condensation Shedding by Shearing Airflow in Microgravity Using Different Surface Coatings, Surface Wettability Effects on Phase Change Phenomena Workshop, Oct 2021, University of Brighton, Brighton, UK.

- **Awards and Scholarships:**

1. **Best Presentation Award** in Graduate Seminar, May 2021, Mechanical Engineering Department, York University, Toronto, Canada.
2. **Global Research Award**, Sep 2020, Mitacs, Toronto, Canada.
3. **Best Presentation Award** in Graduate Seminar, May 2020, Mechanical Engineering Department, York University, Toronto, Canada.
4. **Darvish Scholarship**, Oct 2019, Parya Trillium Foundation, Toronto, Canada.
5. **Ontario Trillium Scholarship (OTS)** for the Ph.D. program, Oct 2017, Toronto, Canada.

Chapter 1 Introduction and Motivation

1.1 Introduction

1.1.1 Background information and research direction

Water can be found in oceans, lakes, rivers, and the air, and it is vital to life on Earth. About 90% of the human body consists of water, and in general, the sustainability of life on Earth depends on water. It makes the environment moist, and its existence in the atmosphere is essential as water vapour plays many critical roles in the life form on Earth. For instance, people's comfort level is determined by the relative humidity of the environment. In a spacecraft (enclosed environment), water represents 95% of the entire consumable necessities for human life support, considering the average quantity of water, oxygen, and food used by crew and living organisms every day [1]. Various basic phenomena and their adaptation to microgravity must be well understood to control the water cycle inside a confined environment. This cycle happens naturally in the Earth's atmosphere (e.g., condensation and evaporation of humid air). Usually, enclosed environments (spacecraft) have a relative humidity (25 to 75%), and condensation may occur on the skin, plant leaves, and any solid surface [1]. Therefore, without proper air conditioning systems, such condensates can harm electronic devices, prevent the human body's cooling (hindering the evaporation of sweat), and cause fungal and microorganisms' growth in a microgravity environment.

1.1.2 Fundamentals of condensation

Condensation of the humid air has various applications such as water harvesting systems [2], [3], dehumidification [4], distillation /desalination [5], and refrigeration and air conditioning [6].

Condensation takes place on a solid surface when the substrate temperature falls below the saturation temperature of the vapour. Condensation on the solid surface can be classified as filmwise condensation (FWC) or dropwise condensation (DWC) based on surface wettability [7]. FWC is seen when the surface wettability is high. By contrast, DWC occurs when the contact angle between liquid and surface is sufficiently large to prevent the formation of a stable liquid film [8]. Heat transfer through DWC is characterized by a significant increase in heat transfer coefficient (HTC) compared to FWC [9]. Hence, it is not surprising that there are many experimental and numerical studies in the literature on the DWC of pure vapour [10]. Some of the applications mentioned above involve the DWC of humid air (i.e., the case where non-condensable gases are present); relatively few studies have examined this aspect [11]–[14].

Starting with pure vapour condensation, it has been shown that the HTC during DWC mode is up to 5–30 times higher than those in FWC mode [15]–[17]. The liquid film in FWC mode, due to the low thermal conductivity and consequently high thermal resistance, acts as a barrier between the vapour and surface (*Figure 1.1-a*). However, in DWC, the continuous removal of the condensates allows the new vapour to be exposed to the surface to facilitate further condensation, improving heat transfer performance. The following two requirements are necessary to have DWC: (1) An external force to stimulate the condensates to move (*Figure 1.1-b*), and (2) substrate with low surface energy to facilitate droplets movement and create the thermodynamically favourable conditions for DWC (*Figure 1.1-c*); otherwise, the condensation mode switches to FWC.

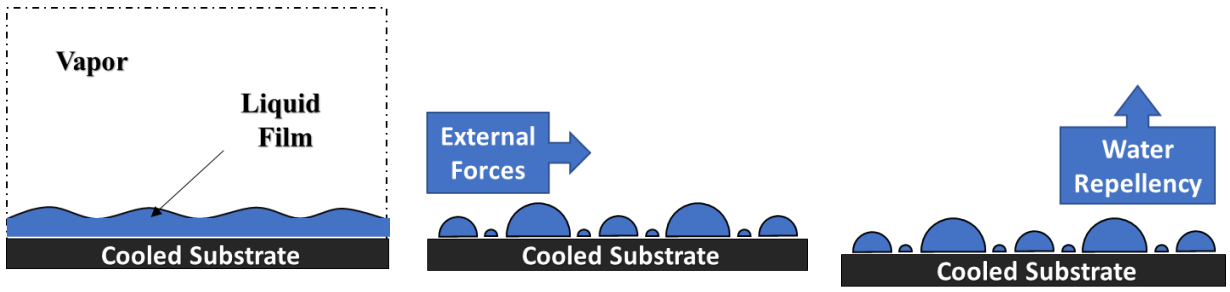

(a) (b) (c)

Figure 1.1. Schematic view of condensation on a cooled substrate. (a) Filmwise condensation. The liquid layer acts as a barrier to condensation. (b) Dropwise condensation. External forces remove the condensates (c) The condensates are removed easily using a substrate with low surface energy.

1.1.3 Dropwise condensation

Dropwise condensation (DWC) is known to be a superior mode of heat transfer compared to the alternative, i.e., filmwise condensation (FWC). DWC can improve heat transfer performance in almost all processes that involve a phase change [18]. Achieving DWC can be significant for the energy sector [19], power plants; chemical industry [18], refineries; production of water by desalination [5], and HVAC (Heating, Ventilation, and Air Conditioning) systems [6]. This latter point directly relates to the environmental control and life support system (ECLSS) in space vehicles. Also, DWC can be found in other applications related to reduced gravity environments, such as thermal management systems for satellites, power management systems, and wastewater treatment for manned space platforms. The high HTC seen in systems with DWC also means that the size of the system can be small, which entails a lighter structure. This point is essential for space application as one of the goals for system design is the minimization of a system's weight. However, the condensation phenomenon at the liquid-vapour interface in zero gravity (i.e., space applications) is not well understood. Therefore, it is necessary to understand the humid air condensation in a microgravity environment. Characterizing the condensation kinematics in zero gravity can provide insight into the mechanism for the systems reliant on condensation.

DWC is a cyclic process involving the following steps: nucleation, growth, coalescence, and droplet shedding [20]. Due to the vapour and surface having direct contact, the vapour condenses and grows at nucleation sites. This growth eventually leads to coalescence with nearby droplets. After reaching a critical size, shedding in DWC is typically achieved with the aid of gravity (in vertical/tilted surfaces) [21], use of surfaces with wettability gradient [22]–[25], or through the coalescence-induced spontaneous motion of the droplets [26]–[30]. Also, exposing to shear flow (in horizontal surfaces), condensates can be removed [31]. In the latter case, the droplet moves when its external drag force overcomes the adhesion force between the droplet and the surface. The droplet's drag force depends on airflow velocity and frontal area of the droplet, which is a function of the shape of a droplet. The wetting characteristics determine the adhesion forces (e.g., surface tension, contact angle, and contact line shape/size). Therefore, both adhesion and drag forces are based upon the wetting characteristics of a droplet on the surface [31].

1.1.4 Heat transfer measurement

Heat transfer through DWC for pure vapour has been investigated widely in the literature [17]. The HTC of a DWC highly depends on droplet size distribution. Heat is assumed to be transferred through the droplets only; the area on the substrate that is free of condensate is regarded as inactive [32], [33]. In DWC, most of the heat transfer occurs in small size droplets (< 10 μm) [32], [34], [35]. The reason is that the thermal resistance of a droplet typically increases with an increase in size [36]. Therefore, it is important to keep the average size of the droplet as low as possible to get high thermal performance in DWC.

Estimating heat flux (HF), HTC, and substrate temperature are required to design systems that rely on condensation. Due to the thermal disruption, boundary layer distortion, and optical

measurement restriction, the installation of conventional sensors measuring HF and temperature at the area/location of interest is very challenging. Therefore, due to these issues, the HF, HTC, and substrate temperature are determined using the inverse heat conduction method, which is based on Fourier's law of heat conduction [37]. Linear temperature variation within the conduction medium is assumed to estimate boundary conditions. This assumption can be applied for the experiments which reach a steady-state condition after the first seconds of operation. However, since condensation has time-varying nature due to instantaneous movements of condensate on top of the solid surface, measurement of transient HFs still remains a challenge. The reason is that Fourier's law does not hold true for transient heat transfer problems [38], and the temperature variation within the medium to estimate HF is not linear anymore. Hence a transient inverse heat conduction method is required for HF measurement of condensation, which is not previously explored in the literature. The first objective of this work is to develop a transient inverse heat conduction method to characterize humid air condensation for instantaneous heat flux measurement. This objective is discussed in detail in *Chapter 2*.

1.1.5 Shedding

Most of the works so far have focused on vertical orientation for the substrate as gravity force is used for condensate drainage. In this condition, it is hard to understand the contribution of condensate movement by airflow since both gravity and shear force of airflow affect the movement of the droplet. However, it is possible to investigate airflow and its effect on shedding on a horizontal surface since airflow can control droplets removal. Shedding of droplets from a surface is a critical part of the DWC process to improve heat transfer. The majority of DWC systems take advantage of gravity to cause the drops to move (or shed) from the surface of a condenser before they grow too large to connect and create a film [6-8]. However, for space applications, this route

is not available [42]. Surface energy gradient has been suggested as a way to remove drops [10-11]; however, there can be a significant limitation on the distance that drops may be transported on such surfaces. One can take advantage of aerodynamic forces and remove/shed droplets from a surface using a stream of air (note that in ECLSS, an air stream is usually present) [45].

In most practical applications, it is challenging to omit all non-condensable gas (NCG) and just deal with pure vapour. Also, some applications are directly related to humid air, like dehumidification [4]. It was found that a small amount of NCG (volume fraction of air rose 0.5%) results in a significant decrease of HTC in FWC by nearly 50% [46]. A possible explanation for heat and mass transfer deterioration is that NCG hampers the mass transport process. Since condensate liquid/gas interface is impermeable to the NCG, they are accumulated next to the condensate interface forming a boundary layer [47]–[49]. As a result, the partial pressure of vapour decreases, as schematically shown in *Figure 1.2*; consequently, saturation temperature decreases, which deteriorates the condensation rate. Furthermore, by increasing the flow velocity of the air/vapour mixture, NCG boundary layer thickness decreases, and turbulent mass transfer increases the condensation rate. Also, the condensates removal process from the surface is enforced.

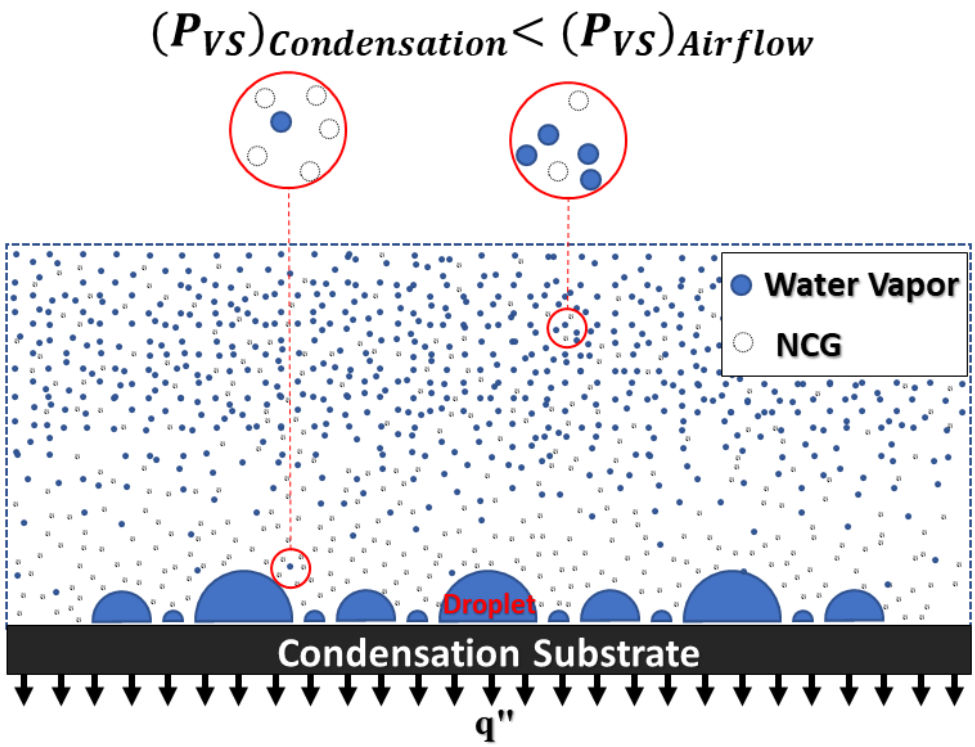

Figure 1.2. Schematic view of DWC on a cooled substrate. The partial pressure of vapour near the condensates is lower than the airflow, resulting in a lower saturation temperature near the condensates.

Although the humid air condensation may have a similar mechanism to pure steam with NCG, humid air contains only a small amount of water vapour compared to the total volume of dry air. For example, at 25 °C, one kilogram of air can hold a maximum of 22 grams of water while the remaining amount is composed of dry air, which can be considered as an NCG. The question will be raised: what is the effect of airflow on humid air condensation, which is not addressed in the literature. However, some works examined the DWC of humid air [11]–[14].

Gotze et al. [11] investigated the effect of HF, air-to-wall temperature difference (5–18 K), absolute humidity (0.006–0.063), relative humidity (RH) (10–85%), and Reynolds number (Re) (5,000–20,000) on HTC for DWC on a vertical polymer surface (polypropylene filled with 20% carbon nanotubes). In [12] a study was conducted to develop a single droplet growth model to examine the DWC for humid air on a vertical surface. This model investigated the complex

simultaneous heat and mass transfer from the free stream across the droplet to a cold surface. They used the same experimental setup as [11] for RH of 80% with sub-cooling temperatures of 0–12°C, and RH of 94% with sub-cooling temperatures of 0–8°C (the humid air temperature was 30°C). To minimize the influence of convection, the air velocity was kept less than 1 m/s. In contrast, high flow velocities (Re=14,000) were used in [11], which resulted in high HTC compared with [12]. There is an overlap in RH= 80% for the works in [11] and [12]. The HTC is approximately twice for [11] compared to [12]. Higher airflow may have some contribution to convection heat transfer, but the doubling of HTC may be related to three possible explanations caused by high airflow: induced significant turbulence levels near the surface, enforcement of droplet removal by exposure to airflow, and the removal of NCG. These were not addressed in either [11] or [12], so the results are somewhat ambiguous.

Castillo et al. [13] characterized condensation dynamics (i.e., the droplet growth and distribution) of stationary humid air for different RHs (45, 50, 55, and 70%). A vertically oriented hydrophobic surface (Teflon AF 1600, Dupont) at a constant sub-cooling temperature of 15°C was used. The relationship between condensation dynamics and RH was described based on trends of the condensation rate on the fresh substrate. The results showed that the condensation rate reduces as the droplets grow and coalesce. However, the effect of condensation dynamics (i.e., the droplet growth and distribution) on heat transfer was not investigated. Therefore, the impact of condensation dynamics on heat transfer performance is undetermined. The second objective of this work is to characterize the effect of condensation parameters (i.e., RH, subcooling temperature, and airflow velocity) on the rate of condensation. This objective is discussed in detail in *Chapter 2*.

1.1.6 Microgravity

Substrates with lower surface energy provide a higher possibility of shedding due to a lower lateral adhesion force. Therefore, a higher frequency condensation cycle augments the HTC. On the other hand, those substrates have a lower vertical adhesion force and a higher possibility of detachment, especially in a microgravity environment. Therefore, the main question to answer is whether the vertical adhesion of droplets in the presence of airflow will be strong enough in microgravity conditions to avoid detachment. In principle, it should be possible to mimic reduced gravity conditions in ground-based applications for deposited droplets; on-ground experiments have demonstrated lift-off of droplets when the droplet density and shearing medium are close [50]. However, in condensation applications, unavoidable differences in the air density and viscosity with water means that on-ground experiments cannot answer the question of re-entrainment. Also, detachment of droplets can be seen if the droplet bursts (i.e., high-speed airflow impulse) [51]. However, a burst droplet situation does not address the concern of condensate detachment because it is not a realistic situation for condensation; as such, there is a need for microgravity tests.

The use of surface coatings can increase or reduce the energy requirements for the shedding process by airflow or alter the thermodynamic conditions for DWC. The adhesion of the droplets is a function of surface properties and the condensing period. Also, the surface's wettability will significantly affect the size of condensating droplets and the adhesion of droplets onto the surface [52]. There are three possible shedding regimes for the droplet under aerodynamic forces; sliding, deformation/sliding, and deformation/sliding/detachment [50]. Sliding of condensate improves HTC by providing a fresh area for condensation. Although detachment/lifting off can provide a fresh area for the condensation cycle, most of the tiny droplets can be shed while the large droplet

is shed to slide on the surface. Also, the entrainment of droplets due to detachment is usually unwanted for the overall performance of a system.

A reduced gravity environment can be achieved using various platforms such as space missions, sounding rockets, drop towers, and parabolic flight (PF). Although space flight can provide long periods of reduced gravity, drop towers and PF are cheaper and more accessible to perform experiments. Drop tower can give 2-3 seconds of freefall. However, in PF, an aircraft flies a parabolic trajectory providing reduced gravity for up to 40 seconds [53]. The aircraft generates reduced gravity by following a trajectory that cancels the acceleration due to gravity (*Figure 1.3-a*). Essentially, microgravity is achieved, if the plane provides the acceleration of 9.81 m/s^2 in the opposite direction of gravity. The PF typically consists of 31 parabolas, each providing about 22 seconds of microgravity (*Figure 1.3-b*). Before and after microgravity, the aircraft must experience higher than normal gravity (around 1.8 g) to provide freefall.

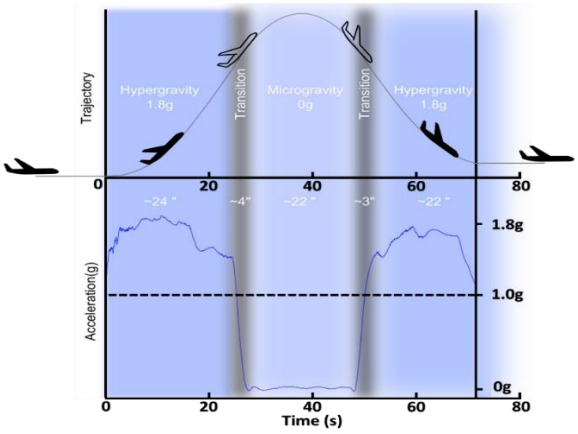

(a)

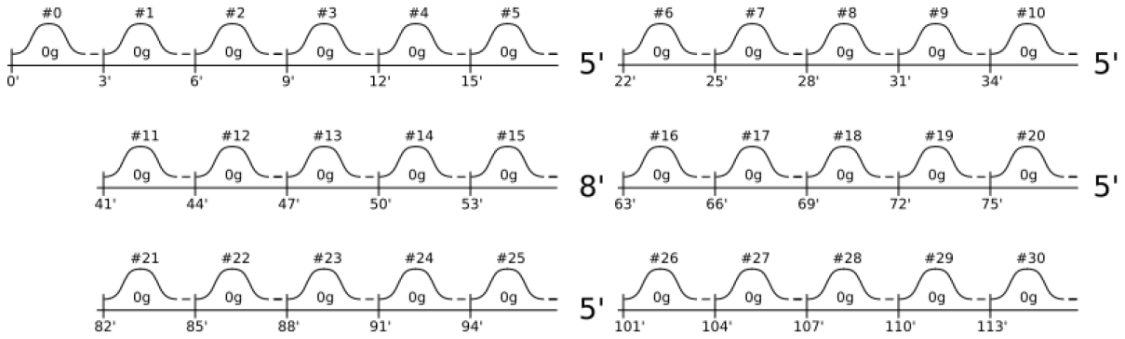

(b)

Figure 1.3. (a) The trajectory of aircraft during PF. The plane generates reduced gravity by following a trajectory that cancels the acceleration due to gravity. Each parabola consists of two hypergravity and one microgravity. (b) The PF typically consists of 31 parabolas, each providing about 22 seconds of microgravity [54].

Only a few studies exist on the influence of microgravity on the shape of droplets. Brutin et al. [55] performed fundamental experiments on sessile drop creation in microgravity. They focused on investigating the drops interaction with a solid surface (i.e., contact angle) in reduced gravity levels. Three different fluids (de-ionized water, HFE-7100 and FC-72) and two surfaces (aluminium and PTFE) was used. The results showed the contact angle behaviour depends on the drop diameter and the gravity level. They found that the contact angle can be ten degrees lower for the drop created under normal gravity than the same drop created in microgravity. Diana et al. [56] characterized droplet shape (contact angle and wetted perimeter) for drops of water and ethanol on aluminium and PTFE substrates under normal gravity and reduced gravity. The results showed that

the Young-Laplace equation could describe the shape of a tiny droplet in reduced gravity. The wetting diameter and height are related to the surface energy to obtain the lowest free energy shape (spherical cap). The wetting perimeter of the drops was found lower in reduced gravity compared to normal gravity. Lower wetting perimeter results in less adhesion force between liquid and surface. Therefore, this study did not address the fact that the reduced gravity could promote the droplet lift-off. Accordingly, the third objective of this work is to develop an understanding and evaluation of the shedding of condensate when exposed to airflow (aerodynamic forces) in a microgravity environment. The goal is to determine which coating facilitates the shedding of droplets at a low required air velocity without causing the droplets to lift off the surface. This objective is discussed in detail in *Chapter 3*.

1.1.7 Electrowetting

In practice, using a substrate with low wettability can facilitate droplets to move and keep the average size of the droplet low. An ideal condensing surface should provide sufficient sites for droplet nucleation, which is favoured on hydrophilic (water-loving) surfaces. It should also provide rapid drainage of the condensate formed to expose fresh regions for renucleation, which is favoured on hydrophobic (water-repellent) surfaces with low contact angle hysteresis to promote early shedding or coalescence of condensate droplets. The effect of structured surfaces such as super-hydrophobic, super-hydrophilic, gradient variations, hydrophilic-hydrophobic hybrid patterned surfaces on condensation heat transfer has been investigated in the literature [57]. In essence, it was found that promoting DWC is associated with better heat transfer performance due to providing a higher rate of droplet removal on the substrate. In general, compared to the mono-structure surface, using a hybrid surface enhances the condensation heat transfer by providing better condensate removal.

Hydrophobic and superhydrophobic surfaces (e.g., nanostructured, micro-grooved, wettability-patterned, and liquid impregnated textured) [58]–[63] facilitate condensate mobility and lower resistance to shedding, resulting in DWC mode [64]. However, all of the methods discussed above alter the chemical or topographical patterning of the substrate passively to promote condensate mobility. Also, previous studies have demonstrated that the coatings are not durable and long-lasting when exposed to harsh conditions such as condensation and shear stress [65], [66]. In addition, contact angle decreases by condensation time [67] which deteriorates the mobility of condensate compared to the shedding behaviour of depositing a single droplet.

Apart from passive approaches, an alternating (AC) electric field has been used to promote condensation heat transfer by actively controlling droplets dynamic [68]–[72]. Miljkovic et al. [73] developed a new electric-field-enhanced condensation mode by applying an external electric field. The results indicated that the bouncing of droplets (due to coalescence) increases the average droplet size and deteriorates the condensation heat transfer performance. Applying 100 and 200 V/cm electric fields resulted in a 50% increase in heat transfer coefficient. Kim et al. [74] used an electric field to manipulate the static three-phase contact line and surface tension on the inclined surface. They characterized three regimes (gravity dominated, intermediate, and surface force dominated) and demonstrated that the critical inclination angle decreased significantly by applying an electric field.

Previous studies have shown that the rate of condensation in the starting edge of the horizontal substrate is high, leading to a larger average droplet size [75]. The shedding initiates with those large droplets at starting edge, and the rest of the tiny droplets get removed in the way of large droplets. Therefore, one may use EW locally to manipulate the arrangement of droplets that control the shedding (i.e., at the starting edge or any location with critical droplet size for

shedding). Razzaghi et al. examined the shedding behaviour of various sessile droplets patterns when placed in close proximity to one another. The droplets pattern and spacing determined the flow structure over droplets at a specific airflow. The results indicated that when the droplets are close together (as is typically the case for condensation), the critical velocity of shedding for square arrangement is lower than a diamond arrangement. There exist some works on the utilizing of EW for condensation enhancement. However, most of them focused on pure vapour condensation. To our knowledge, all the existing works have not considered the effect of EW on the shedding of condensate by airflow. Thus, the last objective of the current work is to investigate the enhancement of heat transfer and condensate shedding during humid air condensation using EW-based surfaces on the horizontal surface. This objective is discussed in detail in *Chapter 4*.

1.2 Scientific and technological gaps

In sum, it is very important to keep the average size of the condensate as low as possible to get high thermal performance in DWC. Therefore, the shedding of condensate from a surface is a critical part of the DWC process to improve heat transfer. Airflow is used as way of shedding when the other methods are not available. However, the effect of airflow on humid air condensation and the impact of condensation dynamics on heat transfer performance are not addressed in the literature. Also, estimating heat flux (HF), HTC, and substrate temperature are required to design systems that rely on condensation. Because condensation has time-varying nature due to instantaneous movements of condensate on top of the solid surface, measurement of transient HFs still remains a challenge. Therefore, it is of fundamental importance to understand the influence of airflow during humid air condensation on the horizontal surface using a transient method. This understanding provides an insight into designing surfaces that aim to optimize the heat transfer performance.

In addition, substrates with lower surface energy provide a higher possibility of shedding due to a lower lateral adhesion force. Therefore, a higher frequency condensation cycle augments the HTC. On the other hand, those substrates have a lower vertical adhesion force and a higher possibility of detachment, especially in a microgravity environment. Although detachment/lifting off can provide a fresh area for the condensation cycle, most of the tiny droplets can be shed while the large droplet is shed to slide on the surface. Also, the entrainment of droplets due to detachment is usually unwanted for the overall performance of a system. Therefore, the main question to answer is whether the vertical adhesion of droplets in the presence of airflow will be strong enough in microgravity conditions to avoid detachment. Such knowledge allows us to properly design condensers that can work under microgravity conditions, and in dropwise condensation mode. This information is not available, and the success of this work can generate novel knowledge relevant to space technology and applications.

Moreover, using coated surfaces can facilitate condensate mobility and lower resistance to shedding, resulting in DWC mode. However, the coatings alter the chemical or topographical patterning of the substrate passively to promote condensate mobility. Also, the coatings are not durable and long-lasting when exposed to harsh conditions such as condensation and shear stress. In addition, contact angle decreases by condensation time which deteriorates the mobility of condensate compared to the shedding behaviour of depositing a single droplet. AC electric field has been used to promote condensation heat transfer by actively controlling droplets dynamic. However, most of works focused on pure vapour condensation. To our knowledge, all the existing works have not considered the effect of EW on the shedding of condensate by airflow. Therefore, it is necessary to investigate the enhancement of heat transfer and droplet shedding during humid air condensation using EW-based surfaces on the horizontal surface. This knowledge provides an

understanding into using EW locally to manipulate the arrangement of droplets that control the shedding (i.e., at the starting edge or any location with critical droplet size for shedding).

1.3 Thesis goals, objectives and outline

The main goal is to understand how the shedding of condensate affects the mechanisms that govern DWC dynamics and relate those effects to the overall HTC. Then, the shedding of condensates can be manipulated using an EW-based surface to get higher HTC as much as possible. In summary, the main research questions which are going to be answered are:

- How can the transient measurement method be applied to characterize the surface HF, temperature, and associated HTC for humid air DWC?
- What is the effect of condensation parameters (i.e., RH, and subcooling temperature) on HTC and the rate of condensation for humid air DWC and horizontal orientation?
- How can airflow affect humid air DWC by facilitating condensate shedding?
- What is the relationship between condensate morphology (i.e., the size of droplets, coverage ratio, and droplet distribution) and HTC for humid air DWC?
- How can gravity affect the shedding of condensate? What type of coating would promote shedding and, at the same time, avoid the re-entrainment of droplets?
- How can electrowetting (i.e., surface with structured electrodes) enhance the humid air DWC and heat transfer performance on horizontal surfaces?

Based on the above-explained research questions, the research objectives are:

1. To develop a transient inverse heat conduction method to characterize humid air DWC to measure instantaneous heat flux and HTC.

2. To characterize the effect of condensation parameters (i.e., RH, subcooling temperature, and airflow velocity) on the rate of DWC and heat transfer performance.
3. To develop an understanding and evaluation of the shedding of condensate when exposed to humid airflow (aerodynamic forces) in a microgravity environment.
4. To investigate the enhancement of heat transfer and condensate shedding during humid air condensation using EW-based surfaces on the horizontal surface.

The current thesis consists of 5 chapters in a "sandwich thesis" format. Each chapter contains in detailed introduction and literature review. *Chapter 1* provides a brief introduction and background information. Also, motivation, objectives and a short literature survey are covered in this chapter. *Chapter 2* tackle objective 1 and 2 and has been extracted from the technical journal paper. *Chapter 3* and *Chapter 4* address objectives 3 and 4, respectively. Lastly, *Chapter 5* summarises the thesis by conclusions with suggestions for future works. Note that the appendices is provided afterward.

1.4 References

[1] S. H. Schwartzkopf, “Design of a controlled ecological life support system: regenerative technologies are necessary for implementation in a lunar base CELSS.,” *Bioscience*, vol. 42, no. 7, pp. 526–535, 1992.

[2] R. V Wahlgren, “Atmospheric water vapour processor designs for potable water production: a review,” *Water Res.*, vol. 35, no. 1, pp. 1–22, 2001.

[3] D. Milani, A. Abbas, A. Vassallo, M. Chiesa, and D. Al Bakri, “Evaluation of using thermoelectric coolers in a dehumidification system to generate freshwater from ambient air,” *Chem. Eng. Sci. J.*, vol. 66, pp. 2491–2501, 2011.

[4] R. L. Webb and K. Hong, “Performance of Dehumidifying Heat Exchangers With and Without Wetting Coatings,” in *Transaction of the ASME*, 1999, p. vol. 125, 1018-1026.

[5] S. Parekh, M. M. Faridb, J. R. Selmana, and S. Al-Hallaj"', “Solar desalination with a humidification-dehumidification technique-a comprehensive technical review,” *Desalination*, vol. 160, pp. 167–186, 2004.

[6] M.-H. Kim and C. W. Bullard, “Air-side performance of brazed aluminum heat exchangers under dehumidifying conditions,” *Int. J. Refrig.*, vol. 25, no. 7, pp. 924–934, Nov. 2002.

[7] J. W. Rose, “Dropwise condensation. Heat Exchenger Design Handbook,” in *Begell House*, Begellhouse, 1998.

[8] I. Tanasawa, “Advances in Condensation Heat Transfer,” *Adv. Heat Transf.*, vol. 21, pp. 55–139, Jan. 1991.

[9] M. Rama, N. Reddy, M. Yohan, and K. H. Reddy, “Heat Transfer Co-Efficient Through Dropwise Condensation and Filmwise Condensation Apparatus,” *Int. J. Sci. Res. Publ.*, vol. 2, no. 12, 2012.

[10] J. W. Rose, “Dropwise condensation theory and experiment: A review,” *Proc. Inst. Mech. Eng. Part A J. Power Energy*, vol. 216, no. 2, pp. 115–128, 2002.

[11] P. Götze, C. Philipp, and U. Gross, “Dropwise Condensation Experiments with Humid Air at a Polymer Surface,” *J. Phys. Conf. Ser.*, vol. 395, no. 1, p. 012129, Nov. 2012.

[12] S. Zheng, F. Eimann, C. Philipp, T. Fieback, and U. Gross, “Modeling of heat and mass transfer for dropwise condensation of moist air and the experimental validation,” *Int. J. Heat Mass Transf.*, vol. 120, pp. 879–894, 2018.

[13] J. E. Castillo, J. A. Weibel, and S. V. Garimella, “The effect of relative humidity on dropwise condensation dynamics,” *Biol. Control*, vol. 80, pp. 759–766, 2015.

[14] S. Danilo, C. Dominique, and P. Frédéric, “Experimental dropwise condensation of unsaturated humid air – Influence of humidity level on latent and convective heat transfer for fully developed turbulent flow,” *Int. J. Heat Mass Transf.*, vol. 102, pp. 846–855, 2016.

[15] J. W. Rose, “On the mechanism of dropwise condensation,” *Int. J. Heat Mass Transf.*, vol. 10, no. 6, pp. 755–762, Jun. 1967.

[16] G. Koch, K. Kraft, and A. Leipertz, “Parameter study on the performance of dropwise condensation,” *Rev. Générale Therm.*, vol. 37, no. 7, pp. 539–548, Jul. 1998.

[17] J. W. Rose, “Dropwise condensation theory and experiment: A review,” *Proc. Inst. Mech. Eng. Part*

A J. Power Energy, vol. 216, no. 2, pp. 115–128, Jan. 2002.

[18] M. Ahlers, A. Buck-Emden, and H. J. Bart, "Is dropwise condensation feasible? A review on surface modifications for continuous dropwise condensation and a profitability analysis," *J. Adv. Res.*, vol. 16, pp. 1–13, 2019.

[19] J. M. Beér, "High efficiency electric power generation: The environmental role," *Progress in Energy and Combustion Science*, vol. 33, no. 2. Pergamon, pp. 107–134, 01-Apr-2007.

[20] P. Meakin, "Steady state behavior in a model for droplet growth, sliding and coalescence: the final stage of dropwise condensation," *Phys. A Stat. Mech. its Appl.*, vol. 183, no. 4, pp. 422–438, May 1992.

[21] C. Dietz, K. Rykaczewski, a G. Fedorov, and Y. Joshi, "Visualization of droplet departure on a superhydrophobic surface and implications to heat transfer enhancement during dropwise condensation," *Appl. Phys. Lett.*, vol. 97, no. 3, pp. 33103–33104, 2010.

[22] S. Daniel, M. K. Chaudhury, and J. C. Chen, "Fast drop movements resulting from the phase change on a gradient surface.," *Science*, vol. 291, no. 5504, pp. 633–637, Jan. 2001.

[23] P. S. Mahapatra, A. Ghosh, R. Ganguly, and C. M. Megaridis, "Key design and operating parameters for enhancing dropwise condensation through wettability patterning," *Int. J. Heat Mass Transf.*, vol. 92, pp. 877–883, Jan. 2016.

[24] A. Ghosh, S. Beaini, B. J. Zhang, R. Ganguly, and C. M. Megaridis, "Enhancing dropwise condensation through bioinspired wettability patterning," *Langmuir*, vol. 30, no. 43, pp. 13103–13115, 2014.

[25] A. M. Macner, S. Daniel, and P. H. Steen, "Condensation on Surface Energy Gradient Shifts Drop Size Distribution toward Small Drops," *Langmuir*, vol. 30, no. 7, pp. 1788–1798, Feb. 2014.

[26] J. Feng, Z. Qin, and S. Yao, "Factors Affecting the Spontaneous Motion of Condensate Drops on Superhydrophobic Copper Surfaces," *Langmuir*, vol. 28, no. 14, pp. 6067–6075, Apr. 2012.

[27] J. Feng, Y. Pang, Z. Qin, R. Ma, and S. Yao, "Why Condensate Drops Can Spontaneously Move Away on Some Superhydrophobic Surfaces but Not on Others," *ACS Appl. Mater. Interfaces*, vol. 4, no. 12, pp. 6618–6625, Dec. 2012.

[28] J. B. Boreyko and C.-H. Chen, "Self-Propelled Dropwise Condensate on Superhydrophobic Surfaces," *Phys. Rev. Lett.*, vol. 103, no. 18, Oct. 2009.

[29] R. Enright, N. Miljkovic, J. Sprittles, K. Nolan, R. Mitchell, and E. N. Wang, "How Coalescing Droplets Jump," *ACS Nano*, vol. 8, no. 10, pp. 10352–10362, Oct. 2014.

[30] T. Q. Liu, W. Sun, X. Y. Sun, and H. R. Ai, "Mechanism study of condensed drops jumping on super-hydrophobic surfaces," *Colloids Surfaces A Physicochem. Eng. Asp.*, vol. 414, pp. 366–374, Nov. 2012.

[31] A. J. B. Milne and A. Amirfazli, "Drop Shedding by Shear Flow for Hydrophilic to Superhydrophobic Surfaces †," *Langmuir*, vol. 25, no. 24, pp. 14155–14164, Dec. 2009.

[32] C. Graham and P. Griffith, "Drop size distributions and heat transfer in dropwise condensation," *Int. J. Heat Mass Transf.*, vol. 16, no. 2, pp. 337–346, Feb. 1973.

[33] J. W. Rose, "Condensation Heat Transfer Fundamentals," *Chem. Eng. Res. Des.*, vol. 76, no. 2, pp. 143–152, Feb. 1998.

[34] S. Lee, H. K. Yoon, K. J. Kim, S. Kim, M. Kennedy, and B. J. Zhang, “A dropwise condensation model using a nano-scale, pin structured surface,” *Int. J. Heat Mass Transf.*, vol. 60, pp. 664–671, May 2013.

[35] D. Attinger *et al.*, “Surface engineering for phase change heat transfer: A review,” *MRS Energy Sustain.*, vol. 1, pp. 1–40, Nov. 2014.

[36] B. Peng, X. Ma, Z. Lan, W. Xu, and R. Wen, “Analysis of condensation heat transfer enhancement with dropwise-filmwise hybrid surface: Droplet sizes effect,” *Int. J. Heat Mass Transf.*, vol. 77, pp. 785–794, 2014.

[37] I. Mohammed, A. R. A. Talib, M. T. H. Sultan, and S. Saadon, “Temperature and heat flux measurement techniques for aeroengine fire test: A review,” *IOP Conf. Ser. Mater. Sci. Eng.*, vol. 152, no. 1, 2016.

[38] D. G. Walker, “Heat flux determination from measured heating rates using thermographic phosphors,” *J. Heat Transfer*, vol. 127, no. 6, pp. 560–570, Jun. 2005.

[39] S. Oh and S. T. Revankar, “Experimental and theoretical investigation of film condensation with noncondensable gas,” *Int. J. Heat Mass Transf.*, vol. 49, no. 15–16, pp. 2523–2534, Jul. 2006.

[40] X. H. Ma, X. D. Zhou, Z. Lan, Y. M. LI, and Y. Zhang, “Condensation heat transfer enhancement in the presence of non-condensable gas using the interfacial effect of dropwise condensation,” *Int. J. Heat Mass Transf.*, vol. 51, no. 7–8, pp. 1728–1737, Apr. 2008.

[41] J. Huang, J. Zhang, and L. Wang, “Review of vapor condensation heat and mass transfer in the presence of non-condensable gas,” *Applied Thermal Engineering*, vol. 89. Elsevier Ltd, pp. 469–484, 06-Jul-2015.

[42] S. Khandekar and K. Muralidhar, *Dropwise condensation on inclined textured surfaces*. NYC, USA: Springer, 2014.

[43] S. Daniel, M. K. Chaudhury, and J. C. Chen, “Fast drop movements resulting from the phase change on a gradient surface,” *Science (80-.).*, vol. 291, no. 5504, pp. 633–636, Jan. 2001.

[44] A. M. Macner, S. Daniel, and P. H. Steen, “Condensation on surface energy gradient shifts drop size distribution toward small drops,” *Langmuir*, vol. 30, no. 7, pp. 1788–1798, Feb. 2014.

[45] A. Razzaghi, S. A. Banitabaei, and A. Amirfazli, “Shedding of multiple sessile droplets by an airflow,” *Phys. Fluids*, vol. 30, no. 8, p. 087104, Aug. 2018.

[46] D. F. Othmer, “The Condensation of Steam,” *Ind. Eng. Chem.*, vol. 21, no. 6, pp. 576–583, Jun. 1929.

[47] D. W. Tanner, D. Pope, C. J. Potter, and D. West, “Heat transfer in dropwise condensation at low steam pressures in the absence and presence of non-condensable gas,” *Int. J. Heat Mass Transf.*, vol. 11, no. 2, pp. 181–190, Feb. 1968.

[48] S. Oh and S. T. Revankar, “Experimental and theoretical investigation of film condensation with noncondensable gas,” *Int. J. Heat Mass Transf.*, vol. 49, no. 15–16, pp. 2523–2534, Jul. 2006.

[49] X.-H. Ma, X.-D. Zhou, Z. Lan, Y.-M. LI, and Y. Zhang, “Condensation heat transfer enhancement in the presence of non-condensable gas using the interfacial effect of dropwise condensation,” *Int. J. Heat Mass Transf.*, vol. 51, no. 7–8, pp. 1728–1737, Apr. 2008.

[50] S. Madani and A. Amirfazli, “Oil drop shedding from solid substrates by a shearing liquid,” *Colloids Surfaces A Physicochem. Eng. Asp.*, vol. 441, pp. 796–806, Jan. 2014.

[51] S. Moghtadernejad, M. Tembely, M. Jadidi, N. Esmail, and A. Dolatabadi, “Shear driven droplet shedding and coalescence on a superhydrophobic surface,” *Phys. Fluids*, vol. 27, no. 3, p. 032106, Mar. 2015.

[52] A. Amirfazli, V. Bertola, and C. A. Papakonstantinou, “Contact Angle Changes under a Condensating Environment,” in *IACIS*, 2018.

[53] F. Karmali and M. Shelhamer, “The dynamics of parabolic flight: Flight characteristics and passenger percepts,” *Acta Astronaut.*, vol. 63, no. 5–6, pp. 594–602, Sep. 2008.

[54] Novespace, “A310 Zero-G User Guide,” pp. 1–30, 2017.

[55] D. Brutin, Z. Zhu, O. Rahli, J. Xie, Q. Liu, and L. Tadrist, “Sessile drop in microgravity: Creation, contact angle and interface,” *Microgravity Sci. Technol.*, vol. 21, no. SUPPL. 1, pp. 67–76, Aug. 2009.

[56] A. Diana, M. Castillo, D. Brutin, and T. Steinberg, “Sessile drop wettability in normal and reduced gravity,” *Microgravity Sci. Technol.*, vol. 24, no. 3, pp. 195–202, Jun. 2012.

[57] K. S. Yang, K. H. Lin, C. W. Tu, Y. Z. He, and C. C. Wang, “Experimental investigation of moist air condensation on hydrophilic, hydrophobic, superhydrophilic, and hybrid hydrophobic-hydrophilic surfaces,” *Int. J. Heat Mass Transf.*, vol. 115, pp. 1032–1041, 2017.

[58] J. B. Boreyko and C. H. Chen, “Self-propelled dropwise condensate on superhydrophobic surfaces,” *Phys. Rev. Lett.*, vol. 103, no. 18, p. 184501, Oct. 2009.

[59] N. Miljkovic, R. Enright, and E. N. Wang, “Effect of droplet morphology on growth dynamics and heat transfer during condensation on superhydrophobic nanostructured surfaces,” *ACS Nano*, vol. 6, no. 2, pp. 1776–1785, Feb. 2012.

[60] N. Miljkovic *et al.*, “Jumping-droplet-enhanced condensation on scalable superhydrophobic nanostructured surfaces,” *Nano Lett.*, vol. 13, no. 1, pp. 179–187, Jan. 2013.

[61] N. Miljkovic, D. J. Preston, R. Enright, and E. N. Wang, “Electric-field-enhanced condensation on superhydrophobic nanostructured surfaces,” *ACS Nano*, vol. 7, no. 12, pp. 11043–11054, Dec. 2013.

[62] R. D. Narhe and D. A. Beysens, “Nucleation and growth on a superhydrophobic grooved surface,” *Phys. Rev. Lett.*, vol. 93, no. 7, p. 076103, Aug. 2004.

[63] A. Ghosh, S. Beaini, B. J. Zhang, R. Ganguly, and C. M. Megaridis, “Enhancing dropwise condensation through bioinspired wettability patterning,” *Langmuir*, vol. 30, no. 43, pp. 13103–13115, Nov. 2014.

[64] J. W. Rose, “Dropwise condensation theory and experiment: A review,” *Proc. Inst. Mech. Eng. Part A J. Power Energy*, vol. 216, no. 2, pp. 115–128, 2002.

[65] C. Lee, H. Kim, and Y. Nam, “Drop Impact Dynamics on Oil-Infused Nanostructured Surfaces,” *Langmuir*, vol. 30, no. 28, pp. 8400–8407, Jul. 2014.

[66] J. S. Wexler, I. Jacobi, and H. A. Stone, “Shear-driven failure of liquid-infused surfaces,” *Phys. Rev. Lett.*, vol. 114, no. 16, p. 168301, Apr. 2015.

[67] C. A. Papakonstantinou, H. Chen, V. Bertola, and A. Amirfazli, “Effect of condensation on surface contact angle,” *Colloids Surfaces A Physicochem. Eng. Asp.*, vol. 632, p. 127739, Jan. 2022.

[68] P. Birbarah, Z. Li, A. Pauls, and N. Miljkovic, “A Comprehensive Model of Electric-Field-Enhanced Jumping-Droplet Condensation on Superhydrophobic Surfaces,” *Langmuir*, vol. 31, no. 28, pp.

7885–7896, Jul. 2015.

[69] X. Yan, J. Li, L. Li, Z. Huang, F. Wang, and Y. Wei, “Droplet condensation on superhydrophobic surfaces with enhanced dewetting under a tangential AC electric field,” *Appl. Phys. Lett.*, vol. 109, no. 16, p. 161601, Oct. 2016.

[70] T. Foulkes, J. Oh, P. Birbarah, J. Neely, N. Miljkovic, and R. C. N. Pilawa-Podgurski, “Active hot spot cooling of GaN transistors with electric field enhanced jumping droplet condensation,” *Conf. Proc. - IEEE Appl. Power Electron. Conf. Expo. - APEC*, pp. 912–918, May 2017.

[71] A. Shahriari, P. Birbarah, J. Oh, N. Miljkovic, and V. Bahadur, “Electric Field–Based Control and Enhancement of Boiling and Condensation,” *https://doi.org/10.1080/15567265.2016.1253630*, vol. 21, no. 2, pp. 102–121, Apr. 2016.

[72] E. D. Wikramanayake and V. Bahadur, “Electrowetting-based enhancement of droplet growth dynamics and heat transfer during humid air condensation,” *Int. J. Heat Mass Transf.*, vol. 140, pp. 260–268, Sep. 2019.

[73] N. Miljkovic, D. J. Preston, R. Enright, and E. N. Wang, “Electric-field-enhanced condensation on superhydrophobic nanostructured surfaces,” *ACS Nano*, vol. 7, no. 12, pp. 11043–11054, 2013.

[74] J. Kim and M. Kaviany, “Purging of dropwise condensate by electrowetting,” *J. Appl. Phys.*, vol. 101, no. 10, 2007.

[75] M. Shakeri Bonab, R. Kempers, and A. Amirfazli, “Determining transient heat transfer coefficient for dropwise condensation in the presence of an air flow,” *Int. J. Heat Mass Transf.*, vol. 173, p. 121278, Jul. 2021.

Chapter 2 Shedding Behaviour of DWC in the Presence of an Airflow[1]

2.1 Introduction

Condensation of humid air has many applications, including water harvesting systems [1], [2], dehumidification [3], distillation/desalination [4], refrigeration, and air-conditioning [5]. Condensation takes place on a solid surface when the substrate temperature falls below the saturation temperature of the vapour. Condensation on a solid surface can be classified as filmwise condensation (FWC) or dropwise condensation (DWC) based on the surface wettability [6]. FWC occurs when the surface wettability is high, while DWC occurs when the contact angle between liquid and surface is sufficiently large to prevent the formation of a stable liquid film [7]. Heat transfer through DWC is characterized by a large heat transfer coefficient (HTC) when compared to FWC [8]. Hence, it is not surprising that there are many experimental and numerical studies on DWC of pure vapour [9]. Some of the above-mentioned applications involve DWC of humid air (i.e., the case where non-condensable gases are present); relatively few studies have examined this aspect [10]–[13].

DWC studies for pure vapour condensation have shown that the HTC during DWC mode is up to 5–30 times higher than that in FWC mode [14]–[16]. The liquid film in FWC mode acts as a thermal resistance between the vapour and surface due to the low thermal conductivity of the relatively thick liquid layer. In contrast, for DWC the continuous removal of the condensate allows new vapour to be exposed to the surface, facilitating further condensation and improving the heat

[1] *This chapter has been published as a peer-reviewed journal paper titled "Determining transient heat transfer coefficient for dropwise condensation in the presence of an air flow" in International Journal of Heat and Mass Transfer.*

transfer rate. The following two requirements are necessary to have DWC: (i) an external force to enable condensate removal, and (ii) a substrate with low surface energy to facilitate droplet movement—otherwise, the condensation mode switches to FWC.

DWC is a cyclic process involving the following steps: nucleation, growth, coalescence, and droplet shedding [17]. Due to the vapour and surface having direct contact, the vapour condenses and grows at nucleation sites. This growth eventually leads to coalescence with nearby droplets. After a droplet reaches a critical size, shedding in DWC is typically achieved with the aid of gravity (in vertical/tilted surfaces) [18], use of surfaces with wettability gradients [19]–[22], or through the coalescence-induced spontaneous motion of the droplets [23]–[27]. Also, exposure to shear flow (in horizontal surfaces) allows condensate to be removed [28]. In the latter case, the droplet starts to move when the external drag force on the droplet overcomes the adhesion force between the droplet and the surface [29], [30]. The drag force on the droplet depends on the airflow velocity and frontal area of the droplet, which is a function of the droplet's shape. The adhesion forces are determined by the wetting characteristics (i.e., surface tension, contact angle, and contact line shape/size). Therefore, both adhesion and drag forces are based upon wetting characteristics of the droplet on the surface [28]–[30].

The HTC of DWC depends on droplet size distribution. Heat is assumed to be transferred through the droplets only; the area on the substrate that is free of condensate is regarded as inactive [31], [32]. In DWC, most of the heat transfer occurs in small-sized droplets (< 10 μm) [31], [33], [32]. This is because the thermal resistance of a droplet typically increases with an increase in size [33]. Therefore, it is important to keep the average size of the droplet at shedding as low as possible to obtain high thermal performance in DWC.

Estimations of HF, HTC, and substrate temperature are required to design systems that rely on condensation. In DWC, due to the thermal disruption, boundary layer distortion, and optical measurement restriction, the installation of conventional sensors to measure HF and temperature at the area/location of interest is not practical. To overcome this, HF, HTC, and substrate temperature are determined using the inverse heat conduction method, which is based on Fourier's law of heat conduction [36]. A linear temperature variation within the conduction medium is assumed to estimate those parameters. This assumption can be applied to experiments that reach a steady-state condition after the first seconds of operation. However, because condensation has a time-varying nature due to the instantaneous movements of condensate on the solid surface, measurement of transient HF is required. Conventional steady-state applications of Fourier's law do not provide accurate quantification of heat flux (HF) for transient heat transfer situations [37]. This is so as the temperature variation within the medium needed to estimate HF is not linear. Hence, a transient inverse heat conduction method is required for HF measurement during condensation; this has not been previously addressed.

In practice, using a substrate with low wettability can facilitate droplet movement and keep the average size of droplets low [28]–[31]. An ideal condensing surface should provide sufficient sites for droplet nucleation, which is favored on hydrophilic surfaces. It should also provide rapid drainage of the condensate formed, exposing fresh regions for re-nucleation, which is favored on hydrophobic surfaces with low contact angle hysteresis [34]. The effect of structured surfaces (such as super-hydrophobic, super-hydrophilic, wettability gradient, and hydrophilic–hydrophobic hybrid patterned surfaces) on condensation heat transfer for humid air has been investigated in the literature [38]. Yamauchi et al. [39] investigated the heat flux (HF) for a hybrid surface and they found higher HF than for hydrophobic or hydrophilic surfaces. Ghosh et al. [40] designed

wettability-patterned surfaces to control spatial nucleation, departing droplet size, and rate of condensate drainage for pure vapour. Their surface pattern improved condensate collection up to 19% compared with non-patterned surface.

DWC heat transfer for pure vapour has been investigated widely in the literature, e.g. [16]. However, in most practical applications it is very difficult to omit all non-condensable gas (NCG) and just deal with pure vapour. Also, many applications are directly related to humid air, such as dehumidification [3]. It was found that a small amount of NCG (volume fraction of air increase of 0.5%) results in a nearly 50% decrease of HTC in FWC [41]. A possible explanation for the deterioration of heat and mass transfer is that NCG hampers the mass transport process. Because the NCGs cannot permeate the condensate liquid/gas interface, they accumulate next to the condensate interface forming a boundary layer [42]–[44]. As a result, the partial pressure of vapour decreases; consequently, saturation temperature decreases, which deteriorates the condensation rate. By increasing the flow velocity of the air/vapour mixture, the NCG boundary layer thickness decreases and turbulent mass transfer increases the condensation rate. Also, the condensate removal process from the surface is ensured.

Although humid air condensation may have a similar mechanism to that of pure steam with NCG, humid air contains only a small amount of water vapour compared with the total volume of dry air. For example, at 25 °C, 1 kg of air can hold a maximum of 22 g of water while the remaining amount is composed of dry air which can be considered an NCG. This raises questions regarding the effect of airflow on humid air condensation with little attention thus far in the literature.

Gotze et al. [10] investigated the effect of HF, air-to-wall temperature difference (5–18 K), absolute humidity (0.006–0.063), relative humidity (RH) (10–85%), and Reynolds number (Re)

(5,000–20,000) on HTC for DWC on a vertical polymer surface (polypropylene filled with 20% carbon nanotubes). The onset of condensation was identified by a significant increase in HTC. However, because a steady-state inverse heat conduction method was assumed to estimate HF based on Fourier's law, the results are the average values for HTC and there is a time delay between thermal measurement and condensation identification. Therefore, transient inverse conduction should be used to obtain accurate results.

In [11] a numerical study was conducted to develop a single droplet growth model to examine the DWC for humid air on a vertical surface. This model investigated the complex simultaneous heat and mass transfer from the free stream across the droplet to a cold surface. Although the main goal of the study was numerical modelling, experiments were used for the validation of numerical results. Also, some of the inputs for the simulation, such as best-possible nucleation density, were defined using experiments. They used the same experimental setup as [10] for RH of 80% with sub-cooling temperatures of 0–12°C, and RH of 94% with sub-cooling temperatures of 0–8°C (the humid air temperature was 30°C). To minimize the influence of convection, the air velocity was kept less than 1 m/s. In contrast, high flow velocities (Re=14,000) were used in [10] which resulted in high HTC compared with [11]. There is an overlap in RH= 80% for the works in [10] and [11]. The HTC is approximately twice for [10] compared to[11]. Higher airflow may have some contribution to convection heat transfer, but the doubling of HTC may be related to three possible explanations caused by high airflow: induced significant turbulence levels near the surface, enforcement of droplet removal by exposure to airflow, and the removal of NCG. These were not addressed in either [10] or [11], so the results are somewhat ambiguous.

The effect of RH on DWC dynamics was investigated by Castillo et al. [12]. They characterized condensation dynamics (i.e., the droplet growth and distribution) of stationary humid air for different RHs (45, 50, 55, and 70%). A vertically oriented hydrophobic surface (Teflon AF 1600, Dupont) at a constant sub-cooling temperature of 15°C was used. The relationship between condensation dynamics and RH was described based on trends of the condensation rate on the fresh substrate. The results showed that the condensation rate reduces as the droplets grow and coalesce. This trend continues until coalescence occurs and clears parts of the surface for more nucleation. However, the effect of condensation dynamics (i.e., the droplet growth and distribution) on heat transfer was not investigated. Therefore, the impact of condensation dynamics on heat transfer performance is undetermined.

Shedding of droplets from a surface is a critical part of the DWC process to improve heat transfer. The use of gravity as a droplet removal technique is not always available, for example, in a microgravity environment, the use of airflow for the shedding of droplets may be considered for environmental control and life support system of space crafts [36]. Most of the works so far have focused on vertical orientation for the substrate as the force of gravity is used for condensate drainage. In this condition, it is hard to understand the contribution of condensate movement by airflow, because both gravity and shear force of airflow affect the movement of the droplet. However, on a horizontal surface, it is possible to investigate airflow and its effect on the shedding of droplets and, consequently, heat transfer.

Recently, Danilo et al. [13] experimentally studied DWC on a horizontal flat surface (steel) for turbulent humid air with a wide range of RHs (1.3–93.6%). In [13] condensation increased with humidity levels; the rate of increase was linear with time for droplets smaller than a critical size. Also, by increasing humidity levels, heat transfer increased up to 3.7 times compared with dry air

convective heat transfer. However, a specific aspect of this investigation requires attention: although instantaneous measurement was performed for the latent heat contribution of condensation by weighting the condensate (response time ranged between 3–5 s), steady-state Fourier's law was used to determine the global HF (response time is more than 200 s). As mentioned before, because condensation has a time-varying nature, the steady-state Fourier's law of heat conduction cannot be applied for instantaneous HF measurement.

Taken all together, only a few studies have investigated the effect of airflow on humid air condensation for horizontal surfaces. Also, all the existing works did not consider the effect of condensate morphology on heat transfer, which requires transient heat transfer analysis. The objective of the current study is to investigate the influence of airflow during humid air condensation on horizontal surfaces. To enable this, we also needed to develop a transient inverse heat conduction method to characterize the surface HF and associated HTC.

2.2 Experimental apparatus and procedure

Simultaneous measurement of condensation heat transfer and two-phase flow visualization was accomplished using a closed-circuit humid air wind tunnel. Condensation took place on a cooled horizontal surface in the test section. The experimental setup was designed to independently control the condensing surface temperature, RH, and air velocity. The heat transfer measurements and flow visualization were synchronized to relate the condensation dynamics (drop-size distribution) to HTC.

2.2.1 Condensation surface and heat flux meter bar

A heat flux meter bar was designed to measure the HF by using temperature sensors. The CAD model of the condensation surface and heat flux measurement system is shown in *Figure 2.1-a*.

The meter bar was made of aluminum (Al alloy 6061-T6, Metal Supermarket) instead of copper as our calculations showed a small uncertainty in temperature for the range in this study will be achieved. Mirror polished aluminum (Al alloy 6061-T6, Mc) was used as a condensation surface (Al alloy 6061-T6 – McMASTER-CARR). The surface roughness, advancing contact angle, and receding contact angle were measured as Ra = 38.30 ± 5.08 nm, $\theta_a = 71.08 \pm 2.13$, and $\theta_r = 38.22 \pm 1.74$, respectively. The meter bar on one end was attached to the aluminum condensation surface using a TIM. The other end of the meter bar was in contact with a thermoelectric cooler (CP-031, TE technology) by means of a TIM.

Resistance temperature detectors (RTDs) with a diameter of 1 mm (PT100KN1510 ± 0.01°C, Omega) were embedded inside the meter bar. The RTDs were also embedded inside the condensation surface to measure the substrate temperature, as shown in *Figure 2.1-b*. RTDs were fixed inside the holes with a depth of 16 mm using thermal interface material (TIM) to ensure maximum contact with the meter bar. The meter bar was not only thermally insulated by using extruded polystyrene (RSI-0.88, Owens Corning) to assure one-dimensional conduction, but also designed in three separate segments (see *Figure 2.1-b*) with an air gap between them to make sure the HF is one-dimensional. Using these segments, HF can be measured locally (i.e., upstream, middle section, and downstream) on the condensation surface as well. The meter bar and RTD arrangement are shown in detail in *Figure 2.1-b*.

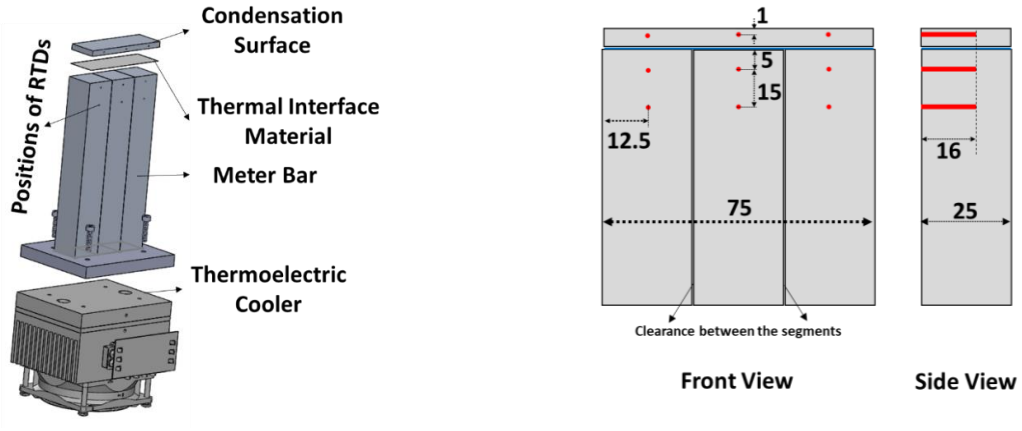

(a) (b)

Figure 2.1. a) The CAD model of the condensation surface and heat flux measurement system. b) The RTD arrangement in the meter bar (units: mm). RTDs were fixed inside the holes with a depth of 16 mm using thermal interface material to ensure maximum contact with the meter bar.

All RTDs used in the experiments were simultaneously calibrated in a constant-temperature thermal bath against a standard resistance temperature detector (50-mm-long Fluke PRT full immersion reference probe, Model 5606) calibrated by the Alpha Controls and Instrumentation (accredited to ISO/IEC 17025 by the A2LA). An isothermal-controlled copper chamber was used to perform the calibration from 5 to 25°C using the approach described in [43]. Maximum uncertainty in temperature difference between the sensors was ± 0.016 K.

2.2.2 Wind tunnel

The wind tunnel was designed to control RH and airflow velocity and to simulate the condensation environment. A schematic diagram of the wind tunnel is shown in *Figure 2.2*. Airflow velocity is controlled by a voltage regulator used to change the fan speed and it is measured by a hot-film anemometer (EE75, E+E Elektronik Ges.m.b.H) with an accuracy of ±0.2 m/s. The RH is continuously measured and controlled with a programmable humidity controller (HD100,

Auber). The control system is capable of maintaining RH in a range between 10% to 80% with an accuracy of ±4%.

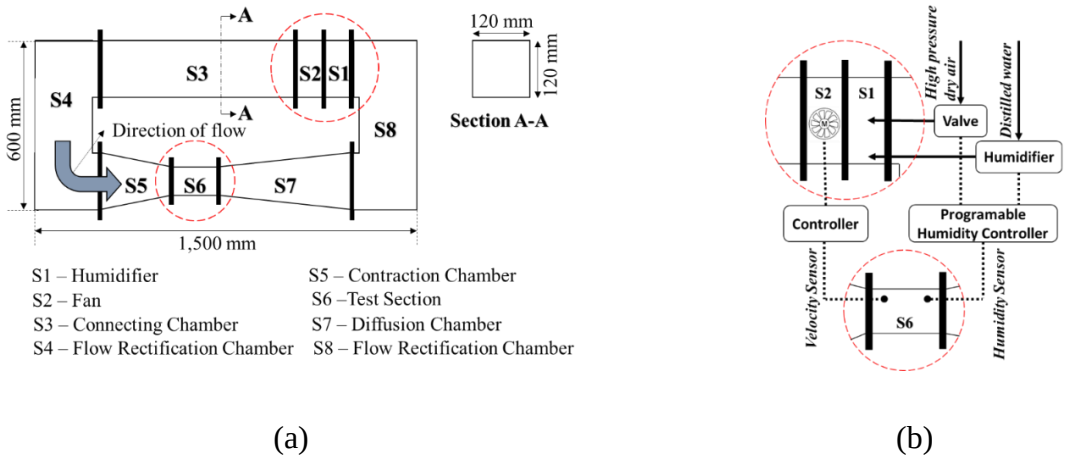

(a) (b)

Figure 2.2. Schematic diagram of the wind tunnel. (a) Dimensions and list of all components (b) Control system diagram for various functions.

2.2.3 Test section

The test section is 150 mm long with a cross-section of 50×50 mm. The bottom surface has an opening of 25×75 mm to allow for the flush placement of the condensation surface. To ensure that the non-uniformities of the flow vanish after the flow straightener, a developing length of 20% of the test section hydraulic diameter was implemented according to [46] to locate the opening. *Figure 2.3* shows the schematic view of the test section. Also, a flow characterization was carried out to evaluate flow quality (see *Appendix A: Flow quality evaluation*)

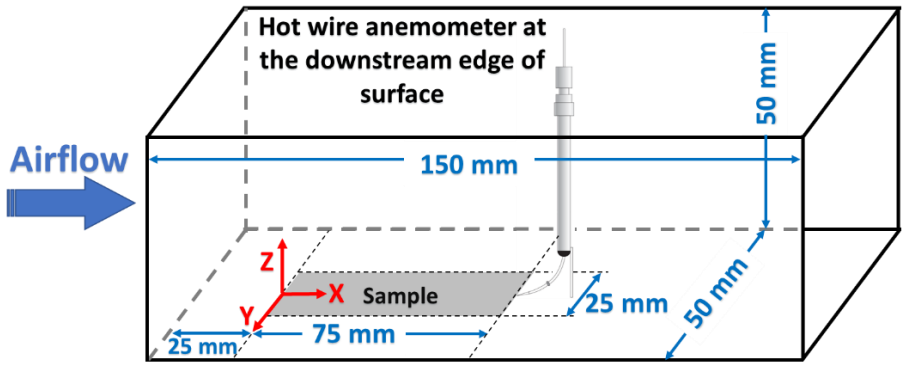

Figure 2.3. Schematic diagram of the test section.

2.2.4 Data acquisition and flow visualization

Image acquisition of droplets was done using a camera (Prosilica GX 1660, 1600 × 1200 pixel Allied Vision) which was vertically mounted; the field of view was 75 mm (lens: 50 mm/F2.8 NMV-50M23, Navitar). The images were captured with an average image size of 84 × 63 mm and an average resolution of 19 $\frac{\text{pixels}}{\text{mm}}$ or 52 µm/pixel.

For data acquisition (DAQ) and condensate morphology analysis, it was necessary to synchronize the HF measurement with the image acquisition. This way, condensation morphology can be linked to HTC. Experimental data were collected by the DAQ (34970A, Keysight) every 5 s (sampling rate), and all of the data, including temperature readings, surface T_{sc}, RH, HF, and HTC, were monitored using MATLAB.

2.2.5 Inverse heat conduction method

In the transient inverse heat conduction method, the main idea is to estimate the boundary conditions that best match the measured temperatures. Thus, one could find the transient temperature and heat flux at the top of condensating surface ($x = 0$) using the temperature data at x_1 and x_2. In *Figure 2.4* Each segment of the meter bar represents a one-dimensional body with

constant thermal properties. Continuous and smoothly varying temperature distribution inside the segment is assumed for the initial condition. The top surface and the temperature of sensors ($x = 0, x_1$ and x_2) are the adjustable boundary conditions.

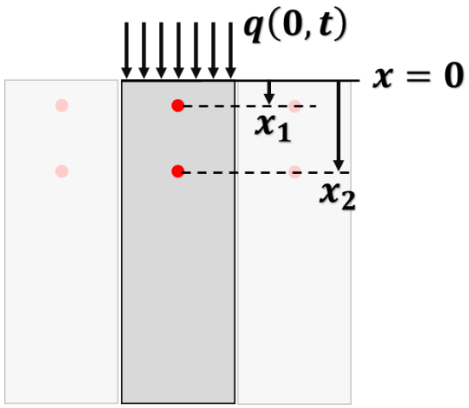

Figure 2.4. A segment of the meter bar considered as a continuous one-dimensional body

The polynomial to fit the temperature profile in a segment of the meter bar is given below [47]:

$$T_n(x,t) = \sum_{i=1}^{n} c_i(t) x^{i-1} \tag{2.1}$$

This polynomial must pass through the temperatures at the two points of x_1 and x_2. Also, it satisfies the one-dimensional heat flow equation given as:

$$\frac{\partial^2 T}{\partial x^2} = \frac{1}{\alpha}\frac{\partial T}{\partial x} \tag{2.2}$$

The coefficient $c_i(t)$ in *Eq. (2.1)* can be found using two measured values at x_1 and x_2, as well as even-numbered spatial derivatives of temperature. The following set of equations are provided to calculate $c_i(t)$:

$$\begin{bmatrix} T(x_1,\,t) \\ T(x_2,\,t) \\ \frac{\partial^2 T(x_1,\,t)}{\partial x^2} \\ \frac{\partial^2 T(x_2,\,t)}{\partial x^2} \end{bmatrix} = \begin{bmatrix} 1 & x_1 & {x_1}^2 & {x_1}^3 \\ 1 & x_2 & {x_2}^2 & {x_2}^3 \\ 0 & 0 & 2 & 6x_1 \\ 0 & 0 & 2 & 6x_2 \end{bmatrix} \begin{bmatrix} c_1(t) \\ c_2(t) \\ c_3(t) \\ c_4(t) \end{bmatrix} \tag{2.3}$$

To calculate $c_i(t)$, the inverse form of *Eq. (2.3)* can be expressed as follows:

$$\begin{bmatrix} c_1(t) \\ c_2(t) \\ c_3(t) \\ c_4(t) \end{bmatrix} = \begin{bmatrix} \frac{x_2}{x_2-x_1} & \frac{-x_1}{x_2-x_1} & \frac{x_1x_2(2x_2-x_1)}{6(x_2-x_1)} & \frac{x_1x_2(x_2-2x_1)}{6(x_2-x_1)} \\ \frac{-1}{x_2-x_1} & \frac{1}{x_2-x_1} & \frac{{x_1}^2-2x_1x_2-2{x_2}^2}{6(x_2-x_1)} & \frac{2{x_1}^2+2x_1x_2-{x_2}^2}{6(x_2-x_1)} \\ 0 & 0 & \frac{x_2}{2(x_2-x_1)} & \frac{-x_1}{2(x_2-x_1)} \\ 0 & 0 & \frac{1}{6(x_2-x_1)} & \frac{1}{6(x_2-x_1)} \end{bmatrix} \begin{bmatrix} T(x_1,\,t) \\ T(x_2,\,t) \\ \frac{\partial^2 T(x_1,\,t)}{\partial x^2} \\ \frac{\partial^2 T(x_2,\,t)}{\partial x^2} \end{bmatrix} \tag{2.4}$$

or

$$c_i(t) = a_{ij} b_i(t) \tag{2.5}$$

In *Eq. (2.5)* a_{ij} can be calculated only by knowing the sensor positions. The matrix $b_i(t)$ consists of temperature readings that are known from experiments and the second derivative terms which are obtained from the heat equation (*Eq. (2.2)*). The first temporal derivative can be used instead of dealing with the second spatial derivative [45]. To calculate the time derivative, a forward-in-time scheme was used. By having the vector $c_i(t)$, the temperature profile in the meter bar can be reconstructed. Then, boundary conditions at the required position (x = 0) can be estimated as follows:

$$T(0,\,t) \approx T_3(0,\,t) = c_1(t) \tag{2.6}$$

$$q(0,\,t) \approx -k\frac{\partial T_3(0,\,t)}{\partial x} = -kc_2(t) \tag{2.7}$$

where k is the thermal conductivity of the meter bar. It is worth noting that no specific limitation has been used for the boundary conditions, which means that the method can be applied for any boundary conditions.

The HF (q) is determined using *Eq. (2.7)*. The surface temperature (T_s) was calculated by the temperature readings in the condensation surface and by extrapolating the temperature gradient through the meter bar (HF and material are the same for the meter bar and the condensation surface) to the condensation surface. Having obtained the HF and T_s, the global HTC can be calculated from:

$$h_{global} = \frac{q}{(T_\infty - T_s)} \tag{2.8}$$

where T_∞ is the airflow temperature.

2.2.6 Uncertainty analysis

The fitted polynomial is not unique for each measurement because of uncertainties in measurements (i.e., temperature readings and position of sensors). A Monte Carlo approach described in [45] was used to find uncertainty. The maximum uncertainties of the temperature readings ($\pm$0.01°C) and positions ($\pm$0.01mm) were considered and 2000 points in the range of uncertainty were chosen randomly. Then, for each measurement, the uncertainty of HF was calculated using the propagation procedure described in [48]. A similar method was applied to the uncertainty of HTC. Further information about the Monte Carlo approach can be found in [45].

Another source of uncertainty could be the time delay between the channels of DAQ. We used 10 RTDs (10 channels) for temperature measurement. It takes 1 s to scan 60 channels based on the

datasheet of the DAQ. The scanning of each channel takes 16.7 ms. The delay was considered in time steps and the propagated uncertainties were less than the reported uncertainty.

2.3 Results and discussion

2.3.1 Response time of the meter bar

Response time refers to the time response for the output (dependent variable) when the input (independent variable) is changed. The time constant (τ) characterizes the system's dominant inertia against the changes. For the first-order system, τ is defined as the time that it takes for the output to reach 63% of its total change. The thermal inertia of the meter bar depends on the thermal diffusivity of the material (α) and characteristic length (L), and time scale of thermal conduction can be calculated using $\tau = \frac{L^2}{\alpha}$. The time scale of thermal conduction for the current meter bar was calculated as 6.25 s. This shows the inherent thermal inertia of metal used as a meter bar. However, for HTC measurement, the whole system together (including surface, TIM, and meter bar) should be considered and the measurement method plays a significant role.

Initial experiments were conducted to characterize the response time of the system to evaluate the efficiency of the transient inverse heat transfer technique. The response time of the measured heat transfer coefficient was evaluated, and the results of the inverse transient method were compared to the steady-state Fourier method. Tests were performed under single-phase convection at a subcooling temperature (T_{sc}) of 0 °C (i.e., set point of Peltier cell) and airflow velocities of 5 and 10 m/s. To understand how both methods (transient and steady-state) were responding to the changes in the boundary condition, firstly the airflow velocity was set at 5 m/s. After reaching a steady-state condition, a step change in velocity (to test how the system would respond) was applied

in less than sampling rate (i.e., an interval time of data acquisition, 5 s). The HTC for the transient method and the conventional method are compared in *Figure 2.5*.

As seen in *Figure 2.5-a*, it took the system 25 s using the steady-state method (used in the literature [11]) to respond to the step change in velocity to reach 63% of the total change in the heat transfer coefficient. Only after t=190 s (190 s after the step change) could the system predict the change in HTC to within 95%. The accuracy of the measured HF was affected due to the time-varying heat fluxes (due to the dynamic nature of DWC). By applying the transient inverse heat conduction method, it took approximately 5 s for the system to respond, i.e. a 5-fold decrease in time seen for steady-state method. Also, it took approximately 30 s (~6-fold decrease) for the system to detect the change in HTC within 95%. Thus, using the transient inverse conduction method, time-varying HTC can be measured reasonably accurately to within 30 s. After characterizing the response time, experiments were conducted to validate the applied transient method compared with a well-recommended correlation for turbulent heat transfer (see *Appendix B: Single-phase convection*).

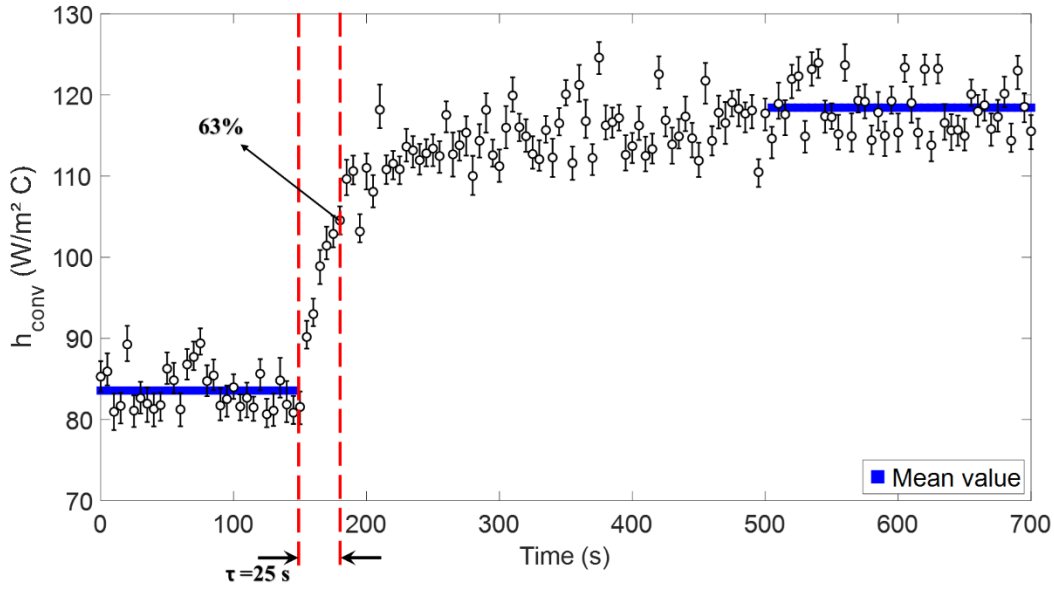

(a)

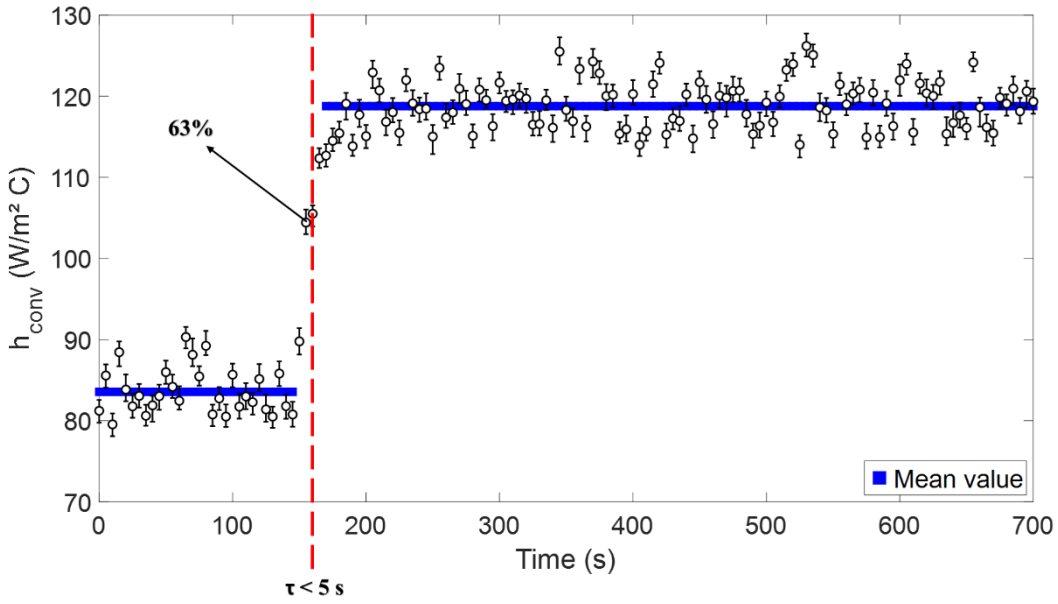

(b)

Figure 2.5. HTC versus time for the step change in velocity from 5 to 10 m/s for T_{sc} of 0°C. (a) The steady-state Fourier method was used, and the time constant is 25 s. (b) The transient inverse heat conduction method where the time constant is less than 5 s.

Although using the transient inverse heat conduction method improves the accuracy of HF measurements significantly, the number and size of sensors which were installed affect the measured data. Using small sensors, the accuracy can be further improved [11]. Also, the temporal

resolution is limited by the data acquisition sampling rate (0.2 Hz). The method used to calculate the time derivative in *Eq. (2.2)* is critical to the success of the technique because the differentiation of experimental data can be a highly unstable process [49].

2.3.2 Effect of relative humidity on condensation

In single-phase convection (i.e., no condensation), the HTC is based on the forced convection of airflow only. During condensation, in addition to the convection effect, phase change (latent heat) becomes important. Also, due to the presence of condensate (creating turbulence in the boundary layer), airflow improves the mixing of the inert gas layer and favors temperature gradients within the boundary layer [13]. The effect of single-phase convection should be removed to focus on condensation and any associated effect due to the presence of condensate. Therefore, firstly the single-phase convection heat transfer was measured using the meter bar and transient inverse heat conduction method (h_{conv}). Then, the global heat transfer coefficient (i.e., the summation of all above-mentioned effects) was measured by the same approach (h_{global}). If the effect of single-phase convection is subtracted from the global heat transfer, the result is the contribution from condensation (i.e., latent heat and all other effects due to the presence of condensate). *Eq. (2.9)* is a reasonable approximation to remove the convection effect.

$$h_{cond} = h_{global} - h_{conv} \tag{2.9}$$

The experiments were carried out for different RHs of 40, 60 and 80% at airflow velocity of 5 m/s and T_{sc} of 0°C. The results showed that HTC is highly dependent on RH which impacts parameters such as droplet growth, coalescence, and distribution. As shown in *Figure 2.6*, the maximum HTC is for the RH of 80%, especially for early stages of condensation (i.e., DWC).

However, after a while, HTC for the RH of 80% becomes close to the RH of 60%. This is because after time step, 1500 s, for the case of RH = 80 %, condensate covers the surface (FWC). Also, for higher RHs, when coverage ratio increases (finally reaches FWC), HTC decreases significantly compared with lower RHs. An RH of 80% was chosen in order for the RH to have a higher rate of condensation and save time in experiments. Moreover, RH of more than 80% was not used to avoid condensation on the walls of the observation section.

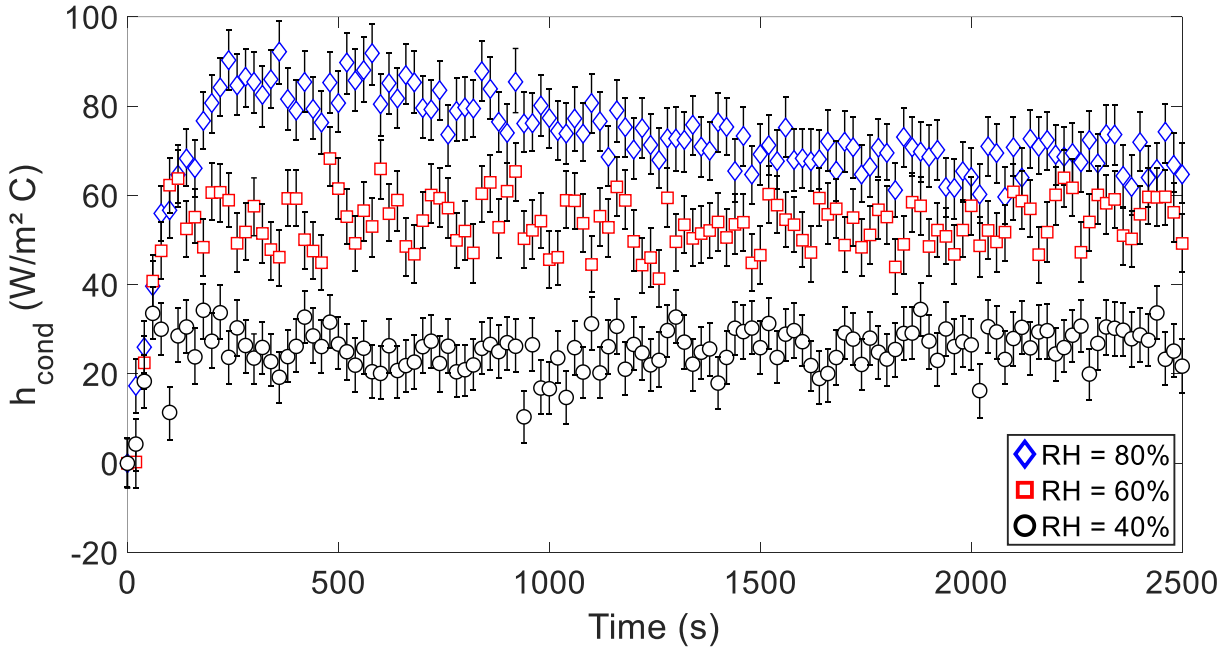

Figure 2.6. Condensation HTC versus the time for different RHs at V = 5 m/s and T_{sc} = 0 °C.

The reason for the high-frequency variations in the data points is the variation of the humid air temperature; the source of variation is the periodic addition of water to control humidity inside the wind tunnel. When adding water to the air without any heat supply, the state of the air follows a constant enthalpy line in the psychrometric chart; this results in decreasing dry air temperature. Also, the reason for the small increase in the trend of ambient temperature is the heat dissipated from the fan during the experiment. Comparing the oscillations for the raw air temperature data

and HTC using power spectral density revealed that both have the same frequency (further information in *Appendix C: Fluctuations in the results*).

2.3.3 Effect of airflow on condensation

Condensation experiments were performed at T_{sc} of 0°C and RH of 80% for the air velocities of 1, 5, 10, and 15 m/s. The experiments started from single-phase convection (RH=10%); then, the RH was increased to 80%. The system takes less than 100 s to reach the set RH. HTC for condensation versus time is displayed in *Figure 2.7* for the airflow velocities of 1, 5, and 10 m/s (shedding was not seen in this range). Higher HTC was found (as seen in *Figure 2.7*) for the velocity of 10 m/s, likely due to significant turbulence levels near the surface.

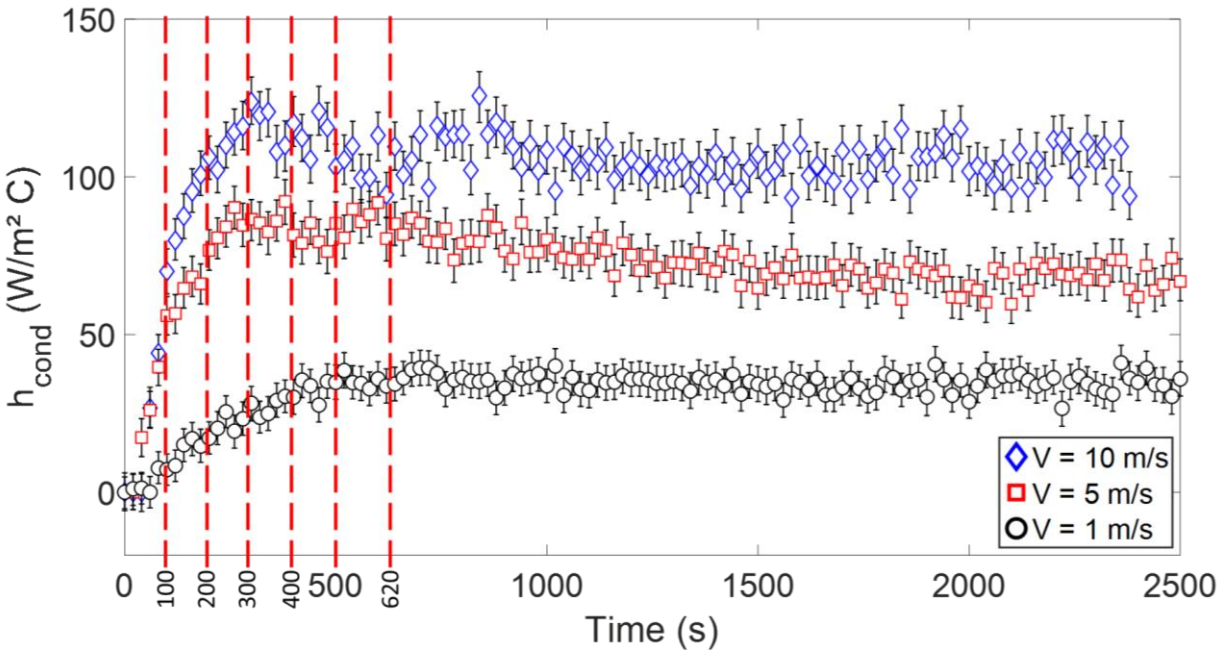

Figure 2.7. Condensation HTC versus time. These values are HTC for condensation contribution only. The RH and T_{sc} were 80% and 0°C, respectively.

To have a better understanding of the airflow effect, condensate morphology on the surface was investigated. In time steps of 100, 200, 300, 500, and 620 s, the corresponding images are provided for velocities of 1, 5, and 10 m/s in *Figure 2.8* to *Figure 2.10*.

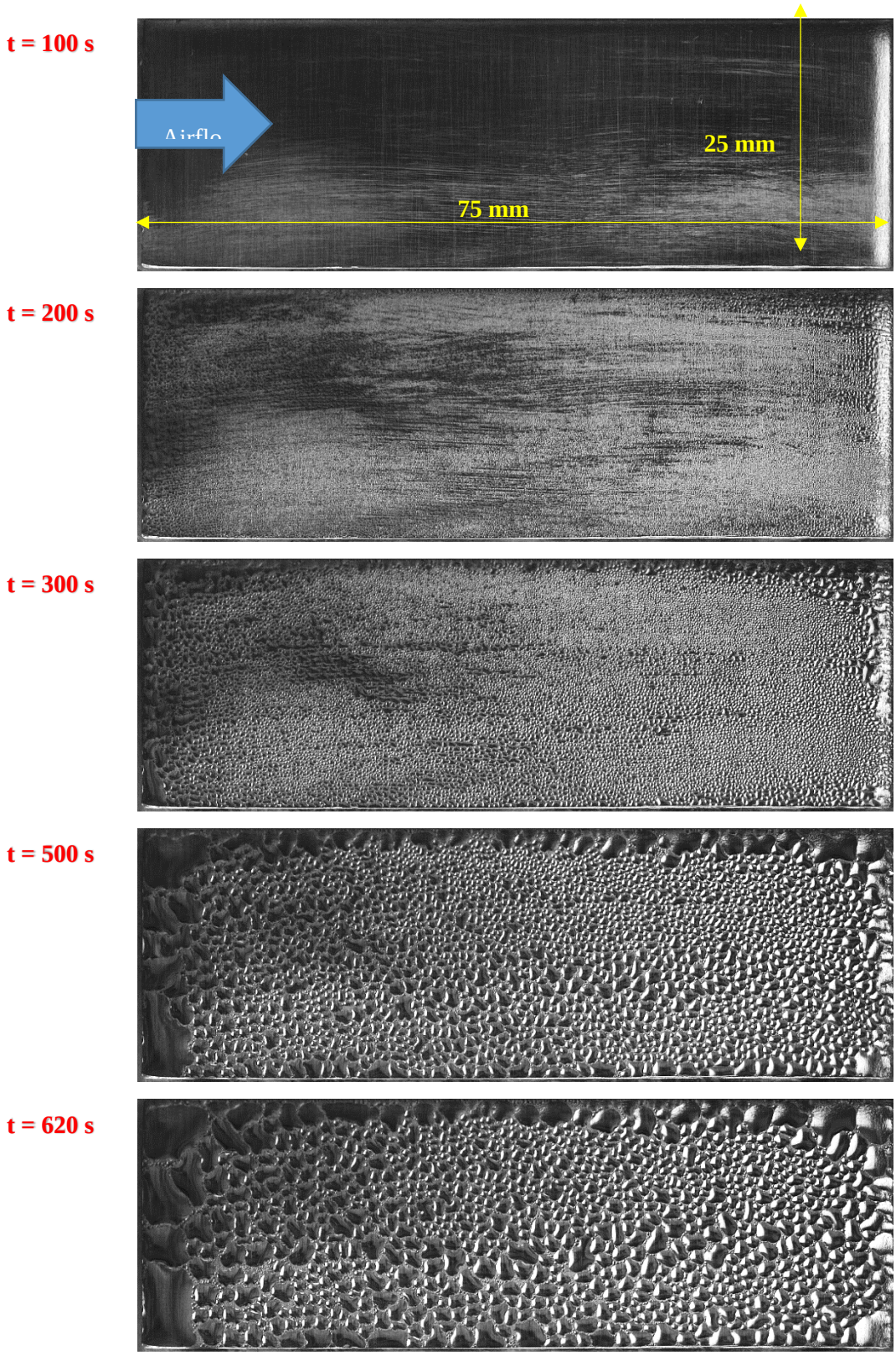

Figure 2.8. Condensate morphology on top of the surface in different time steps for airflow velocity of 1 m/s at RH = 80% and T_{sc} = 0°C.

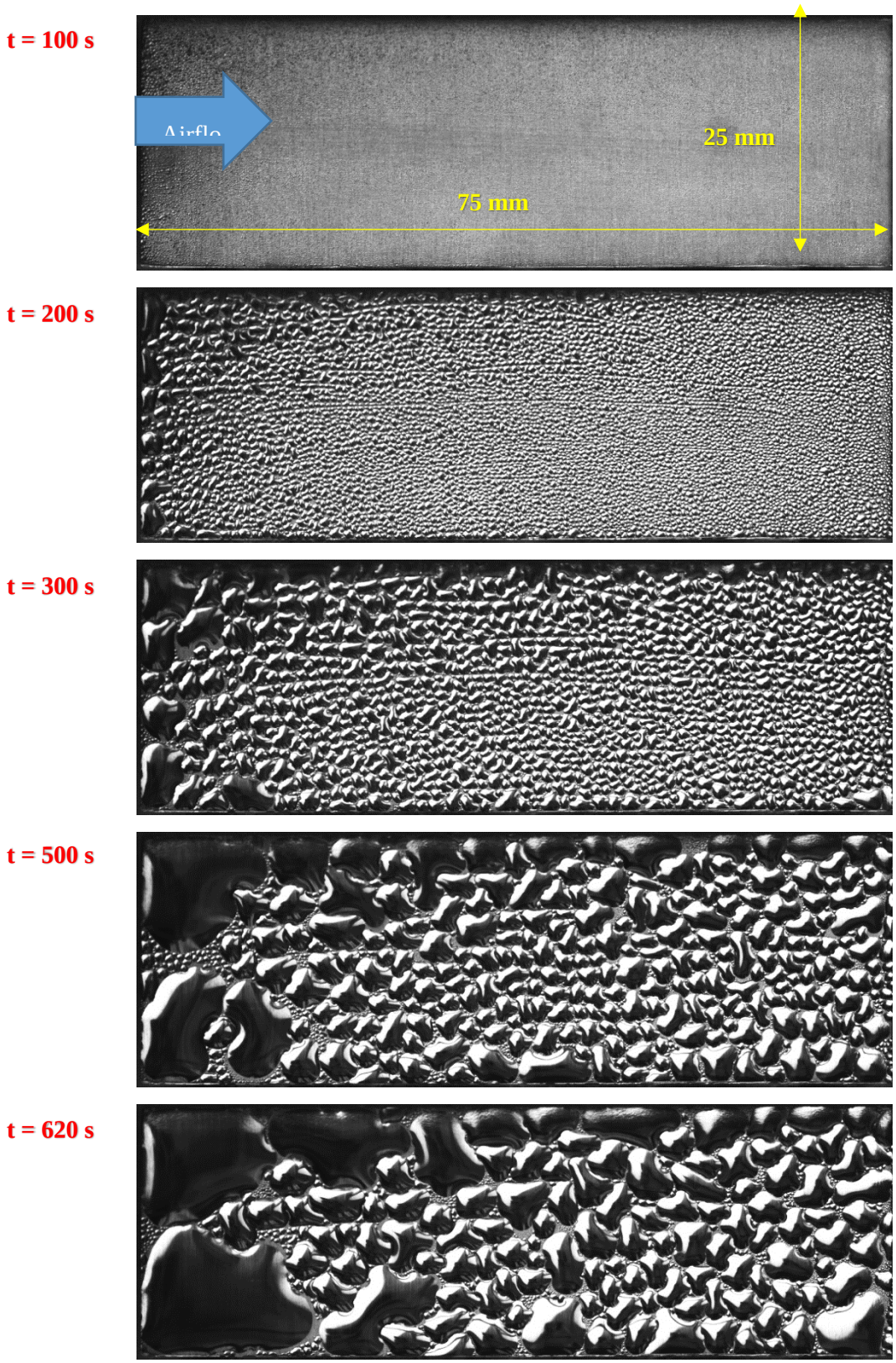

Figure 2.9. Condensate morphology on top of the surface in different time steps for airflow velocity of 5 m/s at RH = 80% and T_{sc} = 0°C.

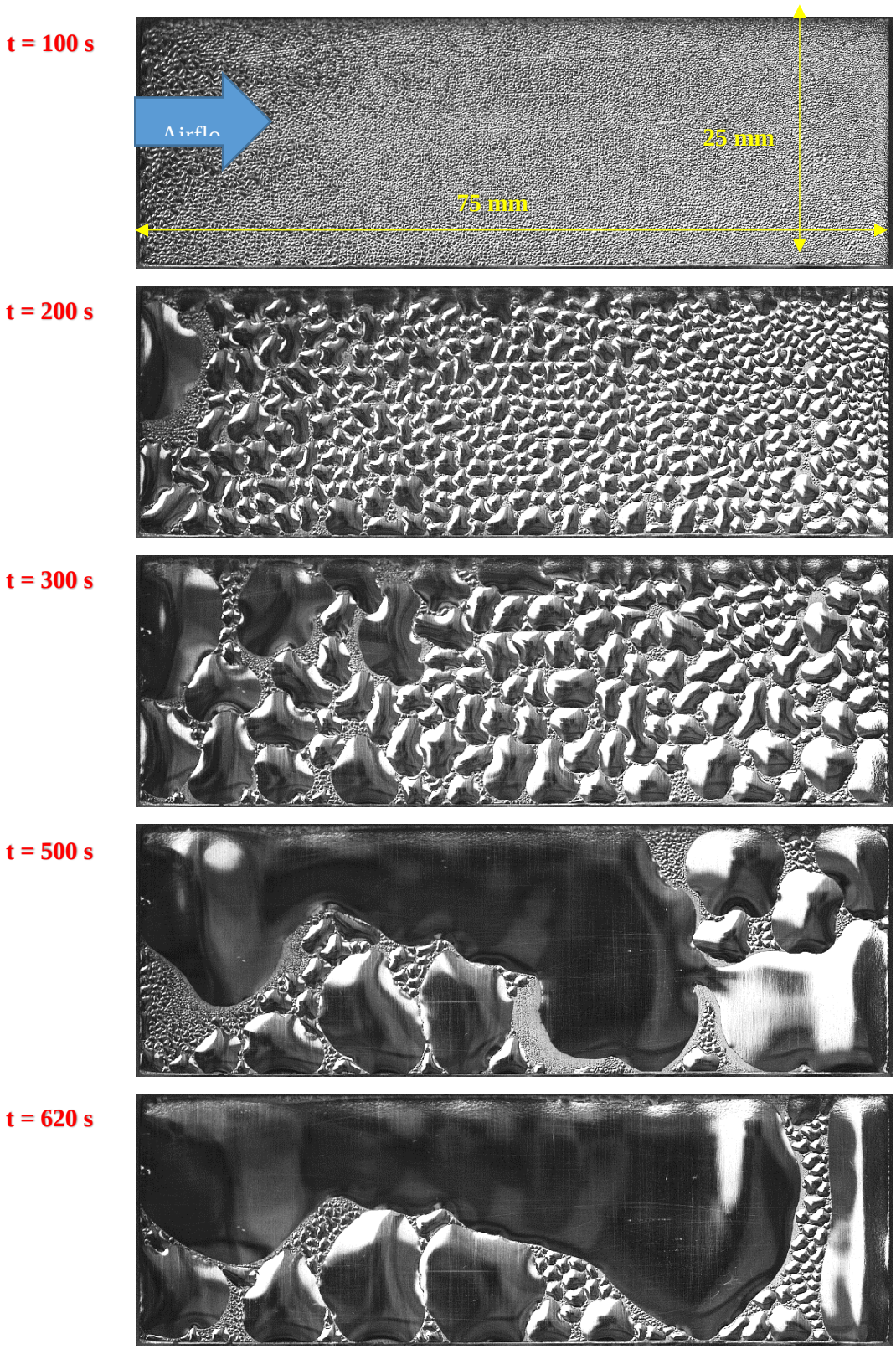

Figure 2.10. Condensate morphology on top of the surface in different time steps for airflow velocity of 10 m/s at RH = 80% and T_{sc} = 0°C.

At the time step of 500 s, the diameter of the droplets (equivalent diameter: $D = \sqrt{4.\text{Area}/\pi}$) was measured in the middle section of the surface (25 × 25 mm) using ImageJ, as shown in *Figure 2.11*. *Figure 2.12* shows the number of droplets versus the equivalent diameter for all velocities in the same mid-section. Although HTC increased by increasing the velocity, the larger size of droplets/puddles (higher rate of condensation without shedding) harmed the rate of increase. This is because the thermal resistance of a droplet typically increases with an increase in size and small droplets are favorable for having high HTC [35].

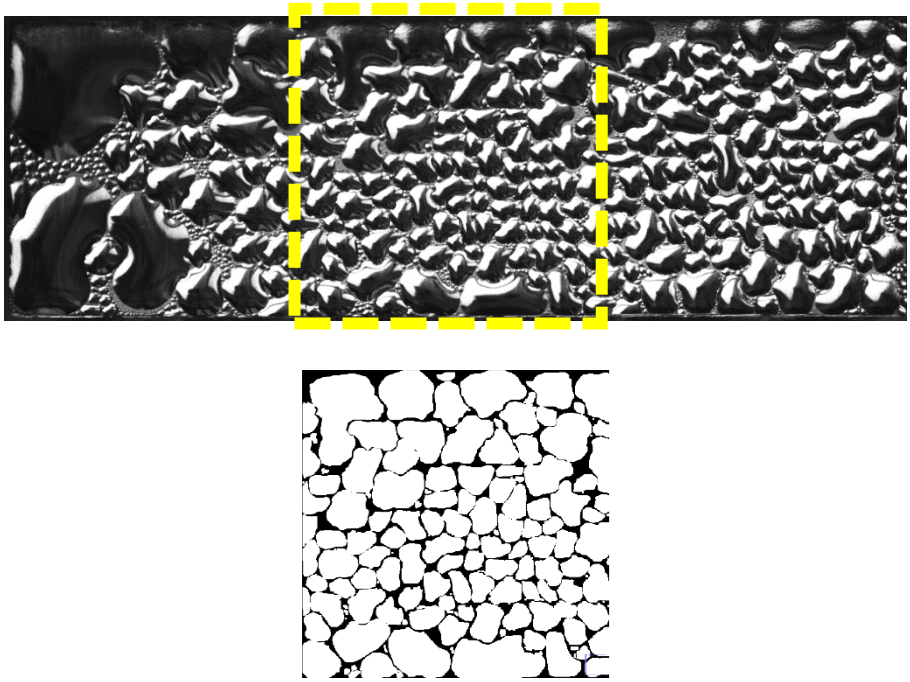

Figure 2.11. Condensate morphology on surface for the airflow velocity of 5 m/s at RH of 80% and subcooling of 0°C. The middle section of the surface (25 × 25 mm) was used and the time step was 500 s.

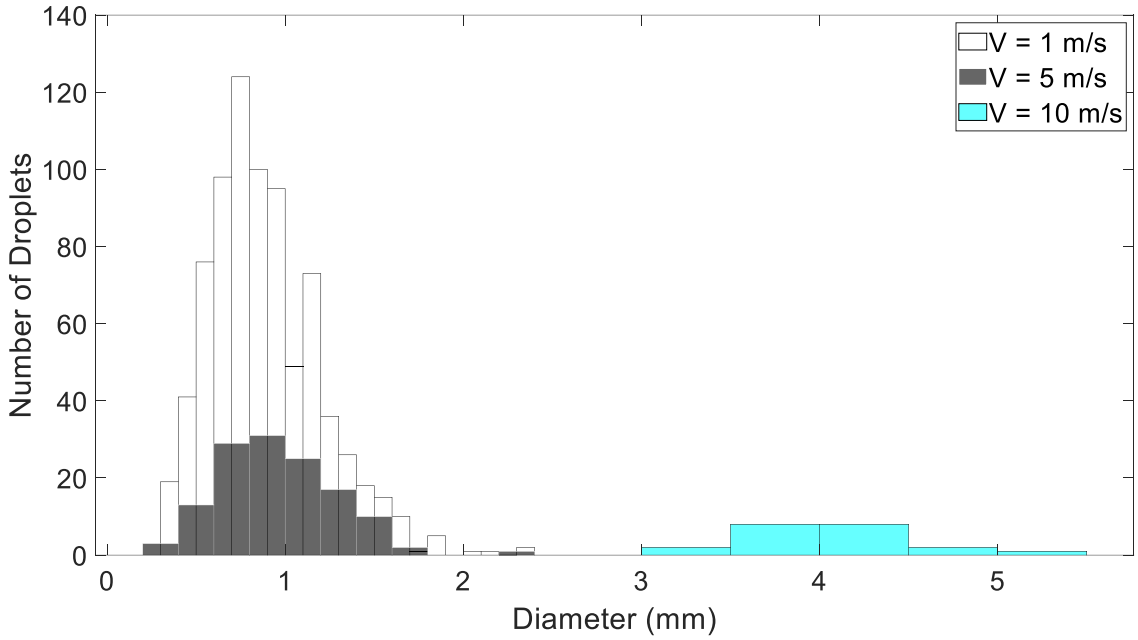

Figure 2.12. Droplet morphology equivalent drop for different velocities at RH of 80% and subcooling of 0°C.

To characterize the effect of air velocity and condensate morphology on HTC, the average Nu number of the condensation (after t = 500 s) versus the Re number is provided in *Figure 2.13* for different velocities, including the velocity of 15 m/s at which shedding was seen; points A, B, C, and D stand for the velocities of 1, 5, 10, and 15 m/s, respectively. From A to C (no shedding), Nu increased by increasing Re. However, the rate of increase is decreasing (the curvature is downward) because the size of the droplets increased (as seen in *Figure 2.12*). From point C to D (shedding), Nu increased, and the curvature is upward. The reason for this is the shedding of condensate due to the airflow.

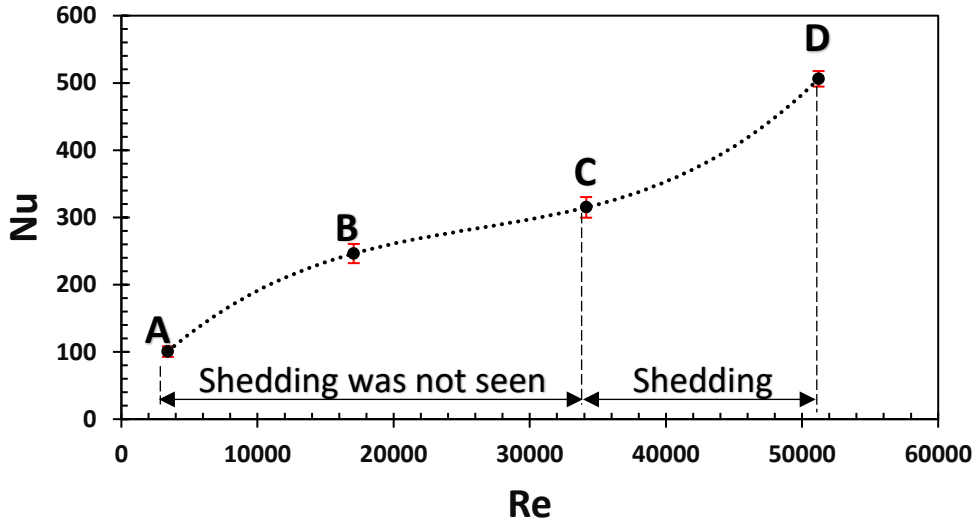

Figure 2.13. Average Nu number of the condensation versus the Re number. Points A, B, C, and D stand for the velocities of 1, 5, 10, and 15 m/s, respectively at RH=80% and $T_{sc} = 0°C$. From A to C, the increment rate HTC decreases due to the absence of shedding (larger condensate). From C to D, the increment rate HTC increases due to shedding (smaller condensate). Note that the trend line is to guide the eyes.

2.3.4 Effect of subcooling on condensation

Experiments were conducted to investigate the effect of subcooling on HTC. *Figure 2.14* shows that HTC for the subcooling of T = 0°C is smaller than for other T_{sc}, which was not expected. This is because T_{sc} changes the contact angle and consequently the circularity of the forming condensate baseline. The contact angle decreases by decreasing the substrate temperature [50]. The circular baseline is most compact in the sense that it encloses the most area for a given perimeter. Condensate morphology on the surface is compared in *Figure 2.16* for different values of T_{sc} in a time step of 500 s at V = 5 m/s and RH = 80%. As shown in *Figure 2.15*, HTC decreased by 20%, decreasing surface temperature from 5 to 0°C. However, the change is not noticeable from 10 to 5°C. The reason for this is that, as shown in *Figure 2.16*, non-circularity (i.e., deviation of cross-section from the form of a circle) of baseline increases by decreasing surface temperature. Condensate occupies more of the surface because of its twig shape and provides a less fresh surface

for the nucleation. However, circular condensate tries to be circular, even after coalescence, and provides a further fresh area for new nucleation.

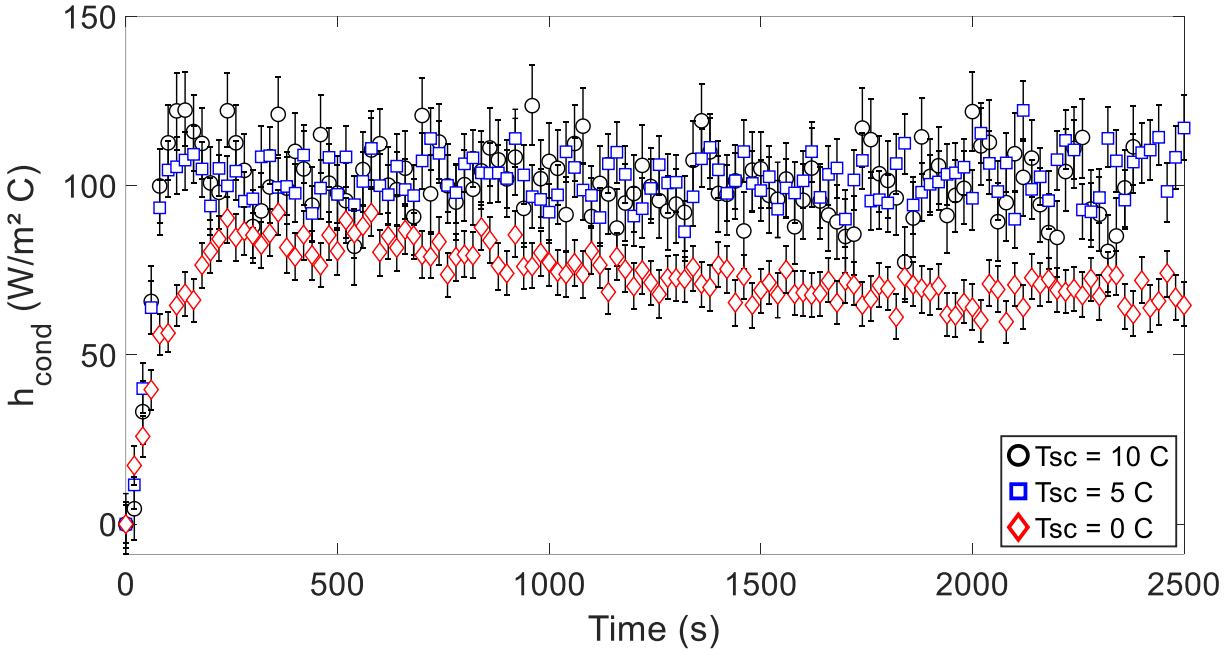

Figure 2.14. Condensation HTC versus time. These values are just HTC for condensation contribution.

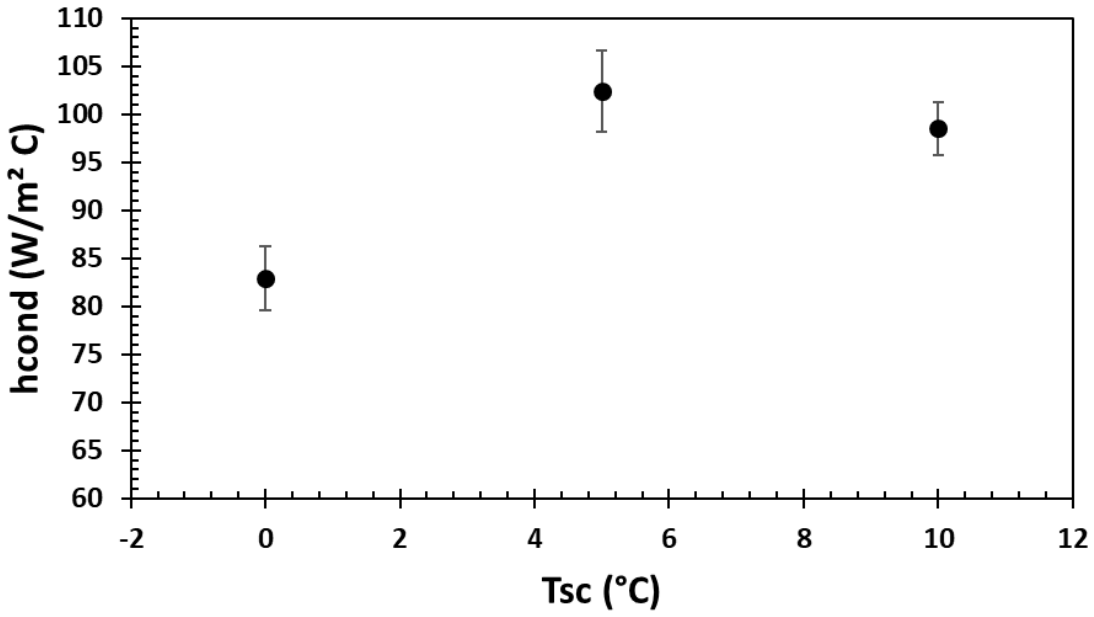

Figure 2.15. Condensation HTC versus subcooling. These values are just HTC for condensation contribution.

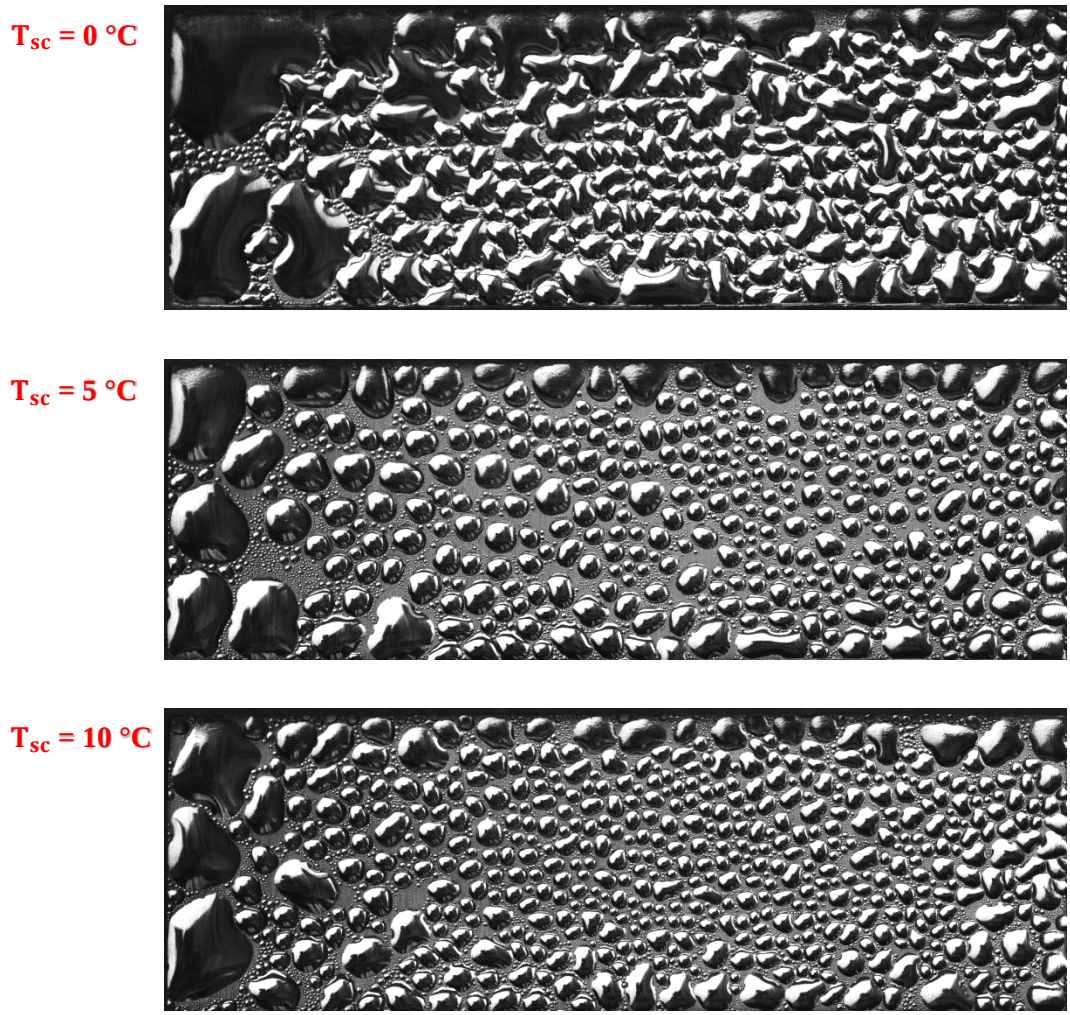

Figure 2.16. Condensate morphology on surface in time step = 500 s for airflow velocity of 5 m/s at RH = 80% at different T_{sc}.

2.3.5 Condensation regime identification

The results show that, for the same overall condensate morphology, different HTC is found at various conditions. Condensation regime classification was done based on droplet diameter to gain a better understanding between condensate morphology and HTC. Based on the average droplet diameter, four classifications were defined, as shown in *Figure 2.17*.

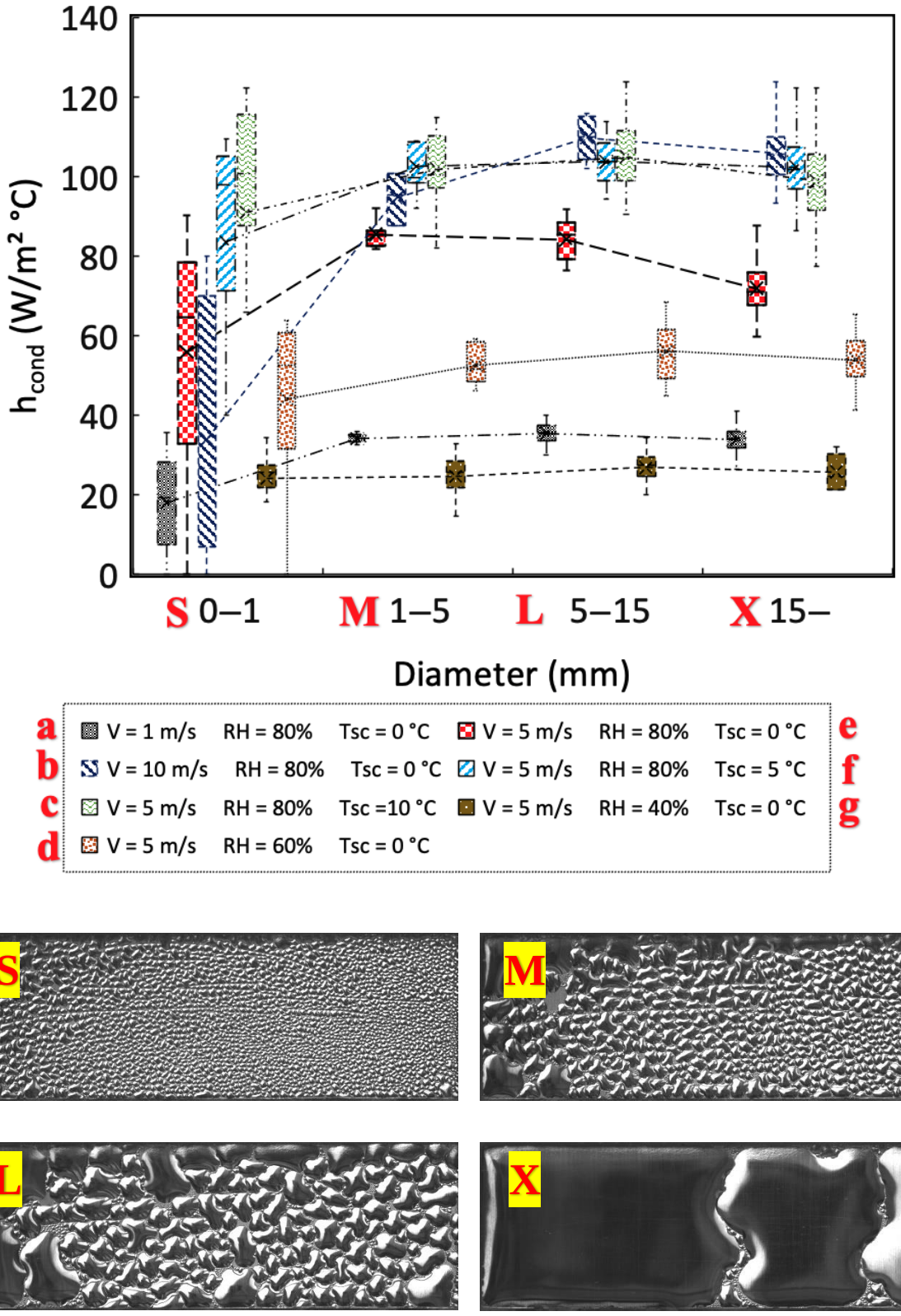

Figure 2.17. Condensation HTC distribution versus regimes based on condensate average droplet/puddle diameter at different conditions.

In the first three conditions (a–c), the effect of velocity was investigated. For condition (a) (V=1 m/s), the maximum variation of HTC happened at regime S, and then almost constant values were found during other regimes (M–X). In condition (b) (V=5 m/s), HTC was increased to the maximum value with a higher variation. However, by covering the surface in regime X, lower HTC was found. In condition (c) (V=10 m/s), the maximum value for HTC was obtained in regime L which showed a higher rate of condensation. Conditions (d) and (e) focused on the effect of subcooling comparing with (b). The results showed that higher subcooling is not always favorable. Higher subcooling (b) resulted in a change of regime from S to M and a decrease in HTC due to the surface covering. Conditions (f) and (g) demonstrated the effect of RH compared with the condition (b). For RH = 40% condensation morphology showed the same behaviour for HTC as with the constant distribution. RH = 60% has a slower change of HTC distribution for the different regimes.

The important point to note about all conditions is that the maximum HTC happened at regime S. Then, because there was no shedding, the regime switched one-by-one to finally reach the full coverage of the surface (regime X). The rest of the regimes either did not change HTC (or even did not let HTC increase) or led to a decreased HTC. *Figure 2.18* shows that the shedding (i.e., condition h) causes the condensation to remain at regime S and increases HTC. This clearly shows that the shedding of condensate kept the average droplet size low and doubled the improvement in heat transfer performance.

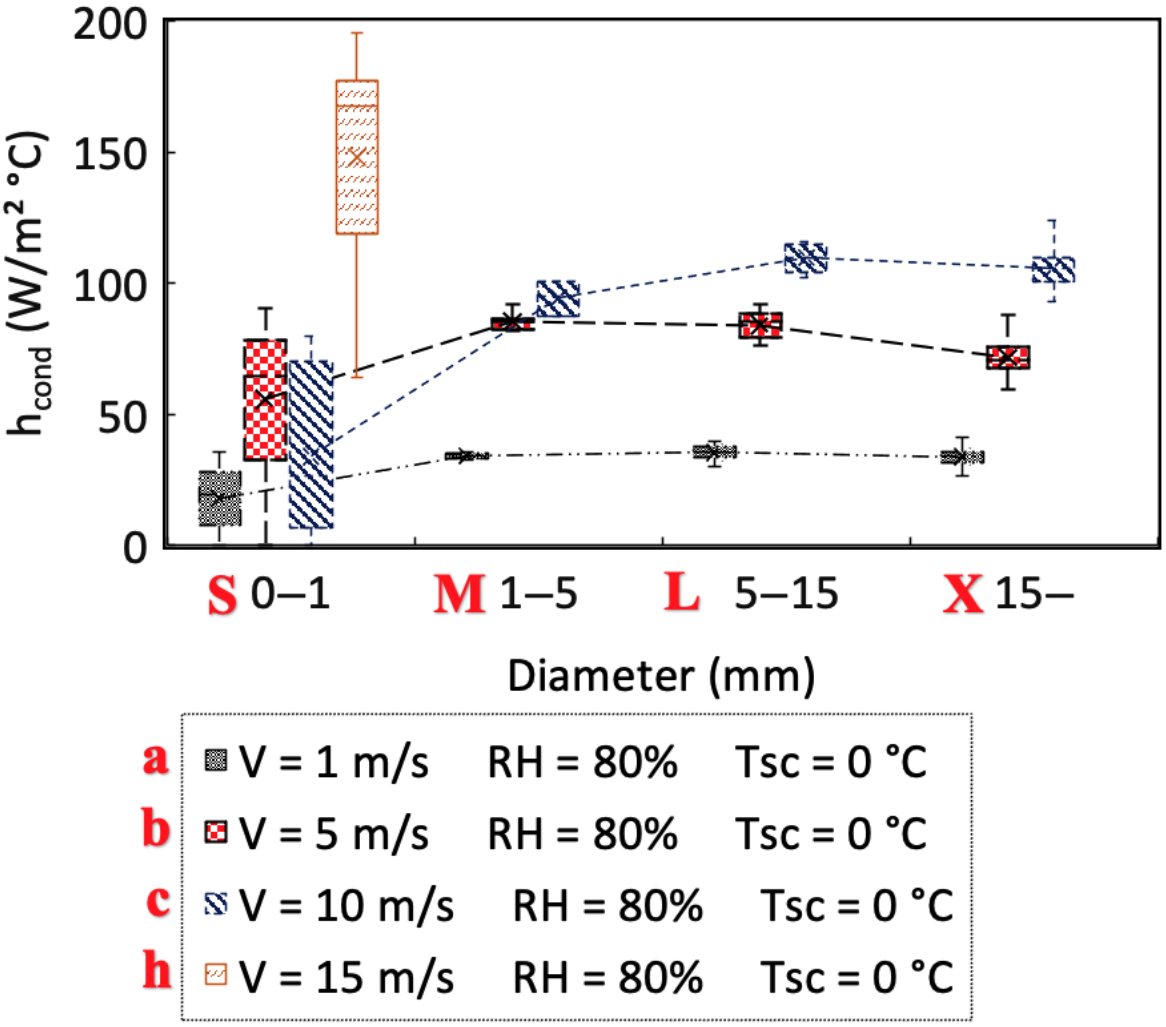

Figure 2.18. Condensation HTC distribution versus regimes based on condensate average diameter for different velocities. Condition h (V = 15 m/s) clearly shows that condensation stayed at regime S.

2.4 Conclusions

Effect of airflow on humid air condensation has received little attention thus far in the literature. Also, the effect of condensate morphology on heat transfer performance has not been addressed which requires transient heat transfer analysis. The current study focused on a systematic investigation of the influence of airflow and condensation parameters during humid air condensation on a horizontal surface at controlled conditions. The transient inverse heat conduction method was used to characterize the surface HF and associated HTC. It took approximately 5 s for

the system to respond, i.e., a 5-fold decrease in time seen for steady-state method. Also, it took approximately 30 s (~6 fold decrease) for the system to detect the change in HTC within 95%. Thus, using the transient inverse conduction method, time-varying HTC can be measured reasonably accurately to within 30 s. The results show that the effect of RH on condensation was investigated and higher HTC was found for higher RHs. Also, it was found that the effect of RH is significant in the DWC regime compared with the FWC regime. When coverage ratio and droplet size increase (finally reaches FWC), HTC decreases significantly for higher RHs compared with lower RHs. In addition, the results show that HTC for the subcooling of T = 0°C is smaller than for other temperatures. T_{sc} changes the circularity of the forming condensate and coverage ratio. A twig-shaped droplet was found for T_{sc} of 0°C; however, it was more circular for higher subcooling. Also, HTC for condensation contribution increased by increasing air velocity. However, the rate of increase for the velocities at which shedding was not seen decreased. In the case of shedding the slop of HTC increment, increased by increasing airflow velocity. The results clearly show that the shedding of condensate kept the average droplet size low and consequently, increased HTC by two-fold. The present work provides a fundamental basis for future condensation experiments to design surfaces that aim to optimize heat transfer performance. This basis helps one to investigate the effect of different coatings as well as electrowetting. Also, different environmental conditions and parameters such as RH, T_{sc}, velocity, and gravity can be characterized.

Acknowledgment

The authors acknowledge the funding of this work by NSERC and an Ontario Trillium Scholarship (MS).

2.5 References

[1] R. V Wahlgren, “Atmospheric water vapour processor designs for potable water production: a review,” Water Res., vol. 35, no. 1, pp. 1–22, 2001.

[2] D. Milani, A. Abbas, A. Vassallo, M. Chiesa, and D. Al Bakri, “Evaluation of using thermoelectric coolers in a dehumidification system to generate freshwater from ambient air,” Chem. Eng. Sci. J., vol. 66, pp. 2491–2501, 2011.

[3] R. L. Webb and K. Hong, “Performance of Dehumidifying Heat Exchangers With and Without Wetting Coatings,” in Transaction of the ASME, 1999, p. vol. 125, 1018-1026.

[4] S. Parekh, M. M. Faridb, J. R. Selmana, and S. Al-Hallaj"', “Solar desalination with a humidification-dehumidification technique-a comprehensive technical review,” Desalination, vol. 160, pp. 167–186, 2004.

[5] M.-H. Kim and C. W. Bullard, “Air-side performance of brazed aluminum heat exchangers under dehumidifying conditions,” Int. J. Refrig., vol. 25, no. 7, pp. 924–934, Nov. 2002.

[6] J. W. Rose, “Dropwise condensation. Heat Exchenger Design Handbook,” in Begell House, Begellhouse, 1998.

[7] I. Tanasawa, “Advances in Condensation Heat Transfer,” Adv. Heat Transf., vol. 21, pp. 55–139, Jan. 1991.

[8] M. Rama, N. Reddy, M. Yohan, and K. H. Reddy, “Heat Transfer Co-Efficient Through Dropwise Condensation and Filmwise Condensation Apparatus,” Int. J. Sci. Res. Publ., vol. 2, no. 12, 2012.

[9] J. W. Rose, “Dropwise condensation theory and experiment: A review,” Proc. Inst. Mech. Eng. Part A J. Power Energy, vol. 216, no. 2, pp. 115–128, 2002.

[10] P. Götze, C. Philipp, and U. Gross, “Dropwise Condensation Experiments with Humid Air at a Polymer Surface,” J. Phys. Conf. Ser., vol. 395, no. 1, p. 012129, Nov. 2012.

[11] S. Zheng, F. Eimann, C. Philipp, T. Fieback, and U. Gross, “Modeling of heat and mass transfer for dropwise condensation of moist air and the experimental validation,” Int. J. Heat Mass Transf., vol. 120, pp. 879–894, 2018.

[12] J. E. Castillo, J. A. Weibel, and S. V. Garimella, “The effect of relative humidity on dropwise condensation dynamics,” Biol. Control, vol. 80, pp. 759–766, 2015.

[13] S. Danilo, C. Dominique, and P. Frédéric, “Experimental dropwise condensation of unsaturated humid air – Influence of humidity level on latent and convective heat transfer for fully developed turbulent flow,” Int. J. Heat Mass Transf., vol. 102, pp. 846–855, 2016.

[14] J. W. Rose, “On the mechanism of dropwise condensation,” Int. J. Heat Mass Transf., vol. 10, no. 6, pp. 755–762, Jun. 1967.

[15] G. Koch, K. Kraft, and A. Leipertz, “Parameter study on the performance of dropwise condensation,” Rev. Générale Therm., vol. 37, no. 7, pp. 539–548, Jul. 1998.

[16] J. W. Rose, “Dropwise condensation theory and experiment: A review,” Proc. Inst. Mech. Eng. Part A J. Power Energy, vol. 216, no. 2, pp. 115–128, Jan. 2002.

[17] P. Meakin, “Steady state behavior in a model for droplet growth, sliding and coalescence: the final stage of dropwise condensation,” Phys. A Stat. Mech. its Appl., vol. 183, no. 4, pp. 422–438, May 1992.

[18] C. Dietz, K. Rykaczewski, a G. Fedorov, and Y. Joshi, “Visualization of droplet departure on a superhydrophobic surface and implications to heat transfer enhancement during dropwise condensation,” Appl. Phys. Lett., vol. 97, no. 3, pp. 33103–33104, 2010.

[19] S. Daniel, M. K. Chaudhury, and J. C. Chen, “Fast drop movements resulting from the phase change on a gradient surface.,” Science, vol. 291, no. 5504, pp. 633–637, Jan. 2001.

[20] P. S. Mahapatra, A. Ghosh, R. Ganguly, and C. M. Megaridis, “Key design and operating parameters for enhancing dropwise condensation through wettability patterning,” Int. J. Heat Mass Transf., vol. 92, pp. 877–883, Jan. 2016.

[21] A. Ghosh, S. Beaini, B. J. Zhang, R. Ganguly, and C. M. Megaridis, “Enhancing dropwise condensation through bioinspired wettability patterning,” Langmuir, vol. 30, no. 43, pp. 13103–13115, 2014.

[22] A. M. Macner, S. Daniel, and P. H. Steen, “Condensation on Surface Energy Gradient Shifts Drop Size Distribution toward Small Drops,” Langmuir, vol. 30, no. 7, pp. 1788–1798, Feb. 2014.

[23] J. Feng, Z. Qin, and S. Yao, “Factors Affecting the Spontaneous Motion of Condensate Drops on Superhydrophobic Copper Surfaces,” Langmuir, vol. 28, no. 14, pp. 6067–6075, Apr. 2012.

[24] J. Feng, Y. Pang, Z. Qin, R. Ma, and S. Yao, “Why Condensate Drops Can Spontaneously Move Away on Some Superhydrophobic Surfaces but Not on Others,” ACS Appl. Mater. Interfaces, vol. 4, no. 12, pp. 6618–6625, Dec. 2012.

[25] J. B. Boreyko and C.-H. Chen, “Self-Propelled Dropwise Condensate on Superhydrophobic Surfaces,” Phys. Rev. Lett., vol. 103, no. 18, Oct. 2009.

[26] R. Enright, N. Miljkovic, J. Sprittles, K. Nolan, R. Mitchell, and E. N. Wang, “How Coalescing Droplets Jump,” ACS Nano, vol. 8, no. 10, pp. 10352–10362, Oct. 2014.

[27] T. Q. Liu, W. Sun, X. Y. Sun, and H. R. Ai, “Mechanism study of condensed drops jumping on super-hydrophobic surfaces,” Colloids Surfaces A Physicochem. Eng. Asp., vol. 414, pp. 366–374, Nov. 2012.

[28] A. J. B. Milne and A. Amirfazli, “Drop Shedding by Shear Flow for Hydrophilic to Superhydrophobic Surfaces †,” Langmuir, vol. 25, no. 24, pp. 14155–14164, Dec. 2009.

[29] A. Razzaghi, A. Amirfazli, Shedding of a pair of sessile droplets, Int. J. Multiph. Flow 110 (2019) 59–68. [30]

[30] A. Razzaghi, S.A. Banitabaei, A. Amirfazli, Shedding of multiple sessile droplets by an airflow, Phys. Fluids 30 (2018) 087104.

[31] C. Graham and P. Griffith, “Drop size distributions and heat transfer in dropwise condensation,” Int. J. Heat Mass Transf., vol. 16, no. 2, pp. 337–346, Feb. 1973.

[32] J. W. Rose, “Condensation Heat Transfer Fundamentals,” Chem. Eng. Res. Des., vol. 76, no. 2, pp. 143–152, Feb. 1998.

[33] S. Lee, H. K. Yoon, K. J. Kim, S. Kim, M. Kennedy, and B. J. Zhang, “A dropwise condensation model using a nano-scale, pin structured surface,” Int. J. Heat Mass Transf., vol. 60, pp. 664–671, May 2013.

[34] D. Attinger et al., “Surface engineering for phase change heat transfer: A review,” MRS Energy Sustain., vol. 1, pp. 1–40, Nov. 2014.

[35] B. Peng, X. Ma, Z. Lan, W. Xu, and R. Wen, “Analysis of condensation heat transfer enhancement with dropwise-filmwise hybrid surface: Droplet sizes effect,” Int. J. Heat Mass Transf., vol. 77, pp. 785–794, 2014.

[36] I. Mohammed, A. R. A. Talib, M. T. H. Sultan, and S. Saadon, “Temperature and heat flux measurement techniques for aeroengine fire test: A review,” IOP Conf. Ser. Mater. Sci. Eng., vol. 152, no. 1, 2016.

[37] D. G. Walker, “Heat flux determination from measured heating rates using thermographic phosphors,” J. Heat Transfer, vol. 127, no. 6, pp. 560–570, Jun. 2005.

[38] K. S. Yang, K. H. Lin, C. W. Tu, Y. Z. He, and C. C. Wang, “Experimental investigation of moist air condensation on hydrophilic, hydrophobic, superhydrophilic, and hybrid hydrophobic-hydrophilic surfaces,” Int. J. Heat Mass Transf., vol. 115, pp. 1032–1041, 2017.

[39] A. Yamauchi, S. Kumagai, and T. Takeyama, “Condensation heat transfer on various dropwise-filmwise coexisting surfaces.,” Heat Transf. - Japanese Res., vol. 15, no. 5, pp. 50–64, Sep. 1986.

[40] A. Ghosh, S. Beaini, B. J. Zhang, R. Ganguly, and C. M. Megaridis, “Enhancing Dropwise Condensation through Bioinspired Wettability Patterning,” Langmuir, vol. 30, no. 43, pp. 13103–13115, Nov. 2014.

[41] D. F. Othmer, “The Condensation of Steam,” Ind. Eng. Chem., vol. 21, no. 6, pp. 576–583, Jun. 1929.

[42] D. W. Tanner, D. Pope, C. J. Potter, and D. West, “Heat transfer in dropwise condensation at low steam pressures in the absence and presence of non-condensable gas,” Int. J. Heat Mass Transf., vol. 11, no. 2, pp. 181–190, Feb. 1968.

[43] S. Oh and S. T. Revankar, “Experimental and theoretical investigation of film condensation with noncondensable gas,” Int. J. Heat Mass Transf., vol. 49, no. 15–16, pp. 2523–2534, Jul. 2006.

[44] X.-H. Ma, X.-D. Zhou, Z. Lan, Y.-M. LI, and Y. Zhang, “Condensation heat transfer enhancement in the presence of non-condensable gas using the interfacial effect of dropwise condensation,” Int. J. Heat Mass Transf., vol. 51, no. 7–8, pp. 1728–1737, Apr. 2008.

[45] R. Kempers, P. Kolodner, A. Lyons, and A. J. Robinson, “A high-precision apparatus for the characterization of thermal interface materials,” Rev. Sci. Instrum., vol. 80, no. 9, p. 095111, Sep. 2009.

[46] R. D. Mehta and P. Bradshaw, “Design rules for small low speed wind tunnels,” Aeronaut. J., vol. 83, no. 827, pp. 443–453, 1979.

[47] E. B. Coy, “Measurement of transient heat flux and surface temperature using embedded temperature sensors,” J. Thermophys. Heat Transf., vol. 24, no. 1, pp. 77–84, 2010.

[48] S. J. Kline and F. A. McClintock, “Describing uncertainties in single-sample experiments,” Mech. Eng., vol. 75, no. 1, pp. 3–8, 1953.

[49] J. I. Frankel, “Regularization of inverse heat conduction by combination of rate sensor analysis and analytic continuation,” J. Eng. Math., vol. 57, no. 2, pp. 181–198, Feb. 2007.

[50] K. Terpiłowski, “Influence of the ambient temperature on water and diiodomethane contact angle with quartz surface,” Ann. UMCS, Chem., vol. 70, no. 1, 2015.

Chapter 3 Experimental Investigation of Dropwise Condensation Shedding by Shearing Airflow in Microgravity Using Different Surface Coatings

3.1 Introduction

Dropwise condensation (DWC) is a superior mode of heat transfer to its alternative, i.e., filmwise condensation (FWC). The increase in heat transfer coefficient (HTC) can be at least ten times higher for DWC versus FWC [1]. DWC can improve heat transfer performance in almost all processes that involve a phase change [2], making its successful application a significant goal for the energy sector [3] (e.g., for power plants, the chemical industry [2], water desalination [4], and HVAC systems [5]). This latter point directly relates to the environmental control and life support system (ECLSS) in space vehicles. Also, DWC can be found in other applications related to reduced gravity environments, such as thermal management systems for satellites, power management systems, and wastewater treatment for manned space platforms. The high HTC seen in systems with DWC also means that these systems can be miniaturized, making them lighter. This is essential for space application—an area in which one of the goals for system design is the minimization of a system's weight. However, the condensation phenomenon at the liquid–vapor interface in zero gravity (i.e., space applications) is not well understood. Therefore, it is necessary to understand humid air condensation in a microgravity environment.

Shedding (i.e., droplet movement under the effect of air shear flow) of droplets from a surface is a critical part of the DWC process that improves heat transfer. The majority of DWC systems take advantage of gravity by causing drops to shed from the surface of a condenser before they grow too large and connect to create a film [6–8]. However, for space applications, gravity is not available [9]. A surface energy gradient has been suggested as a way to remove drops [10–11];

however, there can be significant limitations on the distances that drops can be transported on such surfaces. Alternatively, one can take advantage of aerodynamic forces and remove/shed droplets from a surface using a stream of air (note that in ECLSS, an air stream is usually present) [12].

Droplet shedding is mainly determined by adhesion and drag forces. The adhesion force (F_{adh}) is the force that attaches the droplet to the surface; the lateral (i.e. in the plane of the surface) adhesion force, $(F_{adh})_{Lateral}$ is a function of contact angle (θ), surface tension (σ), and the wetting length (L_w) of the droplet [13]. When a droplet is exposed to a shear flow, the shape of the droplet deforms in such a way that the upstream contact angle (θ_{min}) decreases, and the downstream contact angle (θ_{max}) increases compared with the static contact angle (θ). F_{adh} can be described by the following correlation:

$$(F_{adh})_{Lateral} \propto L_w \sigma (cos\theta_{min} - cos\theta_{max}) \tag{3.1}$$

The drag force (F_{drag}) applied on a droplet due to a shear flow can be described by the following correlation:

$$F_{drag} \propto 1/2 C_D \rho u_{air}^2 S \tag{3.2}$$

where C_D is the drag coefficient, ρ is the air density, u_{air} is the free stream velocity, and S is the frontal area (i.e., the area of the droplet that is facing the airflow). When the shear flow is increased over a droplet, drag force rises accordingly. The opposing lateral adhesion force also increases proportionally. When the airflow is increased to the point of incipient motion of the droplet, the lateral adhesion force is equal to the drag force. The airflow speed associated with the incipient motion is called the critical velocity (u_{cri}). The lateral adhesion force cannot further increase after u_{cri}, and the droplet moves along the surface. The balance of the forces in the horizontal direction is as follows:

$$\begin{cases} (F_{adh})_{Lateral} = F_{drag} & Up\ to\ incipient\ motion, and\ at\ the\ critical\ velocity \\ (F_{adh})_{Lateral} < F_{drag} & After\ critical\ velocity \end{cases} \quad (3.3)$$

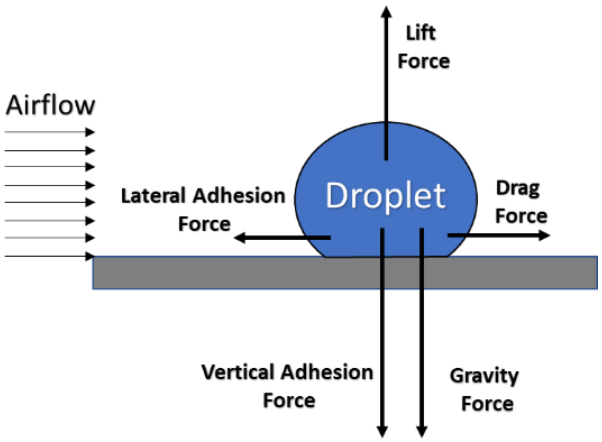

Figure 3.1. Schematic of a droplet and associated forces due to airflow, wettability, and gravity

The droplet also experiences a vertical adhesion, gravity, and lift (for contact angle > 90˚) forces in the vertical direction. When the lift force overcomes the vertical adhesion and gravity forces, the droplet can be detached (i.e., entrained) from the substrate. The balance of the forces in the vertical direction is as follows:

$$\begin{matrix} (F_{adh})_{Vertical} + F_{gravity} \geq F_{Lift} & Droplet\ stays\ attched\ to\ the\ substrate \\ (F_{adh})_{Vertical} + F_{gravity} < F_{Lift} & Detachment\ of\ droplet \end{matrix} \quad (3.4)$$

The use of surface coatings can increase or reduce the force requirements for the shedding by the airflow process. Adhesion of the droplets is a function of surface properties [14] and, indirectly, the condensing period (size of the contact line and change in contact angle [15]). Also, the surface's wettability will significantly affect the size of condensating droplets and the adhesion of droplets onto the surface [15]. The question of how the adhesion force of droplets can be overcome by aerodynamic forces, so they can be shed, needs to be answered. There are three possible shedding regimes for the droplet under aero- or hydro-dynamic forces: sliding, deformation–sliding, and

deformation–sliding–detachment [16]. The results show that sliding of condensate improves HTC by providing a fresh area for condensation. One might assume that the detachment of droplets would also offer a fresh area for the condensation cycle; however, when a large droplet detaches, its chance to sweep away most of the tiny droplets as it sheds away while attached to the surface, will be lost. Therefore, the detachment of droplets from the substrate will hamper this process that can produce a larger fresh area; also, detachment of droplets and entrainment in airflow, regrates the concept of removing moisture from the air in a dehumidification process by condensation.

Substrates with lower surface energy provide a higher possibility of shedding due to a lower lateral adhesion force. Therefore, a higher frequency condensation cycle augments the HTC. On the other hand, such substrates have a lower vertical adhesion force and present a higher possibility of droplet detachment, especially in a microgravity environment. Therefore, the main question to answer is whether the vertical adhesion of droplets in the presence of airflow will be strong enough, in microgravity conditions, to avoid detachment.

In principle, it should be possible to mimic reduced gravity conditions in ground-based applications for deposited droplets; on-ground experiments have demonstrated lift-off of droplets when the droplet density and shearing medium are close [16]. However, in condensation applications, unavoidable differences in the air density and viscosity with water mean that on-ground experiments cannot answer the question of entrainment. Also, detachment of droplets can be seen, if the droplet bursts (i.e., high-speed airflow impulse) [17]. However, a burst droplet situation does not address the concern of condensate detachment because it is not a realistic situation for condensation; as such, there is a need for microgravity tests. A parabolic flight (PF) was used to simulate microgravity (weightlessness) to perform experiments under microgravity

conditions. In PF, an aircraft flies a parabolic trajectory, providing reduced gravity for up to 23 s [18].

Only a few studies exist on the influence of microgravity on the shape of droplets. Brutin et al. [19] performed fundamental experiments on sessile drop creation in microgravity. They focused on investigating the drops' interaction with a solid surface (i.e., contact angle) in reduced gravity levels. Three different fluids (de-ionized water, HFE-7100, and FC-72) and two surfaces (aluminium and PTFE) were used in their study. The results show that contact angle behaviour depends on the drop diameter and gravity level. They found that the contact angle can be 10˚ lower for a drop created under normal gravity than the same drop created in microgravity. Drop pressure change through hydrostatic pressure is a possible explanation for the drop contact angle change. Diana et al. [20] characterized droplet shape (contact angle and wetted perimeter) for drops of water and ethanol on aluminium and PTFE substrates under normal gravity and reduced gravity. The wetting diameter and height are related to the surface energy to obtain the lowest free energy shape (spherical cap). The wetting perimeter of the drops was found to be lower in reduced gravity when compared with normal gravity. Also, they discovered that the Young–Laplace equation was not optimal for describing the contact angle for large drops. However, the issue of how reduced gravity can promote droplet lift-off was not addressed in their study.

The current study aims to develop an understanding and evaluation of the shedding of condensate when exposed to airflow (aerodynamic forces) in a microgravity environment. Therefore, an experimental study was developed to characterize the condensation kinematic in a microgravity environment. The goal of this study is to determine which coating facilitates the shedding of droplets at a low required air velocity without causing the droplets to lift off the surface.

This knowledge will underpin the design of condensers that can work under microgravity conditions and in DWC mode.

3.2 Methods and materials

An experimental setup, a mini closed-loop wind tunnel, was designed to investigate the effect of gravity on the shedding of condensate. Condensation took place on a cooled horizontal surface inside the test section. The measurement of parameters such as air velocity, relative humidity (RH), and gravitational acceleration was synchronized to the flow visualization (top and side views of the test section) to characterize gravity's effect on the shedding of droplets. The centroid of the droplet was considered a reference point, and image processing with MATLAB was performed to follow the droplet movement. *Figure 3.2* shows the line passing through the reference point and the direction of the displacement. The criterion for movement inception (shedding) of the centroid of the droplet was considered to be 10 px (equivalent to 500 µm; pixel density: 50 ± 0.25 µm/px) [21]–[23].

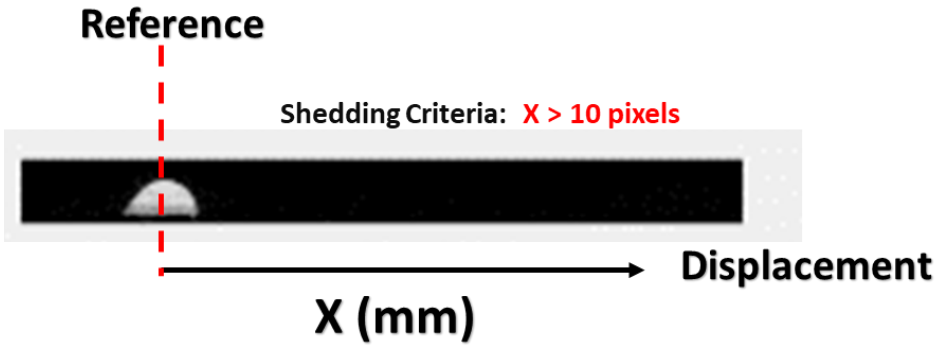

Figure 3.2. The reference point and the direction of the displacement. The shedding criterion is 10 px.

3.2.1 Setup preparation

The main part of the experimental setup, the wind tunnel, was designed to control RH (ambient–99%), airflow velocity (0–25 m/s), and surface temperature (0–50°C) to simulate the condensation environment. A PF that was part of the European Space Agency (ESA) 73th PF campaign framework in November 2020 was used to simulate a microgravity environment. The duration of microgravity was limited to approximately 22 s. Due to the time limitation, a single drop was seeded on the condensating surface because condensation is a time-consuming process. Therefore, the droplet injection system was designed to deposit a droplet of a specific volume on the condensing surface. This enabled us to generate an artificial droplet on top of condensate and to save time. A schematic diagram and the experimental facility are shown in *Figure 3.3*. The test section was 150 mm long with a cross-section of 50×50 mm. The substrate size was 25×75 mm, located at 20% of the test section's hydraulic diameter after the flow straightener (developing length) to ensure that the non-uniformities of the flow settled [24]. The bottom surface had a cartridge-like subsystem that enabled easy replacement of substrates between parabolas in the flight. The aluminium substrates were fitted to grooves in a cartridge. This subsystem was also equipped with a rail fixed to the bottom of the test section (*Appendix D: Test section*) for details.

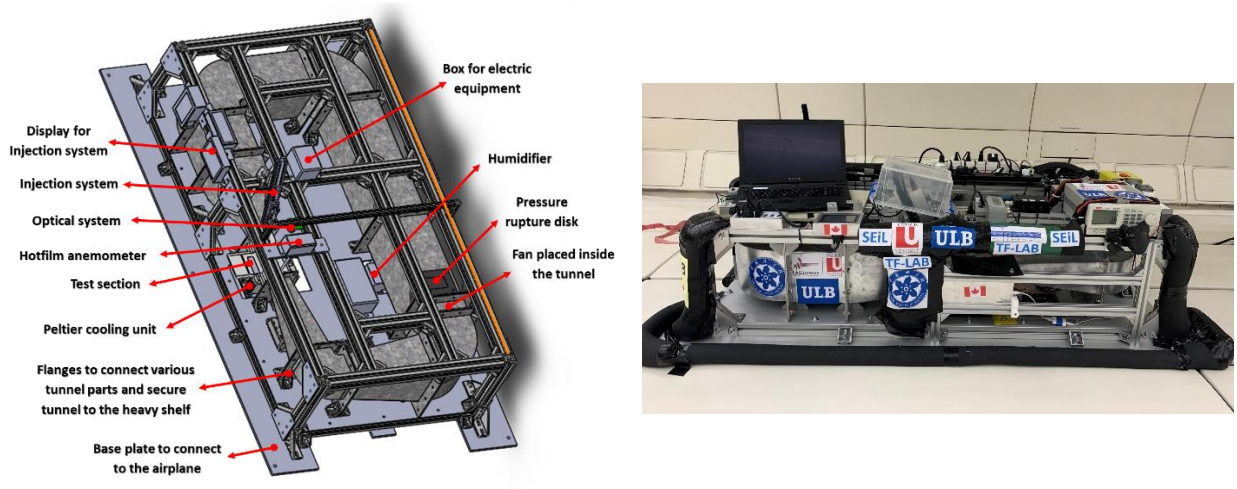

Figure 3.3. Schematic diagram and the actual experimental facility, onboard of the airplane.

Airflow velocity was controlled by a programmable switching DC power supply (IPS-603, RS Pro) which could change the speed of the fan (MM1865 Series, Mechatronics Inc.). The airflow velocity was measured by a hot-film anemometer (EE75, E+E Elektronik Ges.m.b.H) with an accuracy of ±0.2 m/s (see details in *Appendix E: Velocity control system (VCS)*). The airflow inside the tunnel was humidified using ultrasonic atomizers. The RH was continuously measured and controlled using a programmable humidity controller (HD220, Auber). A closed-loop feedback system controlled the introduction of humidity in the closed-loop tunnel. The control system was capable of maintaining RH in a range between ambient and 99% with an accuracy of ±4% (see details in *Appendix F: Humidity control system (HCS)*). The temperature control system was designed to control the temperature of the substrate. The substrate temperature was controlled by a Peltier cell, using closed-loop feedback and a PID algorithm (see details in *Appendix G: Temperature control system (TCS)*). Flow visualization was carried out using two cameras (M1280, Genie Nano) which were vertically and horizontally mounted; the field of view was 75 mm (lens: 12 mm/F1.8 VS-1218VM, VS Technology). The captured images were calibrated using a grid array (R1L3S3, THORLABS). The average resolution for the side view was 50 ± 0.25 μm/px, and for

the top view was 65 ± 0.42 μm/px. The droplet injection subsystem consisted of a syringe, syringe pump (stepper motor), and linear slider to provide the syringe pump with linear movement (see details in *Appendix H: Droplet injection system*).

A computer powered the hardware via an Arduino board and a joystick (PlayStation). The voltage applied to the fan was controlled by software via an RS232 connection. The Arduino board (Arduino Mega) controlled the syringe pump and collected experimental data: time (for synchronization with the cameras), gravity levels, and power for the fan. Commercial software (StreamPix) was used to drive the two cameras. The software overlaid the date and time on the images; these were further synchronized with the gravity levels along the three axes. Finally, the whole experimental setup and operation were controlled by the joystick interface.

3.2.2 Substrate preparation

To obtain the same morphology, the aluminium substrate was polished with sandpapers (#800, # 1200, # 2000, # 4000, and # 8000). Then, roughness measurements were performed using a surface profiler (Dektak 150). The measurements were carried out in the three sections (left, middle, and right) across the substrate length (75 mm) for a length of 55 mm. The process was repeated three times for all substrates, and the average roughness measured was 20 ± 1 nm.

A wide range of contact angles (60˚–160˚) were tested to find the balance between the vertical and horizontal adhesion forces. The aluminium surfaces produced were coated as follows: poly methyl methacrylate (PMMA, $\theta_r = 60° \pm 1°$ and $\theta_a = 80° \pm 1°$), polystyrene (PS, $\theta_r = 70° \pm 1°$ and $\theta_a = 90° \pm 1°$), dry PTFE spray (PTFE, $\theta_r = 80° \pm 1°$ and $\theta_a = 110° \pm 1°$), and NeverWet spray (SHS, $\theta_r > 160°$ and $\theta_a > 160°$). A spin-coating technique was used to fabricate

PMMA and PS surfaces. However, spraying was used for the PTFE and SHS surfaces. Detailed information on surface fabrication is provided in *Table 3.A*.

Table 3.A. Detailed information on surface fabrication

Surface Name	Method	Material and Fabrication Details
PMMA	Spin coat	**Solution:** 2wt% of PMMA (Aldrich Mw~120000) in toluene **Spin coater speed:** 2000 RPM **Spin time:** 60 s
PS	Spin coat	**Solution:** 1wt% of PS (Aldrich Mw~35000) in toluene **Spin coater speed:** 2000 RPM **Spin time:** 60 s
PTFE	Spray coat	**Material:** Dry PTFE spray (ROCOL)
SHS	Spray coat	**Material:** Neverwet spray (Rust-Oleum)

3.3 Results and discussion

We conducted ground-based research as a reference for comparison with the results from reduced gravity. In the ground-based experiments, airspeeds between 3 m/s and 15 m/s caused droplet shedding for all four substrates. Such airspeeds were necessary to overcome the horizontal adhesion force of a droplet onto the substrate. Microgravity tests were carried out to determine, if these speeds would not suffice to lift droplets from the surface in reduced gravity. Based on our experience from the ground-based experiments [25], we chose to conduct the tests at a humidity level of 80% because this would provide a higher rate of condensation and yet would not create fog on the walls of the test section.

3.3.1 Drop shape

Consider a stationary droplet on a horizontal flat surface, and gravity acts downward, perpendicular to the surface. A spherical cap can be used to approximately model the droplet (see *Figure 3.4*), where R_c is the characteristic length, r, is the radius of the contact line, h, is the height of the droplet, and θ_c is the contact angle. The force balance at the liquid–air interface determines the equilibrium shape of the droplet. The Young–Laplace equation expresses the balance due to the pressure difference across the interface by surface tension and gravity forces. Gravity causes hydrostatic pressure inside the droplet. The dimensionless Bond number, $Bo = \frac{\rho g {R_c}^2}{\gamma}$, determines the strength of gravitational force relative to the surface tension force, where ρ, g, and γ represent the liquid density, gravity acceleration, and surface tension, respectively. In zero gravity (i.e., Bo = 0), hydrostatic pressure becomes zero and, the mean curvature of the droplet stays constant, leading the droplet to have a spherical cap shape; the contact angle (depending on the wetting properties of the substrate) will determine the spherical cap shape for a given drop volume. In the presence of gravity (i.e., Bo is finite), the drop shape deviates from a spherical cap, because the hydrostatic pressure is no longer zero.

Volume and characteristic length can be calculated using the equations below:

$$V = \frac{1}{6}\pi h(3r^2 + h^2) \qquad R_c = \frac{r^2+h^2}{2h} \tag{3.5}$$

The volume of the droplet (V), the radius of the contact line (r), and the height of the droplet are normalized as follows:

$$\boldsymbol{\mathcal{R}} = \frac{r}{R_c} = sin\theta_c \qquad \boldsymbol{\mathcal{V}} = \frac{V}{{R_c}^3} = ({}^{\pi}/_{3})(2 + cos\theta_c)(1 - cos\theta_c)^2 \qquad \boldsymbol{\mathcal{H}} = \frac{h}{R_c} \tag{3.6}$$

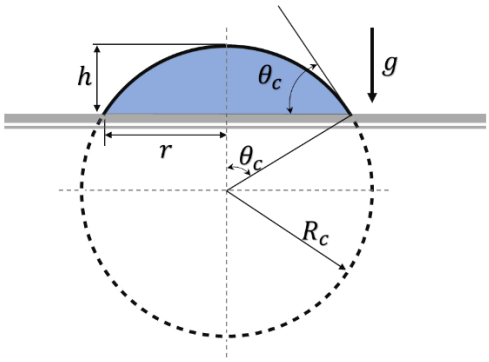

Figure 3.4. A stationary droplet on a horizontal flat surface. The droplet is modelled as a spherical cap, which is a sphere cut off by the surface, where R_c is the characteristic length, r is the radius of the contact line, h is the height of the droplet and θ_c is the contact angle. A downward arrow shows the gravity vector g.

3.3.2 Effect of microgravity on droplet geometry

When the droplet is in microgravity, the contact angle and wetting length can change [19], potentially altering the balance of forces for droplet shedding. Therefore, shape analysis is an essential step to understand the effect of gravity on the shedding behavior of droplets (the primary objective of this study). The shape analysis for the 40 µL size droplet on a PTFE coating is discussed as an example. *Figure 3.5-a* illustrates the droplet profile in microgravity and normal gravity (ground). For the same volume of 40 µL, the radius of the contact line (wetting length) of the droplet in microgravity is 8% lower (i.e., 0.45 mm) than in normal gravity. Also, the droplet in the microgravity condition has a contact angle that is 15% higher (i.e., 12 degrees). Note that the droplet was assumed to be axisymmetric in our calculations. Also, the gravity was 0.22g for microgravity at the moment of increasing the airflow velocity. The adhesion force of the droplet is proportional to the wetting length (L_w) and contact angle (*Eq. 3.1*). A lower wetting length and higher contact angle in microgravity should provide for a lower horizontal adhesion force.

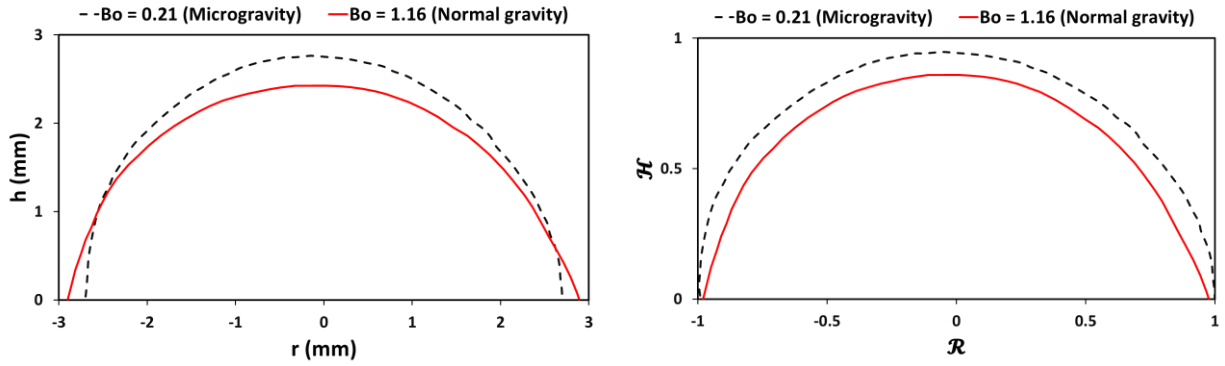

(a) (b)

Figure 3.5. Shape analysis for the 40 µL size droplet on PTFE coating (a) Droplet profile in microgravity and normal gravity (ground); r is the radius of the contact line, and h is the height of the droplet. (b) Dimensionless plot for the same droplet for the identical condition, $\mathcal{R}$ is the normalized radius of the contact line, and $\mathcal{H}$ is the normalized height of the droplet. The gravity vector, g, is downward.

Figure 3.5-b shows the dimensionless plot for the same droplet for an identical condition. The normalized height of a droplet for microgravity is higher than for normal gravity. The drag force for droplet shedding is proportional to the frontal area (S) of the droplet. Due to higher normalized height at the same normalized wetting length, the drag force is higher for the droplet in the microgravity environment. Note that the shape in *Figure 3.5-b* does not represent the actual volume for droplets. Taken all above discussion, the droplet in microgravity is expected to have a lower horizontal adhesion force and undergoes higher drag force compared with the normal gravity conditions. Also, as the contact angle increases in microgravity, the lift force increases because of the droplet's shape [26], [27]. The total vertical adhesion force also decreases because of the lower wetting length (*Eq. 3.1*). Therefore, the droplet is more vulnerable to detaching from the surface in microgravity than in normal gravity. Note that this section was an example of microgravity's effect on droplet geometry, and similar trends were found for other coatings and droplet sizes.

3.3.3 Shedding behavior of droplet in microgravity

The experiments were conducted at an airflow between 3 m/s and 15 m/s at 80% RH and 0°C subcooling. Condensation was allowed to take place for 270–300 s before depositing a droplet. The droplet was deposited 3–5 s before the start of the microgravity phase in PF. Then, 3–5 s after experiencing microgravity, the airflow was increased to 15 m/s. Shedding behaviour for the 60 µL droplet on the PTFE coating is discussed as an example. The same procedure was performed for the ground experiment (timewise) to have similar tests. Each experiment was repeated four times. Displacement versus time for the microgravity and normal gravity tests are shown in *Figure 3.6-a* and *Figure 3.6-b*, respectively. For the inception of the movement, deviations (i.e., between the repeatability tests) of 0.1 s and 0.08 s were found for microgravity and normal gravity, respectively. After shedding started, a higher variation was found for both normal gravity and microgravity tests. A possible explanation is that the droplet coalesces with random condensating droplets and gets different sizes and movements in the way of shedding. This deviation was prominent for microgravity results because there was a slight acceleration in the direction of shedding.

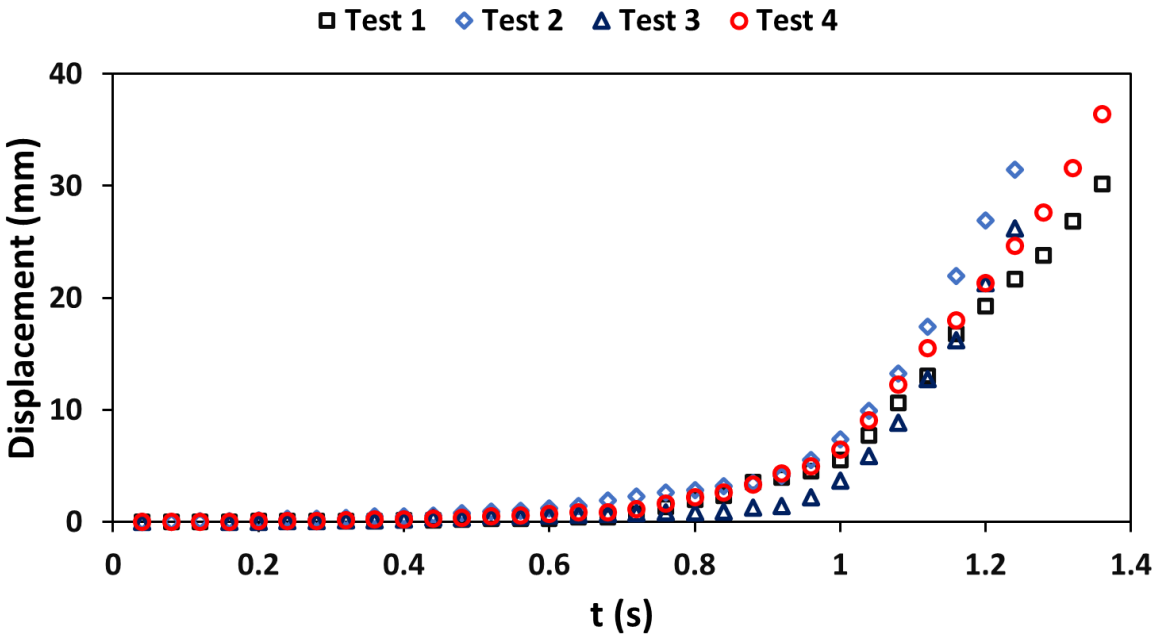

(a)

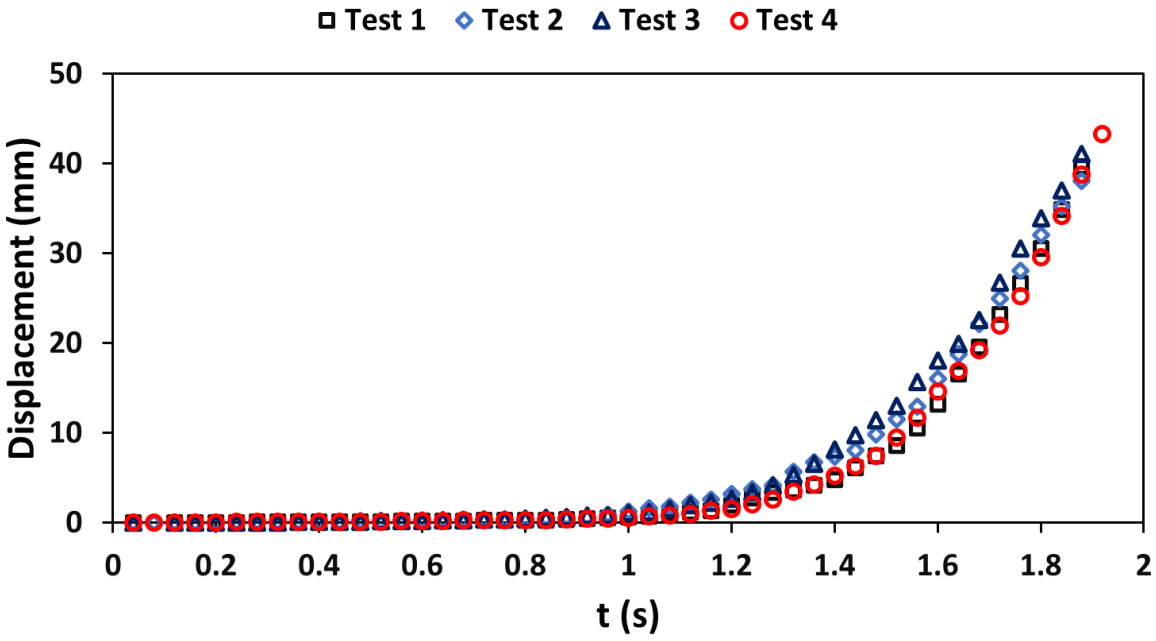

(b)

Figure 3.6. Displacement versus time for (a) microgravity and (b) normal gravity conditions. The coating is PTFE, and the droplet volume is 60μL

The same approach was used for airflow and droplet movement to achieve identical conditions and to compare microgravity and normal gravity results. The displacement graph and airflow velocity (i.e., the combined plot from all tests) are superimposed for the same time frame in *Figure 3.7*. In microgravity, the droplet shed at a 7% lower airflow compared with that of normal gravity. This confirms our analytical assertions earlier, that the droplet experiences a lower horizontal adhesion force and higher drag force in microgravity.

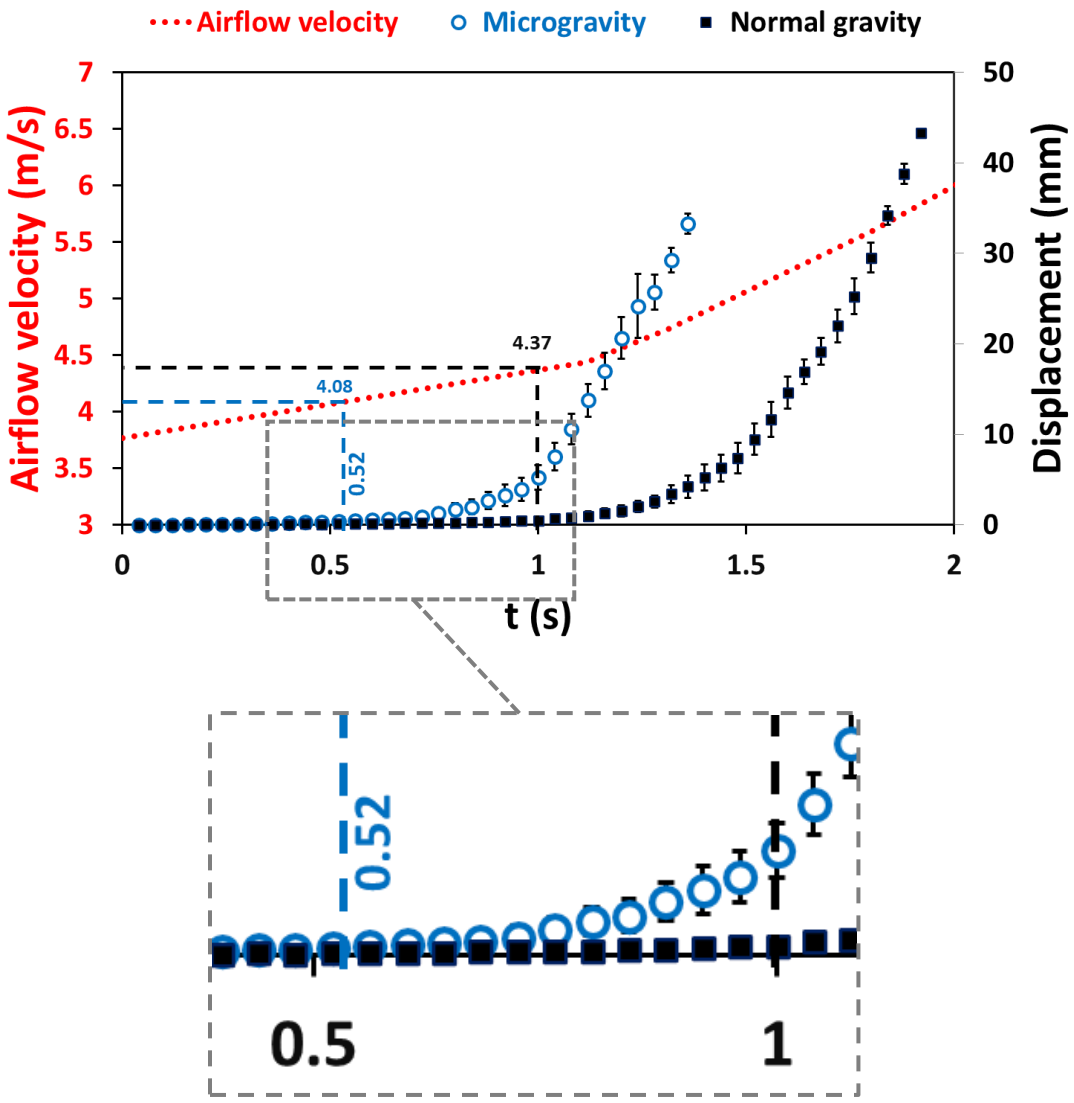

Figure 3.7. The displacement of droplet and airflow velocity are superimposed for the same time frame. The coating is PTFE, and the droplet volume is 60µL. The criterion for movement inception (shedding) of the centroid of the droplet was considered to be 10 pixels. Dotted line to guide the eyes.

The typical progression of 60 μL droplet deformation and shedding are shown in *Figure 3.8*. Each column represents a different coating. It can be seen in *Figure 3.8* that, for all droplets, the droplet (first row, stationary conditions) initially deforms as the gravity decreases (second row, microgravity condition). Then, air velocity increases until critical velocity and runback occurs (third row, shedding condition). However, in normal gravity, deformation due to gravity (second row) does not exist, explaining the higher critical velocity in *Figure 3.7*. The 40 μL and 80 μL droplets deformed into similarly trending shapes to those shown in *Figure 3.8*, depending on the coating.

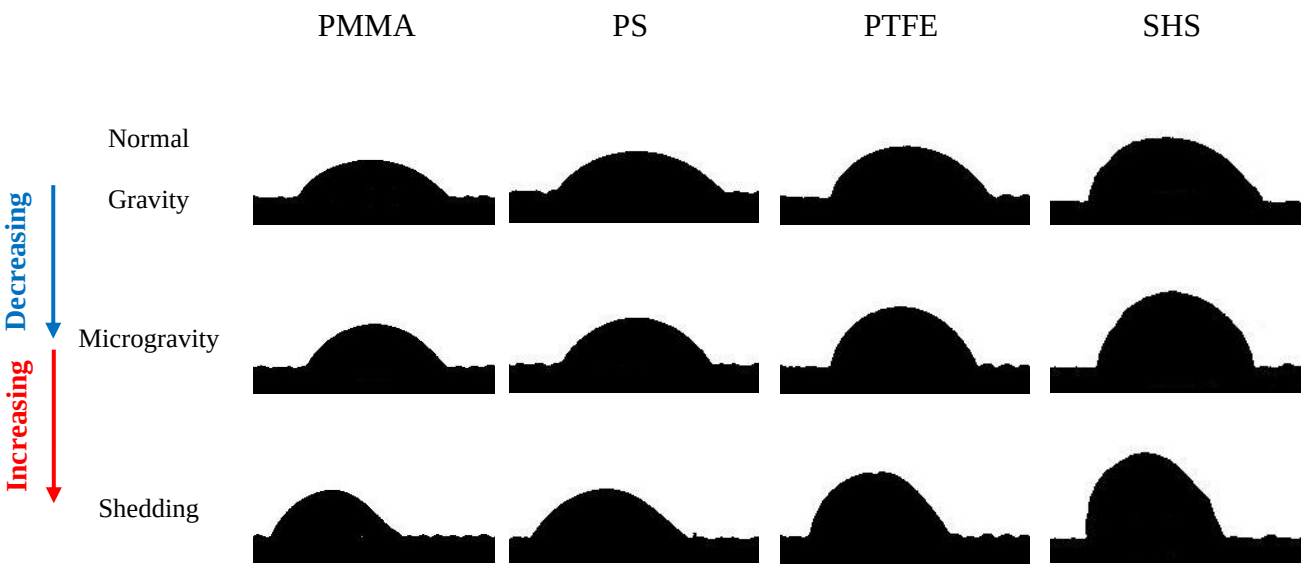

Figure 3.8. Typical progression of droplet deformation and shedding for different coatings. All droplets are 60 μL in volume. Initially, the axisymmetric droplet (first row, stationary conditions) deforms as the gravity decreases (second row, microgravity condition). Then, air velocity increases until critical velocity and runback commences (third row, shedding condition).

3.3.4 Effect of droplet size on shedding

Experiments were conducted for different droplet sizes of 40, 60, and 80 µL to investigate the effect of droplet size on shedding. The same procedure as in the previous section was used. *Figure 3.9* illustrates the results for both microgravity and normal gravity for different droplet sizes. The results clearly show that the shedding velocity is lower for microgravity, and it decreases according to the size of the droplet. Surfaces coated with PMMA, PS, and SHS also show the same trend, with different critical velocities depending on the coating and droplet size. Critical velocities for 0.5–100 µL droplets are taken from Milne et al. [21]. Although the contact angle and interaction of the droplet are different for the substrate in a condensation environment [15], the trend for critical velocities is in good agreement with [21]. In microgravity, a maximum critical velocity improvement (i.e., lower critical velocity) of 8% was found for droplet size of 40 µL.

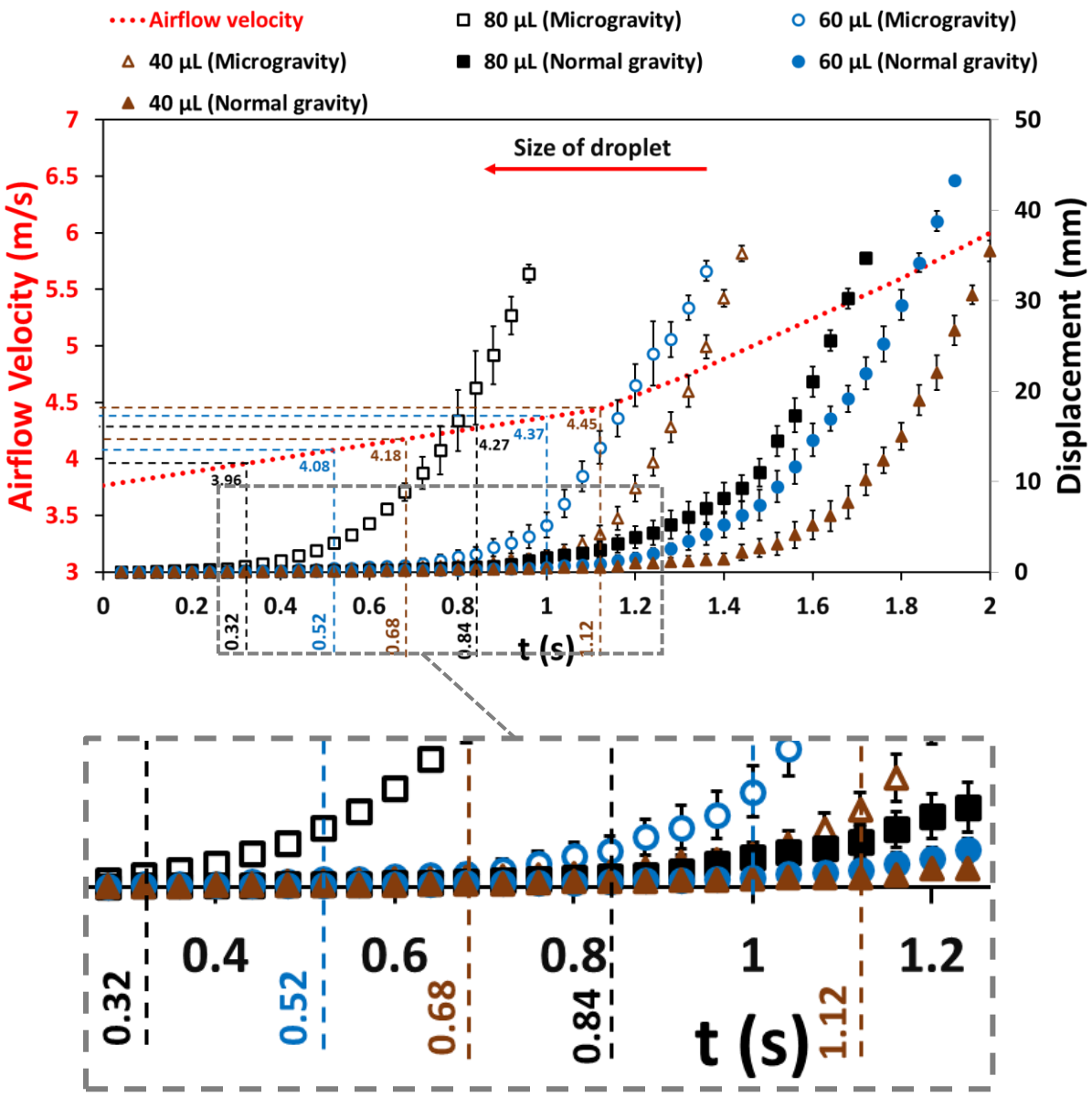

Figure 3.9. The displacement graph and airflow velocity are superimposed for the same time frame. Different droplet sizes of 40, 60, and 80 µL were tested at microgravity and normal gravity. Dotted line to guide the eyes. Colour plots online.

3.3.5 Effect of coating on shedding

The question of how the droplet adhesion force can be overcome by aerodynamic forces in order for shedding to occur can be answered by using different coatings; PMMA, PS, PTFE, and SHS used for the same droplet volume of 60 µL are discussed as an example (the same trend exists for 40 µL and 80 µL droplets). *Figure 3.10* shows the shedding velocities for various coatings. As hydrophobicity increases, the critical shedding velocity decreases. A possible explanation is that the droplet has lower adhesion forces when hydrophobicity increases. Also, the droplet develops a specific shape for higher hydrophobicity: i.e., higher height for the same volume. Therefore, the drag force increases when hydrophobicity increases. As a result of lower adhesion and higher drag, a droplet on PTFE coating experiences a lower shedding velocity. Similar behaviour can be seen in previous work on PMMA, Teflon, and SHS coatings [21].

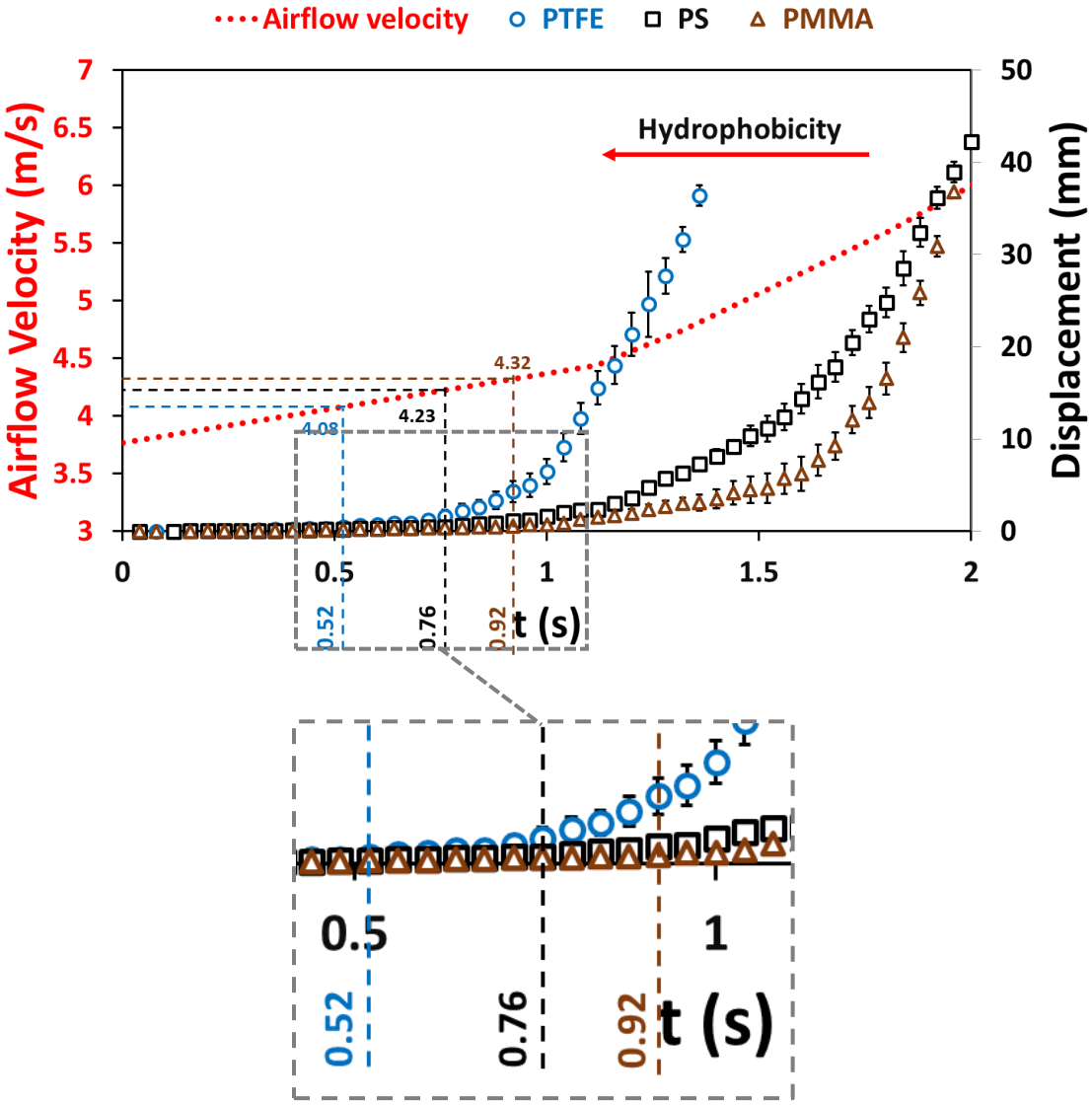

Figure 3.10. The displacement graph and airflow velocity are superimposed for the same time frame. The different substrate coatings of PMMA, PS, and PTFE were tested at microgravity conditions. Dotted line to guide the eyes.

3.3.6 Detachment of droplets

As seen in the previous section, increasing hydrophobicity is favourable for decreasing critical velocity. However, this raises a question: By how much can hydrophobicity be increased but still to avoid droplet detachment from a surface? To address this concern, we started by examining the most hydrophobic surface, i.e., SHS. It was tested under normal gravity and microgravity, and the results for a 40 µL droplet are discussed as an example. As shown in *Figure 3.11*, (a) and (b) (normal gravity before and after critical velocity, respectively), the shedding path is clear, and the droplet removes tiny droplets along its way as it travels on the surface. *Figure 3.11*, (c) and (d) shows top view of surfaces under microgravity conditions before and after critical velocity. In *Figure 3.11-d*, detachment of the droplet is apparent, as the path of cleaned tiny droplets comes to an abrupt end as the seeded droplet detaches from the surface (compare to *Figure 3.11-b*). As discussed earlier, from a condensation point of view, this is not favourable. Also, previous works showed that the shedding of condensate improves the heat transfer coefficient [25]; however, the shedding process and condensation cycle will not be efficient if condensate detaches. Droplet detachment was also found for 60 and 80 µL droplet sizes on an SHS in microgravity.

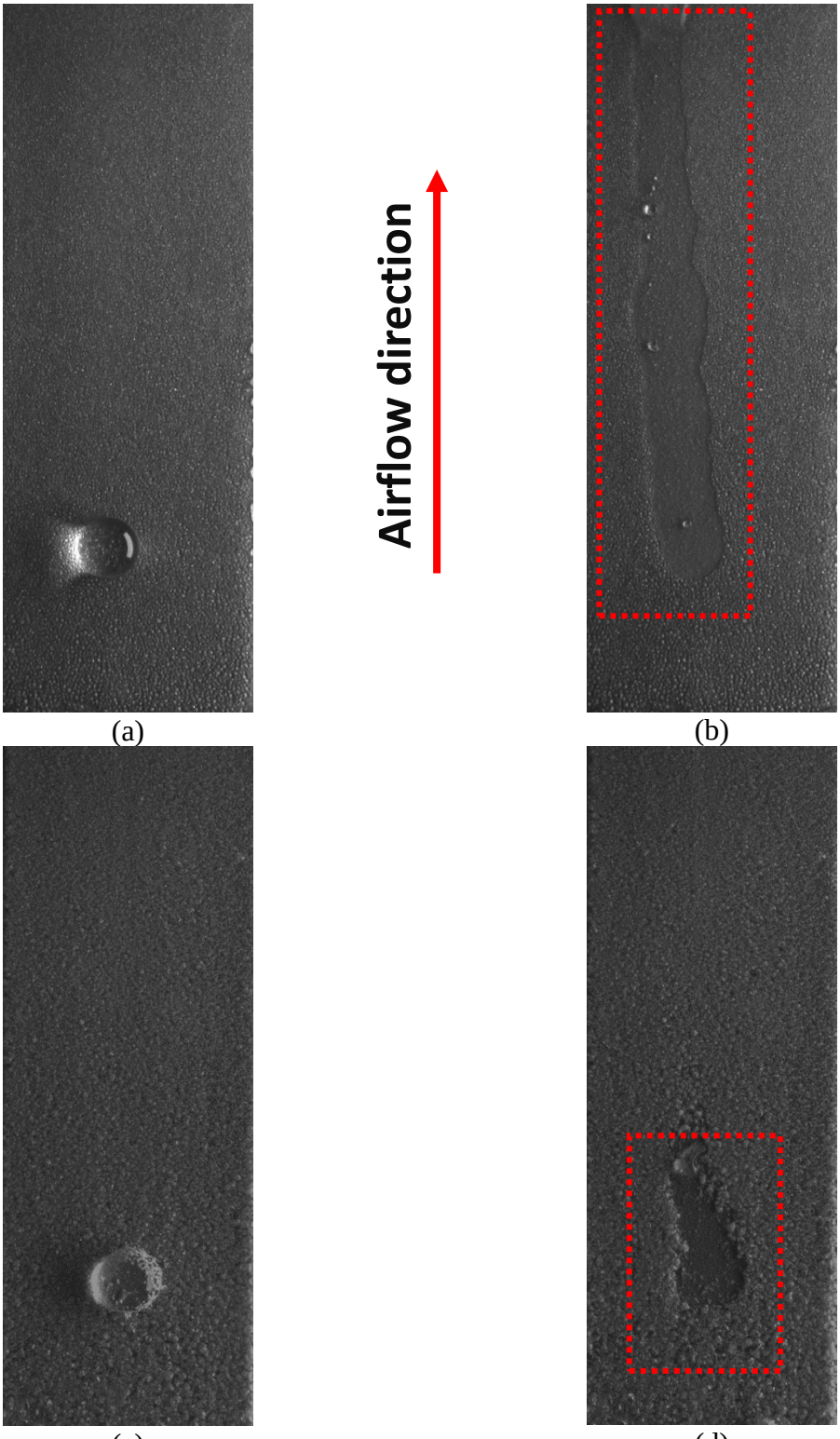

Figure 3.11. Top view for a 40µL droplet on the SHS substrate. (a) Normal gravity before critical velocity and (b) after critical velocity. (c) Microgravity before critical velocity, (d) Microgravity before critical velocity.

3.4 Conclusions

An experimental study was developed to characterize the shedding of condensation when exposed to airflow in a microgravity environment. Droplet shape analysis was conducted to develop an understanding of shedding behaviour. In microgravity, the same droplet has lower adhesion (wetting length) and undergoes higher drag force (frontal area). Both factors favour early shedding in microgravity. Therefore, the droplet in microgravity was shed in a maximum 8% lower airflow as compared with normal gravity. Then, the effect of droplet size was investigated for both microgravity and normal gravity. The results clearly show that the shedding velocity is lower for microgravity, and it decreases according to the size of the droplet. Also, increasing hydrophobicity decreases critical velocity. The droplet undergoes lower adhesion forces when hydrophobicity increases. As a result of lower adhesion and higher drag, a droplet on PTFE coating experiences a lower shedding velocity. Finally, the droplet was found to detach from superhydrophobic surfaces in microgravity. The detachment of droplets from the substrate will hamper the condensation process that can produce a larger fresh area; also, detachment of droplets and entrainment in airflow, regrates the concept of removing moisture from the air in a dehumidification process by condensation.

Acknowledgements

The project is partially supported by the European Space Agency (ESA) under the MAP program and the China Manned Space Agency (CMSA).

3.5 References

[1] E. J. Le Fevre and J. W. Rose, “An experimental study of heat transfer by dropwise condensation,” Int. J. Heat Mass Transf., vol. 8, no. 8, pp. 1117–1133, 1965.

[2] M. Ahlers, A. Buck-Emden, and H. J. Bart, “Is dropwise condensation feasible? A review on surface modifications for continuous dropwise condensation and a profitability analysis,” J. Adv. Res., vol. 16, pp. 1–13, 2019.

[3] J. M. Beér, “High efficiency electric power generation: The environmental role,” Progress in Energy and Combustion Science, vol. 33, no. 2. Pergamon, pp. 107–134, 2007.

[4] S. Parekh, M. M. Faridb, J. R. Selmana, and S. Al-Hallaj, “Solar desalination with a humidification-dehumidification technique-a comprehensive technical review,” Desalination, vol. 160, pp. 167–186, 2004.

[5] M.-H. Kim and C. W. Bullard, “Air-side performance of brazed aluminum heat exchangers under dehumidifying conditions,” Int. J. Refrig., vol. 25, no. 7, pp. 924–934, 2002.

[6] S. Oh and S. T. Revankar, “Experimental and theoretical investigation of film condensation with noncondensable gas,” Int. J. Heat Mass Transf., vol. 49, no. 15–16, pp. 2523–2534, 2006.

[7] X. H. Ma, X. D. Zhou, Z. Lan, Y. M. LI, and Y. Zhang, “Condensation heat transfer enhancement in the presence of non-condensable gas using the interfacial effect of dropwise condensation,” Int. J. Heat Mass Transf., vol. 51, no. 7–8, pp. 1728–1737, 2008.

[8] J. Huang, J. Zhang, and L. Wang, “Review of vapor condensation heat and mass transfer in the presence of non-condensable gas,” Applied Thermal Engineering, vol. 89. Elsevier Ltd, pp. 469–484, 2015.

[9] S. Khandekar and K. Muralidhar, Dropwise condensation on inclined textured surfaces, Chapter 4. NYC, USA: Springer, 2014.

[10] S. Daniel, M. K. Chaudhury, and J. C. Chen, “Fast drop movements resulting from the phase change on a gradient surface,” Science (80-.)., vol. 291, no. 5504, pp. 633–636, 2001.

[11] A. M. Macner, S. Daniel, and P. H. Steen, “Condensation on surface energy gradient shifts drop size distribution toward small drops,” Langmuir, vol. 30, no. 7, pp. 1788–1798, 2014.

[12] A. Razzaghi, S. A. Banitabaei, and A. Amirfazli, “Shedding of multiple sessile droplets by an airflow,” Phys. Fluids, vol. 30, no. 8, p. 087104, 2018.

[13] C. Antonini, F. J. Carmona, E. Pierce, M. Marengo, and A. Amirfazli, “General Methodology for Evaluating the Adhesion Force of Drops and Bubbles on Solid Surfaces,” Langmuir, vol. 25, no. 11, pp. 6143–6154, 2009.

[14] F. Barghi, M. Entezari, S. F. Chini, and A. Amirfazli, “Effect of initial wetting state on plastron recovery through heating,” Int. J. Heat Mass Transf., vol. 156, p. 119705, 2020.

[15] C. A. Papakonstantinou, H. Chen, V. Bertola, and A. Amirfazli, “Effect of condensation on surface contact angle,” Colloids Surfaces A Physicochem. Eng. Asp., vol. 632, p. 127739, 2022.

[16] S. Madani and A. Amirfazli, “Oil drop shedding from solid substrates by a shearing liquid,” Colloids Surfaces A Physicochem. Eng. Asp., vol. 441, pp. 796–806, 2014.

[17] S. Moghtadernejad, M. Tembely, M. Jadidi, N. Esmail, and A. Dolatabadi, “Shear driven droplet

shedding and coalescence on a superhydrophobic surface," Phys. Fluids, vol. 27, no. 3, p. 032106, 2015.

[18] F. Karmali and M. Shelhamer, "The dynamics of parabolic flight: Flight characteristics and passenger percepts," Acta Astronaut., vol. 63, no. 5–6, pp. 594–602, 2008.

[19] D. Brutin, Z. Zhu, O. Rahli, J. Xie, Q. Liu, and L. Tadrist, "Sessile drop in microgravity: Creation, contact angle and interface," Microgravity Sci. Technol., vol. 21, no. SUPPL. 1, pp. 67–76, 2009.

[20] A. Diana, M. Castillo, D. Brutin, and T. Steinberg, "Sessile drop wettability in normal and reduced gravity," Microgravity Sci. Technol., vol. 24, no. 3, pp. 195–202, 2012.

[21] A. J. B. Milne and A. Amirfazli, "Drop Shedding by Shear Flow for Hydrophilic to Superhydrophobic Surfaces†," Langmuir, vol. 25, no. 24, pp. 14155–14164, 2009.

[22] D. K. Mandal, A. Criscione, C. Tropea, and A. Amirfazli, "Shedding of Water Drops from a Surface under Icing Conditions," Langmuir, vol. 31, no. 34, pp. 9340–9347, 2015.

[23] I. V. Roisman, A. Criscione, C. Tropea, D. K. Mandal, and A. Amirfazli, "Dislodging a sessile drop by a high-Reynolds-number shear flow at subfreezing temperatures," Phys. Rev. E, vol. 92, no. 2, p. 023007, 2015.

[24] R. D. Mehta and P. Bradshaw, "Design rules for small low speed wind tunnels," Aeronaut. J., vol. 83, no. 827, pp. 443–453, 1979.

[25] M. Shakeri Bonab, R. Kempers, and A. Amirfazli, "Determining transient heat transfer coefficient for dropwise condensation in the presence of an air flow," Int. J. Heat Mass Transf., vol. 173, p. 121278, 2021.

[26] K. I. Sugioka and S. Komori, "Drag and lift forces acting on a spherical water droplet in homogeneous linear shear air flow," J. Fluid Mech., vol. 570, pp. 155–175, 2007.

[27] J. M. Kolinski, L. Mahadevan, and S. M. Rubinstein, "Lift-Off Instability During the Impact of a Drop on a Solid Surface," vol. 134501, no. April, pp. 1–5, 2014.

Chapter 4 Electrowetting Assisted Shedding of Droplets by a shearing airflow in Dropwise Condensation

4.1 Introduction

Condensation of water is an intrinsic part of a wide variety of industrial processes, including water harvesting systems [1], [2], dehumidification [3], distillation/desalination [4], and refrigeration and air conditioning [5]. There are two common types of condensation; filmwise condensation (FWC) and dropwise condensation (DWC). The condensate layer in FWC acts as a limiting factor for condensation rate and associated heat transfer. However, efficient condensate removal (shedding) in DWC increases the systems' efficiency by up to tenfold [6]. As a result, shedding of condensate from a solid surface is essential for maintaining DWC and consequent heat transfer improvement.

DWC has been extensively investigated, e.g., [7]–[9] to examine coatings that can improve condensation heat transfer. The cyclic process of DWC consists of four stages: nucleation, growth, coalescence, and shedding [10]. Shedding is seen when a droplet reaches a critical size and starts moving on the surface, removing tiny droplets on its way. Shedding occurs due to body force (e.g., gravity, magnetic, etc.), an external force (e.g., shear flow, electrowetting, etc.), and capillary force (e.g., surface chemical and/or roughness patterning). Shedding due to a shear flow is the focus of this work because the other methods are either unavailable or insufficient for some environments, such as space applications.

Hydrophobic and superhydrophobic surfaces (e.g., nanostructured, micro-grooved, wettability-patterned, and liquid impregnated textured) [11]–[15] facilitate condensate mobility and lower resistance to shedding, facilitating DWC mode [7]. However, all of the methods discussed above

alter the chemical or topographical patterning of the substrate passively to promote condensate mobility. Coatings are not necessarily long-lasting in harsh conditions [16], [17]. The contact angle is shown to decrease by condensation time for hydrophobic surfaces [18], which deteriorates the mobility of condensate.

An ideal substrate for DWC should offer ample spots for nucleation (to let initiation of condensation at the microscopic level) and swift condensate removal (to provide a fresh area for the new cycle of condensation). Hydrophilic surfaces provide a large number of nucleation sites with very weak drainage (condensation mode switches to FWC). Hydrophobic surfaces with a low contact angle hysteresis (CAH) aid in the removal of condensate; however, condensation may be hampered due to a lake of nucleation sites. The hybrid surfaces (patterned hydrophobic/hydrophilic surfaces) were proposed for gravity-driven shedding [19]. There are still some limitations for airflow shedding (i.e., in microgravity/absence of gravity or horizontal orientation). Gravity is body force and can be applied to condensate removal in both hydrophilic and hydrophobic regions and improve condensation rate and heat transfer performance. While airflow is an external force, and condensate has a small frontal area in the hydrophilic region. Therefore, hybrid surfaces are not a proper solution for the airflow shedding circumstances.

Apart from passive approaches, an alternating (AC) electric field has been used to promote condensation heat transfer by actively controlling droplets dynamic [20]–[24]. Several studies [19], [25]–[27] have been conducted on electrowetting (EW). Miljkovic et al. [13] developed a new electric-field-enhanced condensation mode by applying an external electric field. The results indicated that the bouncing of droplets due to coalescence in the absence of an electric field increases the average droplet size and deteriorates the condensation heat transfer performance. However, applying an electric field (100 and 200 V/cm) prevents the jumping of droplets and

results in a 50% increase in heat transfer coefficient. Kim et al. [28] used an electric field to manipulate the static three-phase contact line on the inclined surface. They characterized three regimes (gravity dominated, intermediate, and surface force dominated) and demonstrated that the critical inclination angle (i.e., for the onset of droplet motion) decreased significantly by applying an electric field.

EW can be used to manipulate the fluid-solid interaction, enabling microfluidic operations (e.g., movement, splitting, and merging of droplets). EW is a wettability modification technique (applying an electrical potential difference) for a surface (patterned electrodes across a dielectric layer) to actuate the droplet. The classic Young-Lippman's equation [25], [29] can be used to describe the voltage-dependent contact angle:

$$cos\theta = cos\theta_{nv} + \frac{C}{2\sigma}V^2 \tag{4.1}$$

where θ_{nv} denotes the contact angle in the absence of voltage; C, σ, V are the capacitance per unit area of the dielectric layer, the surface tension, and the applied voltage, respectively.

Baratian et al. [30] experimentally investigated the effect of EW on humid airflow (flow rate of 2 l/min) condensation with the temperature of 36 ±1 °C and substrate temperature of 25 °C. They demonstrated that the electrostatic energy landscape created by AC-EW drives condensate droplet movement and coalescence, resulting in the formation of distinct breath figures. As opposed to traditional breath figures, where the coalescing drops remain constrained to the centre of mass of the parent drops, in this case, the coalescing drops align at the respective electrostatic energy minima. In addition, their results showed that altering the breath figure parameters under EW (150 v with the frequency of 1 kHz) results in increased heat transfer efficiency. Recently, Wikramanayake et al. [24] experimentally studied the effect of electric fields (voltage 60 and 100

V, and frequencies of 1 and 10 kHz) on coalescence and growth dynamics during humid air condensation with RH of 60 ± 2.5% and subcooling of 2 ± 1 °C. The results showed that AC fields with higher frequencies provide stronger coalescence than DC fields resulting in a higher growth rate. The electric fields also affected the shedding dynamics, and condensate roll-off improved heat transfer up to 31%.

Previous studies have shown that the rate of condensation in the leading edge of the horizontal substrate is high, so larger droplets form there [31]. The shedding initiates with those large droplets at the leading edge, and the tiny droplets all removed in the wake of the large droplets. Considering this, and the fact that EW has been shown to coarsen and arrange the condensate droplets, one may use EW locally to manipulate the arrangement of droplets to initiate early shedding.

Razzaghi et al. [32] examined the shedding behaviour of various sessile droplets patterns when placed in close proximity to one another. The results indicated that when the droplets are close together (as is typically the case for condensation), the critical velocity of shedding for a square arrangement is lower than for a diamond arrangement. Therefore, manipulating the droplets arrangement by EW can decrease the critical velocity for the shedding of condensate and improve heat transfer performance. This is in addition to the effect of EW, shown to coarsen the droplets that is also useful for shedding them at lower critical velocity [33].

There exist some works on the utilizing of EW for condensation enhancement [34], [24]. To our knowledge, all the existing works have not considered the effect of EW on the shedding of condensate by airflow. Therefore, the objective of the current study is to investigate the enhancement of heat transfer and droplet shedding during humid air condensation using EW-based surfaces airflow on the horizontal surface.

4.2 Methods and materials

A mini closed-looped wind tunnel was used to simulate the condensation environment and control condensation parameters such as airflow velocity, relative humidity (RH), and condensing substrate temperature (see *Figure 4.1*). Condensation experiments were carried out on a silicon substrate. The upstream segment of the substrate had interdigitated electrodes (see *Figure 4.2*). AC electric field was applied to investigate the effect of EW on heat transfer performance. Condensation tests were conducted on identical substrates and under similar experimental conditions with no voltage (control) and under an electric field. Heat transfer measurement was done using a meter bar (i.e., using transient inverse heat conduction developed earlier [31]) and was synchronized to two-phase flow visualization. A high-resolution camera was used to monitor the condensation in both cases. The experimental procedure, fabrication, and measurement methods are briefly described below.

4.2.1 Experimental setup and heat flux meter bar

The primary part of the experimental setup, a mini closed-looped wind tunnel, was capable of controlling RH (10 – 80% ± 4%), airflow velocity (0 – 20 ± 0.2 m/s), and substrate temperature (0 – 40 ± 0.1 °C). *Figure 4.1* shows a schematic drawing of the wind tunnel with associated humidity and velocity control systems. A PID humidity device (HD100, Auber) was used to regulate and quantify the RH. An axial fan (4118N/2H6P, Ebmpapst), an adjustable power supply, and a hot-film anemometer (EE75, E+E Elektronik Ges.m.b.H) were utilized to generate and measure airflow. The substrate temperature was controlled using a Peltier cell (CP-031, TE technology). The substrate was located horizontally inside the test section of 150 mm long and 50×50 mm cross-sections. The airflow inside the test section was characterized as discussed in [31].

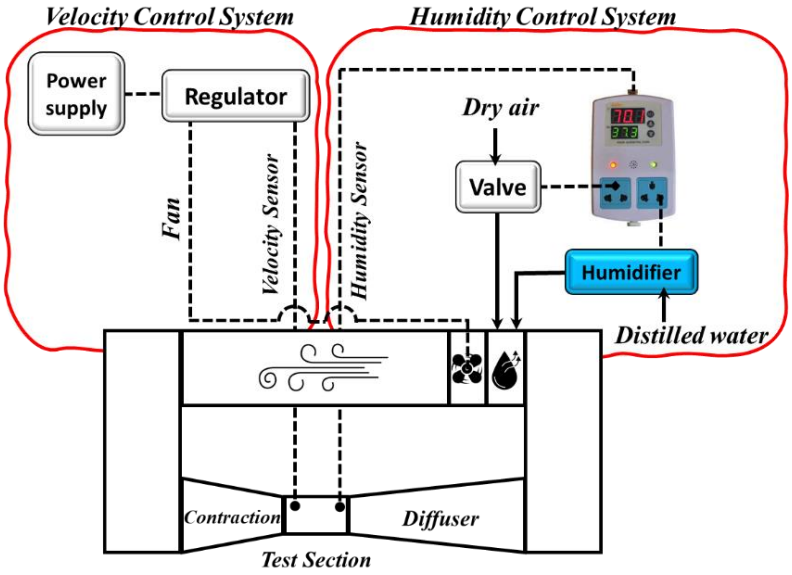

Figure 4.1. Schematic diagram of the wind tunnel with associated velocity and humidity control systems

The heat flux and heat transfer coefficient were characterized using a meter bar (Al alloy 6061-T6, Metal Supermarket) and resistance temperature detectors (RTDs) with a diameter of 1 mm (PT100KN1510 ±0.01 °C, Omega). Extruded polystyrene (RSI-0.88, Owens Corning) was applied to insulate the meter bar. *Figure 4.3* shows the sensors pattern and meter bar in detail. The RTDs were calibrated using a thermal bath and standard RTD (50 mm-long Fluke PRT full immersion reference probe, Model 5606) calibrated by the Alpha Controls and Instrumentation (accredited to ISO/IEC 17025 by the A2LA) [35]. Maximum uncertainty of ± 0.016 K was found for the temperature difference of RTDs.

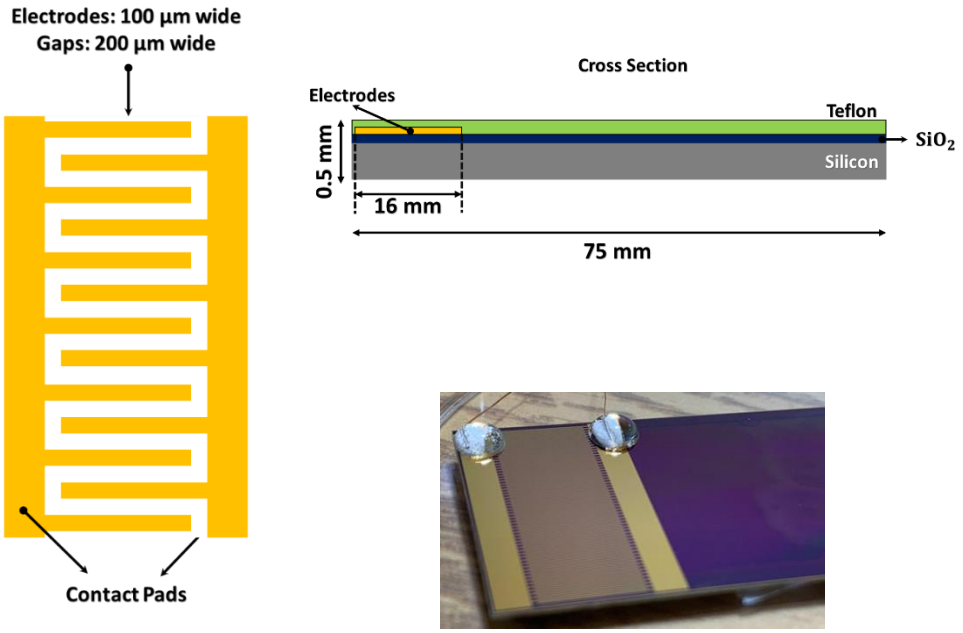

Figure 4.2. The schematic and actual substrate, showing the arrangement of interdigitated electrodes.

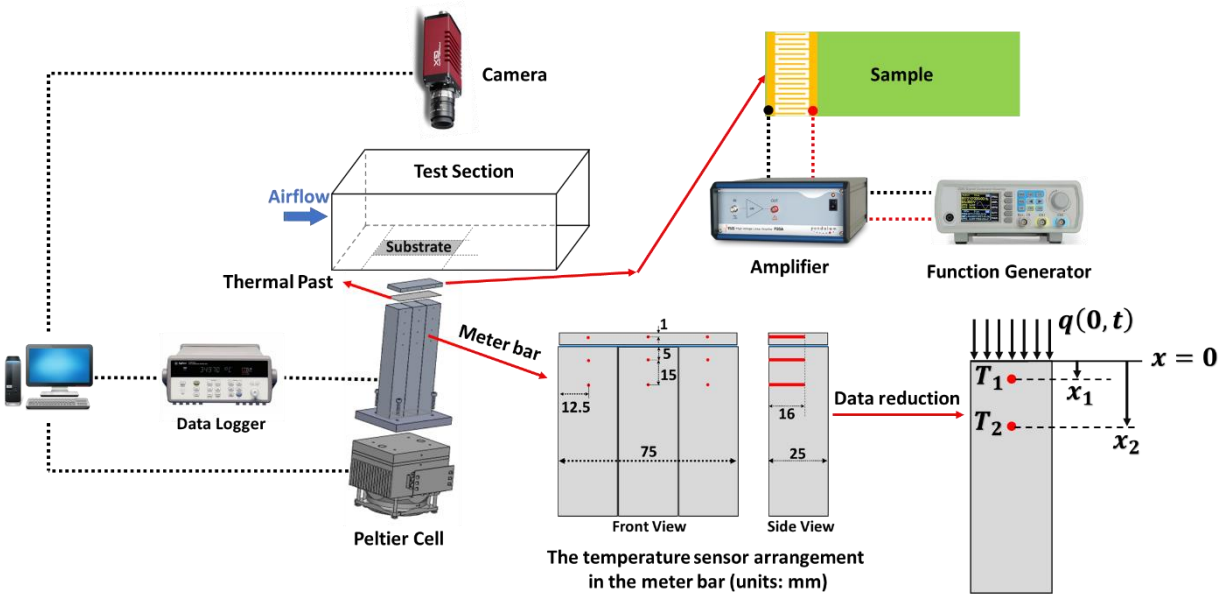

Figure 4.3. The schematic view of measurement systems including meter bar, camera and AC voltage generator. The camera and temperature sensors are synchronized.

An overhead camera (Prosilica GX 1660, 1600 × 1200 pixel Allied Vision) and 50 mm/F2.8 camera lens (NMV-50M23, Navitar) were used to capture the morphology of droplets. The images were taken with an average image size of 10 × 7.5 mm and an average resolution of 148 pixels/mm. Captured images were synchronized to the experimental data collected by DAQ (34970A, Keysight) every 5 seconds to correlate HTC and the condensation morphology.

4.2.2 EW substrate

Condensation experiments were carried out on a silicon plate (p-type, d 525 µm), with a 300 nm thermal oxide on top. A set of electrodes were made of chromium, and gold were patterned on top of the substrate (see *Figure 4.2*). The electrodes had a width of 100 µm and a pitch of 200 µm, as shown in *Figure 4.2*. The entire substrate was then coated with a dielectric polymer (Teflon AF1600) film (spun coated to a 1 µm thickness) that is hydrophobic (*Figure 4.2*). The dielectric layer stores electrostatic energy that acts as an actuator for the droplet. The substrate was flush-mounted horizontally on the test section floor over the meter bar for heat transfer measurement (*Figure 4.3*).

Electrodes were connected to a high voltage and ground ends of a signal generator and amplifier, to create an electric field between neighbouring electrodes (*Figure 4.4*). An AC voltage with a maximum amplitude of 150 V, at 1 and 10 kHz frequencies was applied. Baseline experiments were carried out without any voltage. To prevent the breakdown of the dielectric layer, no more than 150 V was used for the experiments. As the DC field does not provide oscillatory motion of the contact line, larger droplets are less likely to capture nearby smaller ones [24]; therefore, a DC field was not used in this work.

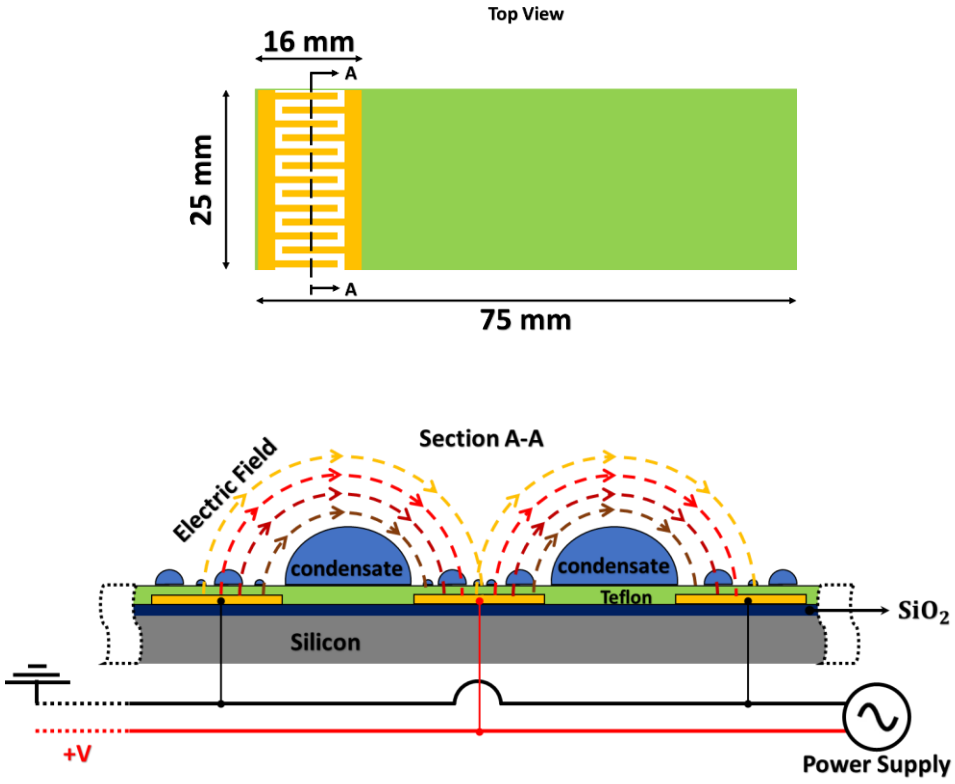

Figure 4.4. Schematic diagram of the substrate cross-section (A-A plane), showing electric field lines and aligned droplets in the gaps of electrodes.

4.2.3 Data reduction and inverse heat conduction method

Data reduction was accomplished using the transient inverse heat conduction method. Boundary conditions (e.g., heat flux and HTC) can be estimated by measuring the temperatures (T_1 and T_2) at minimum two positions (x_1 and x_2) of meter bar (see *Figure 4.3*). Note that the meter bar was designed to represent a continuous one-dimensional body with constant thermal properties. Temperature distribution inside the meter bar is assumed to be continuous and smoothly varying. The objective of the approach is to measure the transient temperature distribution and heat flux at the top surface ($x = 0$) using the temperature data at $x_1 and\ x_2$.

The polynomial for temperature distribution in the meter bar is a function of x, and time-dependent coefficients:

$$T_n(x,t) = \sum_{i=1}^{n} c_i(t)x^{i-1} \tag{4.2}$$

This polynomial must agree with the temperatures at the two measurement points and satisfy the physics of the problem, i.e., the one-dimensional heat conduction equation (*Eq. 4.3*):

$$\frac{\partial^2 T}{\partial x^2} = \frac{1}{\alpha}\frac{\partial T}{\partial x} \tag{4.3}$$

The term for the $c_i(t)$ in *Eq. 4.2* can be determined using temperatures and their even-numbered spatial derivatives as:

$$\begin{bmatrix} T(x_1,\,t) \\ T(x_2,\,t) \\ \frac{\partial^2 T(x_1,\,t)}{\partial x^2} \\ \frac{\partial^2 T(x_2,\,t)}{\partial x^2} \end{bmatrix} = \begin{bmatrix} 1 & x_1 & {x_1}^2 & {x_1}^3 \\ 1 & x_2 & {x_2}^2 & {x_2}^3 \\ 0 & 0 & 2 & 6x_1 \\ 0 & 0 & 2 & 6x_2 \end{bmatrix} \begin{bmatrix} c_1(t) \\ c_2(t) \\ c_3(t) \\ c_4(t) \end{bmatrix} \tag{4.4}$$

Then $c_i(t)$ can be calculated by inverting the matrix in *Eq. 4.4*:

$$c_i(t) = a_{ij}b_i(t) \tag{4.5}$$

where:

$$a_{ij} = \begin{bmatrix} \frac{x_2}{x_2-x_1} & \frac{-x_1}{x_2-x_1} & \frac{x_1x_2(2x_2-x_1)}{6(x_2-x_1)} & \frac{x_1x_2(x_2-2x_1)}{6(x_2-x_1)} \\ \frac{-1}{x_2-x_1} & \frac{1}{x_2-x_1} & \frac{{x_1}^2-2x_1x_2-2{x_2}^2}{6(x_2-x_1)} & \frac{2{x_1}^2+2x_1x_2-{x_2}^2}{6(x_2-x_1)} \\ 0 & 0 & \frac{x_2}{2(x_2-x_1)} & \frac{-x_1}{2(x_2-x_1)} \\ 0 & 0 & \frac{1}{6(x_2-x_1)} & \frac{1}{6(x_2-x_1)} \end{bmatrix} \quad \text{(sensor positions)} \tag{4.6}$$

$$b_i(t) = \begin{bmatrix} T(x_1,\ t) \\ T(x_2,\ t) \\ \frac{\partial^2 T(x_1,\ t)}{\partial x^2} \\ \frac{\partial^2 T(x_2,\ t)}{\partial x^2} \end{bmatrix} \quad \text{(temperature readings and the heat equation)} \tag{4.7}$$

More information about the abovementioned procedure can be found in [31]. The temperature profile in the meter bar can be reconstructed using $c_i(t)$. Then, temperature, heat flux and HTC at x = 0 can be calculated as follows:

$$T(0,\ t) \approx T_3(0,\ t) = c_1(t) \tag{4.8}$$

$$q(0,\ t) \approx -k\frac{\partial T_3(0,\ t)}{\partial x} = -kc_2(t) \tag{4.9}$$

$$h_{global} = \frac{q}{(T_\infty - T_s)} \tag{4.10}$$

where k and T_∞ are the meter bar thermal conductivity and airflow temperature, respectively. As a close approximation, the condensation contribution in HTC was considered as in *Eq. 4.9*. It is understood that this method is not necessarily equal to latent heat since airflow improves the mixing of the inert gas layer and favours temperature gradients within the boundary layer [36].

$$h_{condensation} = h_{global} - h_{convection} \tag{4.11}$$

Uncertainty analysis was done using Monte Carlo approach as described in [35]. The maximum uncertainties of the temperature readings ($\pm 0.01\ ^\circ C$) and positions ($\pm 0.01\ mm$) were considered, and 2000 points in the range of uncertainty were chosen randomly. Then, the uncertainty of HF and HTC was calculated for each measurement using the propagation procedure [37].

4.3 Results and discussion

For the experiments, humidified air at the velocities of 1, 5, 10, and 15 m/s and ambient temperature of 25 ± 2 °C was passed through the test section; RH was 60%, and the substrate was held at a temperature of 0°C. Note that a humidity level of 60% was chosen to conduct the tests because this would provide a higher rate of condensation and yet would not create fog on the walls of the test section. The experiments were categorized into two types: low and high airflow velocities. Droplets will not shed at low airflow velocity tests, unlike the high airflow velocity experiments. The effect of EW on the size and distribution of condensate is investigated for low velocities. Then, condensate size and distribution are linked to the shedding process for high velocities.

4.3.1 Early-stage droplet growth in the low airflow velocity

Firstly, experiments were conducted at lower velocities to visualize early-stage droplet growth dynamics. This provides an understanding of EW behaviour for condensate size and distribution before diving into the shedding process. *Figure 4.5* illustrates a typical progression of the condensate distribution at 270 s, 900 s, 1800 s, and 2700 s for the control case (i.e., absence of an electric field), 1 kHz case, and 10 kHz case with airflow of 1m/s, RH of 60%, and substrate temperature of 0°C. As the average condensate size grows in the control case, the droplets follow a self-similar and homogeneous random pattern (as seen in *Figure 4.5-a to d*). However, the electric field affects the droplet distribution. For example, in *Figure 4.5-e,* droplets were located along with the gaps (dark areas between electrodes) where the electrostatic energy of the system is minimized [25], [26], [34]. Note that the droplet size should be sufficiently large (radius > 5–10 μm) to allow the electrostatic force to overcome the resistance owing to CAH [34].

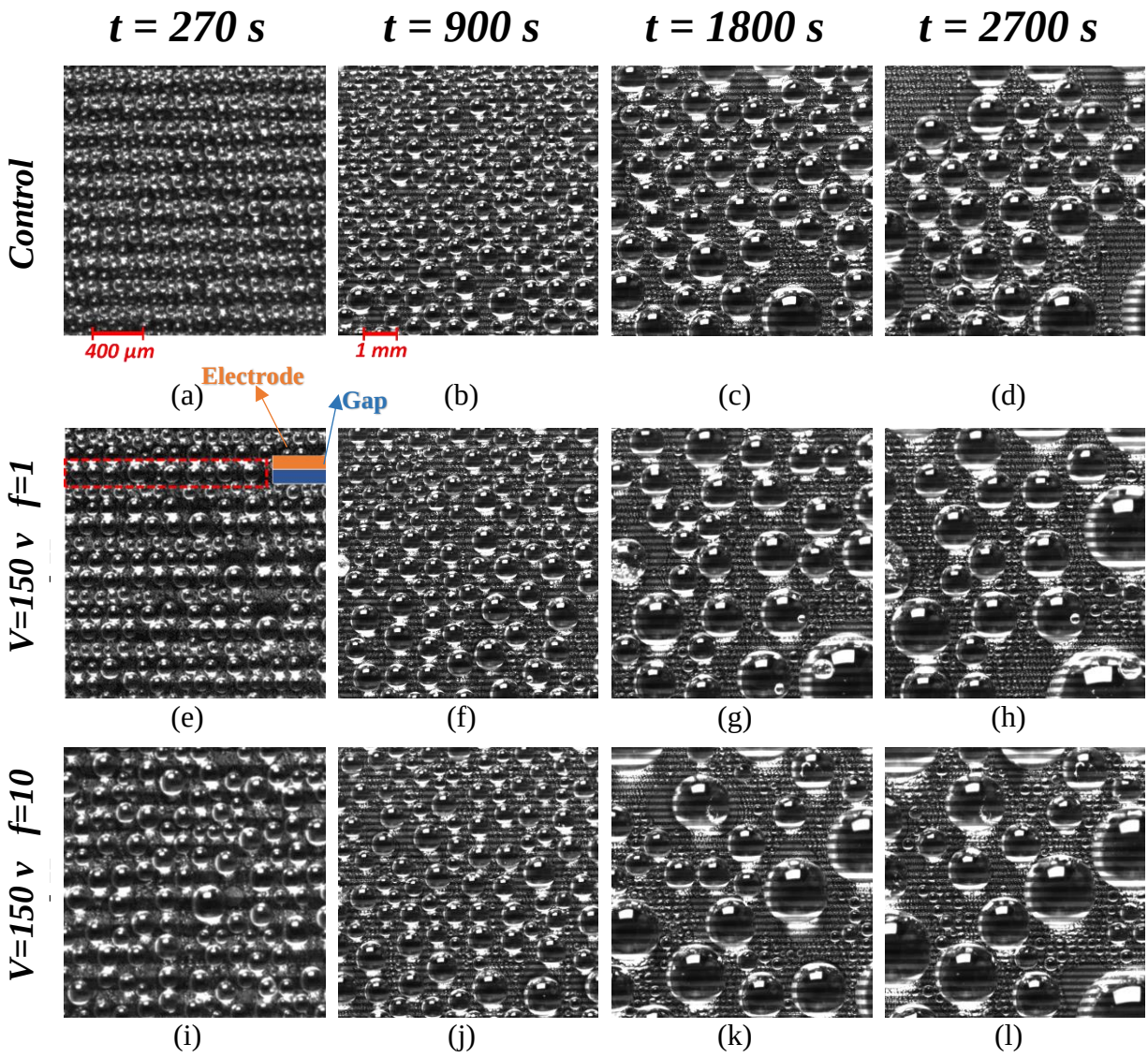

Figure 4.5. Typical progression of the condensate distribution for control (no voltage), f=1 kHz, and f=10 kHz. As shown in a, the scale for the column of t=270 s is 400 µm. The scale is 1 mm for the rest, as shown in b. The airflow, RH, and substrate temperature are 1 m/s, 60%, and 0°C, respectively.

As seen in *Figure 4.5-e*, droplets coalesced as they grew, but they still aligned with the gaps between electrodes. The droplets are larger in the identical situation for 10 kHz compared to 1 kHz [24], [38]. The physical translation of droplets around their equilibrium positions in reaction to the electric field is one possible explanation to see larger droplets (in addition to oscillations at the triple-phase line). Both forms of motion (oscillation and translation) promote coalescence resulting

in larger droplets. Also, contact-line oscillations decrease droplet pinning as electric fields reduce CAH [34], [39].

To characterize the overall contribution of the electric field on growth dynamics, condensate morphology was quantified. The area-weighted average droplet radius, $\langle R \rangle = \frac{\sum r^3}{\sum r^2}$ was calculated using image processing in MATLAB (*Figure 4.6*).

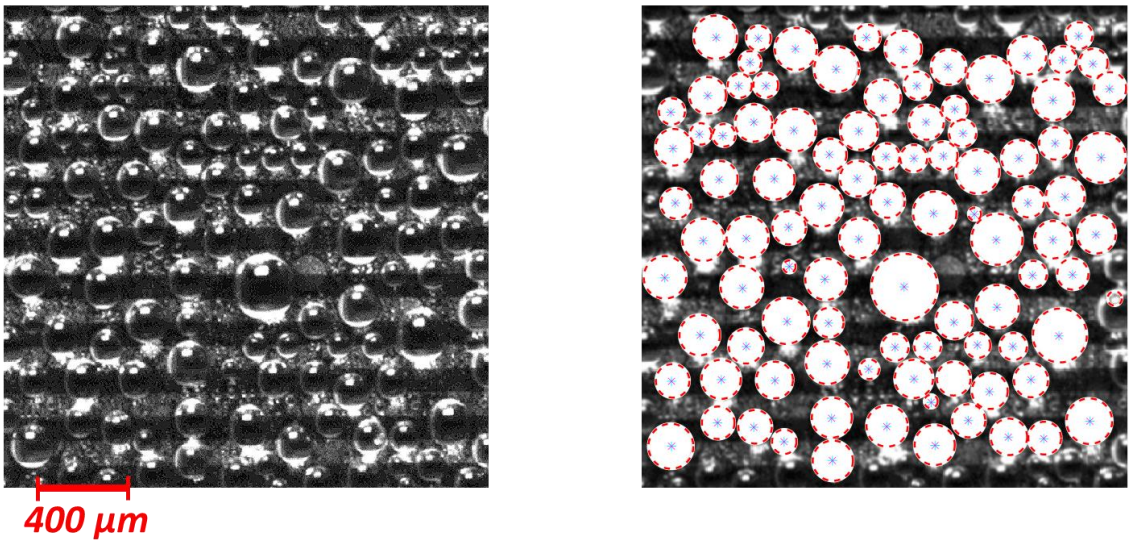

Figure 4.6. Condensate detection using image processing to calculate area-weighted average droplet radius. Condensate distribution for f=10 kHz case at t=270 s shown as an example. The airflow, RH, and substrate temperature are 1 m/s, 60%, and 0°C, respectively.

Figure 4.7 illustrates the progression of $\langle R \rangle$ for an applied voltage of 150 V with frequencies of 1 Hz, and 10 kHz, along with the control case for 1 m/s. Note that 1 m/s is lower than the critical airflow for shedding, and the purpose is to investigate the condensate morphology under the effect of the electric field. *Figure 4.7* clearly shows that the electric field increases $\langle R \rangle$, especially for longer periods.

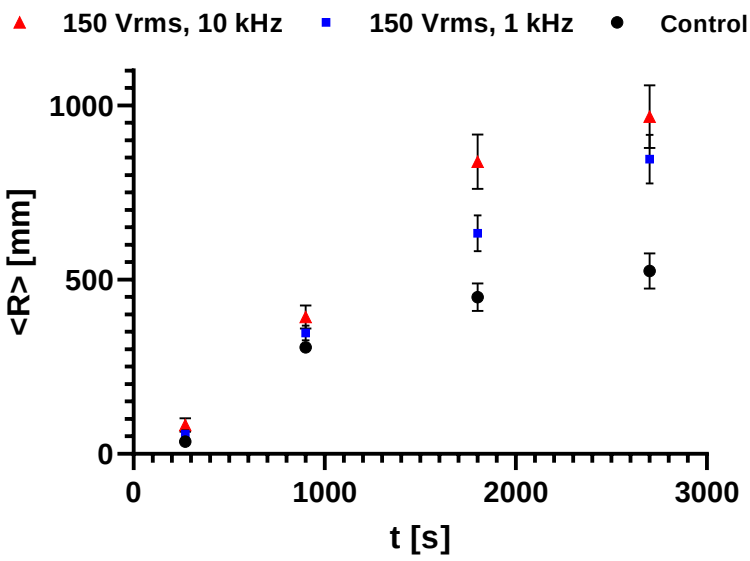

Figure 4.7. The area-weighted average radius of condensed droplets versus time for control, f=1 kHz, and f=10 kHz. The airflow, RH, and subcooling are 1 m/s, 60%, and 0°C, respectively.

After 45 minutes, $\langle R \rangle$ was increased by 61% and 84% for 1 kHz and 10 kHz, respectively, compared to the control case. A higher condensate growth rate for 10 kHz compared to 1 Hz shows that high frequencies facilitate the movement and coalescence of droplets due to the associated reduction of CAH [26], [34].

4.3.2 Effect of electric field on condensate shedding

The applied electric field and frequencies influence condensate dynamics, as seen in the previous section. Experiments were conducted at higher airflows (5 m/s and more) to characterize shedding and associated condensate dynamics. Shedding was determined with the first significant movement of the condensate (i.e., displacement of more than 1000 pixels). Condensate shedding happens when the airflow is sufficiently strong (5 m/s and higher), and the radius of the droplets reach a critical value [40]. Shedding time (t_s) is the time it takes for shedding to start. *Figure 4.8* shows the condensate distribution before and after shedding with the associated shedding time for

airflow of 10 m/s. Experiments were conducted in the identical situation for control, 1 kHz and 10 kHz cases. As seen in *Figure 4.8*, shedding time is lower when the electric field is applied and becomes significant for 10 kHz. Larger condensate in the case of 10 kHz resulted in quicker shedding and a higher frequency of condensation cycle.

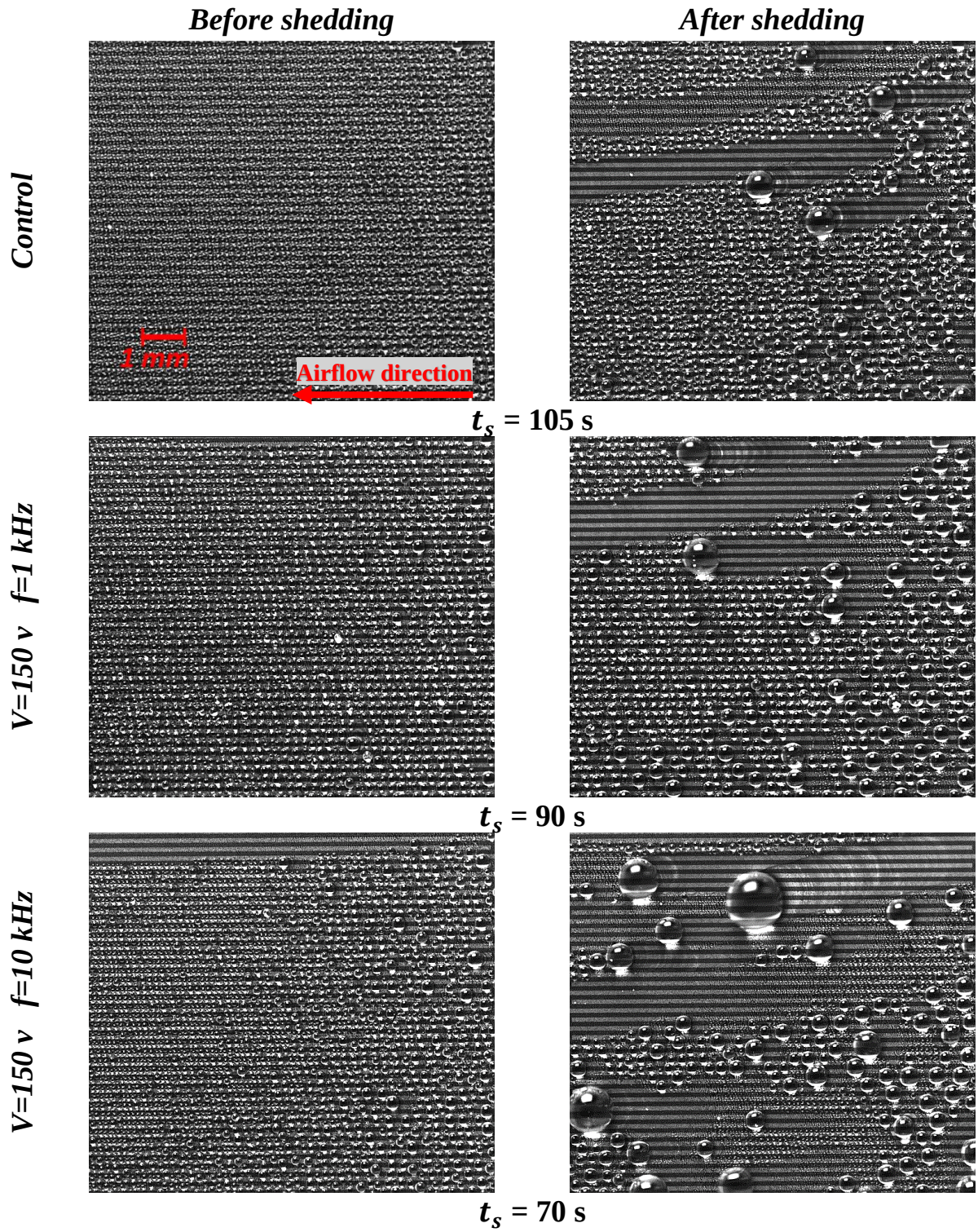

Figure 4.8. Condensate distribution before and after shedding with the associated shedding time for control, 1 kHz, and 10 kHz cases. The airflow, RH, and subcooling are 10 m/s, 60%, and 0°C, respectively.

Maximum droplet diameter was measured to quantify the condensate dynamics. *Figure 4.9* shows the maximum droplet diameter versus time for the airflow of 10 m/s. The points above droplet critical size (dashed line) represent the droplet moving on the surface and getting larger, until it moves out of the imaging area. For the control case, 1 kHz, and 10 kHz, the shedding time are 105 s, 90 s, and 70 s, respectively. Similar trends were found for 5 m/s and 15 m/s.

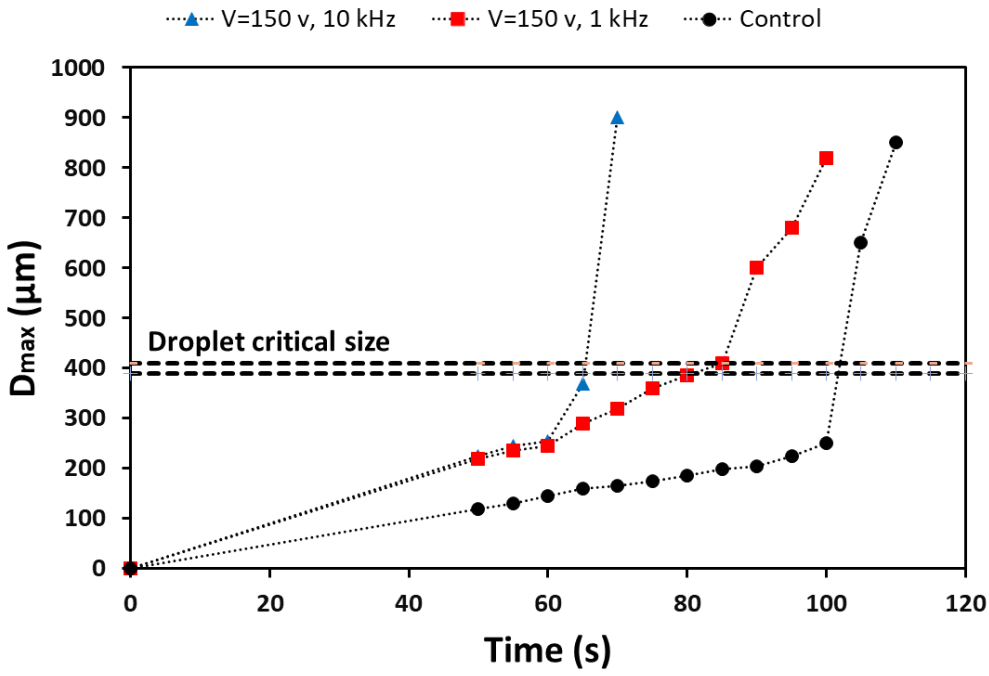

Figure 4.9. Maximum droplet diameter versus time for three cases (control, f=1 kHz, and f=10 kHz). The airflow, RH, and subcooling are 10 m/s, 60%, and 0°C, respectively. Droplet critical size was determined with the first significant movement of the condensate (i.e., displacement of more than 1000 pix). The points after droplet critical size represent the droplet while moving and getting larger, until it goes out of the area of interest.

To better understand the effect electric field, the shedding time was normalized with respect to the control case for each airflow velocity (i.e., the control case was considered as a reference for each airflow velocity). *Figure 4.10* shows the normalized shedding time, $t_s/(t_s)_{Control}$, for the different airflow velocities. It can be clearly seen that the 10 kHz case provides lower shedding time, which became significant with the increase of airflow (i.e., at 15 m/s, the difference is more

significant). The reason is the larger size of the droplets when 10 kHz was applied. Lower shedding time causes a higher frequency of condensation, which improves heat transfer performance [41].

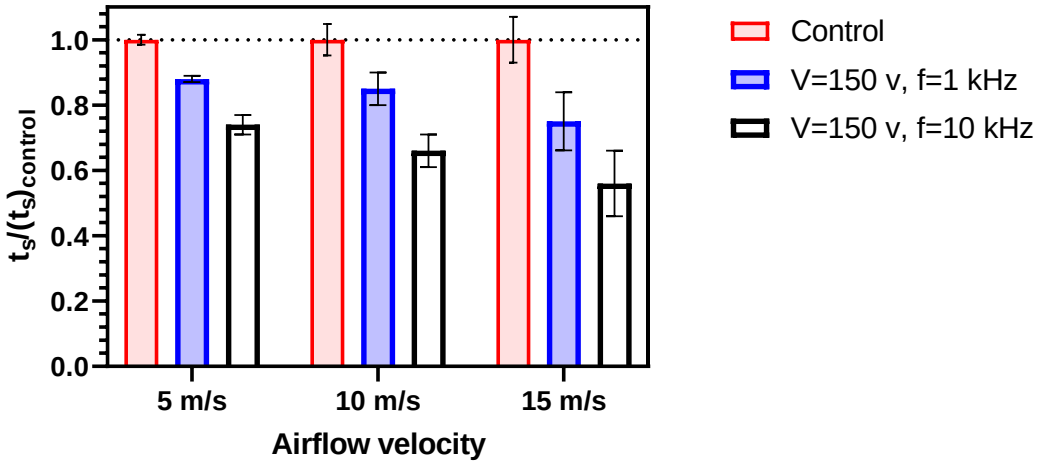

Figure 4.10. Normalized shedding time versus airflow velocity for three cases (control, f=1 kHz, and f=10 kHz). The control case was considered as a reference for each airflow velocity.

4.3.3 Effect of electric fields on HTC

The experiments were conducted for different airflow velocities of 1, 5, 10, and 15 m/s with control, 1 kHz, and 10 kHz electric field. The HTC was calculated using the meter bar, and the transient heat conduction method explained earlier. The meter bar had three different sections to measure heat flux locally: leading area, middle and trailing areas. *Figure 4.11* shows the overall HTC (average of the locations) for three cases (control, f=1 kHz, and f=10 kHz) with different airflow velocities. For the airflow velocity of 1 m/s, a similar HTC was found for all three cases, as shedding was not seen. Although the 10 kHz case results in larger droplets, a significant fraction of the substrate was also covered. Therefore, unlike the vertical surface where the shedding happens by gravity, the effect of coalescence may be cancelled by a higher coverage rate. Also, the electrodes are located at the leading edge (22 % of the substrate), and other sides of the substrate would be unaffected when there is no shedding.

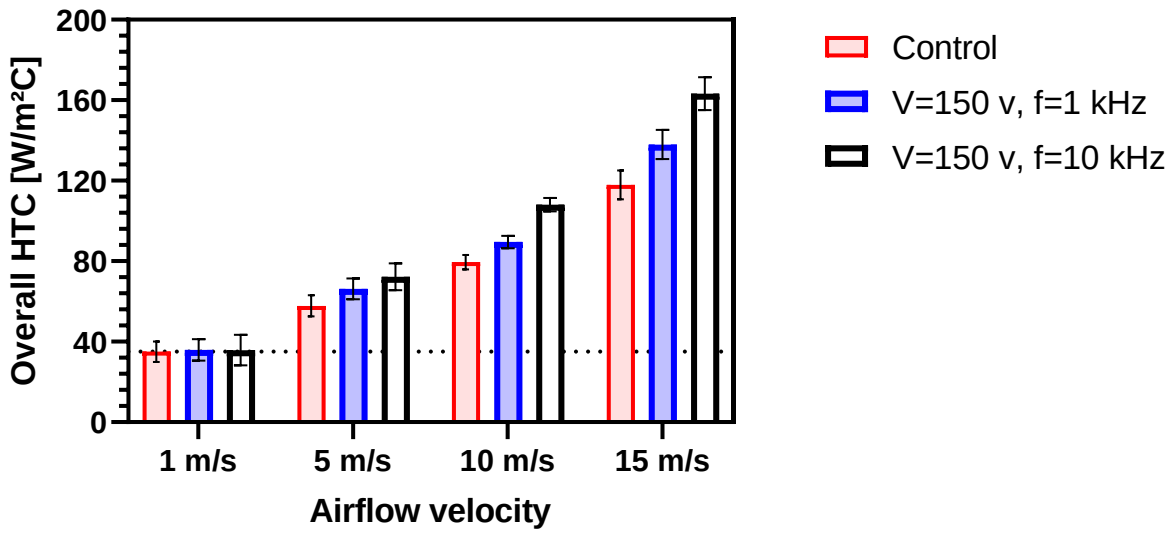

Figure 4.11. Overall heat transfer coefficient (HTC) versus airflow for three cases (control, f=1 kHz, and f=10 kHz).

The condensate size distribution is crucial for shedding and overall HTC, especially in the starting area where the shedding starts [31]. When larger droplets shed, they sweep away tiny condensate along the way, exposing new surfaces for nucleation. Moreover, larger droplets seen under the electric field resulted in an increase in the frequencies of the condensation cycle. As such, higher HTC was found for 10 kHz and for airflows of 10 and 15 m/s where the shedding was prominent, and HTC increased by 36% and 38.5% compared to the control case, respectively.

4.4 Conclusion

Previous studies have focused on the effect of EW on the dynamic behaviour of droplets. However, all the existing works have not considered the effect of EW on the shedding of condensate by a humid airflow. The purpose of the current study was to investigate the effect of EW-based surfaces on droplet shedding and heat transfer enhancement during humid air condensation. AC electric field with the frequencies of 1 and 10 kHz was applied and compared with the baseline (control case). HTC was determined using a transient inverse heat conduction method which was synchronized to a high-resolution camera to monitor the condensation dynamics. The results show that, after 45 mins, ⟨R⟩ was increased by 61% and 84% for 1 kHz and 10 kHz, respectively, compared to the control case for 1 m/s airflow. Electric field with high frequencies reduces CAH and facilitate the movement and coalescence of droplets. It can be clearly seen that the 10 kHz case results in shorter shedding time, which became significant with the increase of airflow. Lower shedding time causes a higher frequency for condensation, which enhances heat transfer performance. In addition, higher HTC was found for 10 kHz and for airflow of 15 m/s where the shedding was prominent, and HTC increased by 38.5% compared to the control case. This foundation provides insight into the EW's utilization on condensate shedding under shear flow.

Acknowledgement

The authors acknowledge Prof. Frieder Mugele and Daniel Wijnperle for providing the EW condensation substrates.

4.5 Reference

[1] R. V Wahlgren, “Atmospheric water vapour processor designs for potable water production: a review,” Water Res., vol. 35, no. 1, pp. 1–22, 2001.

[2] D. Milani, A. Abbas, A. Vassallo, M. Chiesa, and D. Al Bakri, “Evaluation of using thermoelectric coolers in a dehumidification system to generate freshwater from ambient air,” Chem. Eng. Sci. J., vol. 66, pp. 2491–2501, 2011.

[3] R. L. Webb and K. Hong, “Performance of Dehumidifying Heat Exchangers With and Without Wetting Coatings,” in Transaction of the ASME, 1999, p. vol. 125, 1018-1026.

[4] S. Parekh, M. M. Faridb, J. R. Selmana, and S. Al-Hallaj, “Solar desalination with a humidification-dehumidification technique-a comprehensive technical review,” Desalination, vol. 160, pp. 167–186, 2004.

[5] M.-H. Kim and C. W. Bullard, “Air-side performance of brazed aluminum heat exchangers under dehumidifying conditions,” Int. J. Refrig., vol. 25, no. 7, pp. 924–934, 2002.

[6] M. Rama, N. Reddy, M. Yohan, and K. H. Reddy, “Heat Transfer Co-Efficient Through Dropwise Condensation and Filmwise Condensation Apparatus,” Int. J. Sci. Res. Publ., vol. 2, no. 12, 2012.

[7] J. W. Rose, “Dropwise condensation theory and experiment: A review,” Proc. Inst. Mech. Eng. Part A J. Power Energy, vol. 216, no. 2, pp. 115–128, 2002.

[8] A. Alizadeh, V. Bahadur, A. Kulkarni, M. Yamada, and J. A. Ruud, “Hydrophobic surfaces for control and enhancement of water phase transitions,” MRS Bull., vol. 38, no. 5, pp. 407–411, May 2013.

[9] N. Miljkovic, R. Enright, and E. N. Wang, “Effect of droplet morphology on growth dynamics and heat transfer during condensation on superhydrophobic nanostructured surfaces,” ACS Nano, vol. 6, no. 2, pp. 1776–1785, Feb. 2012.

[10] P. Meakin, “Steady state behavior in a model for droplet growth, sliding and coalescence: the final stage of dropwise condensation,” Phys. A Stat. Mech. its Appl., vol. 183, no. 4, pp. 422–438, May 1992.

[11] N. Miljkovic et al., “Jumping-droplet-enhanced condensation on scalable superhydrophobic nanostructured surfaces,” Nano Lett., vol. 13, no. 1, pp. 179–187, Jan. 2013.

[12] R. D. Narhe and D. A. Beysens, “Nucleation and growth on a superhydrophobic grooved surface,” Phys. Rev. Lett., vol. 93, no. 7, p. 076103, Aug. 2004.

[13] N. Miljkovic, D. J. Preston, R. Enright, and E. N. Wang, “Electric-field-enhanced condensation on superhydrophobic nanostructured surfaces,” ACS Nano, vol. 7, no. 12, pp. 11043–11054, Dec. 2013.

[14] A. Ghosh, S. Beaini, B. J. Zhang, R. Ganguly, and C. M. Megaridis, “Enhancing dropwise condensation through bioinspired wettability patterning,” Langmuir, vol. 30, no. 43, pp. 13103–13115, 2014.

[15] J. B. Boreyko and C. H. Chen, “Self-propelled dropwise condensate on superhydrophobic surfaces,” Phys. Rev. Lett., vol. 103, no. 18, p. 184501, Oct. 2009.

[16] C. Lee, H. Kim, and Y. Nam, “Drop Impact Dynamics on Oil-Infused Nanostructured Surfaces,” Langmuir, vol. 30, no. 28, pp. 8400–8407, Jul. 2014.

[17] J. S. Wexler, I. Jacobi, and H. A. Stone, “Shear-driven failure of liquid-infused surfaces,” Phys. Rev. Lett., vol. 114, no. 16, p. 168301, Apr. 2015.

[18] C. A. Papakonstantinou, H. Chen, V. Bertola, and A. Amirfazli, “Effect of condensation on surface contact angle,” Colloids Surfaces A Physicochem. Eng. Asp., vol. 632, p. 127739, 2022.

[19] A. Ghosh, S. Beaini, B. J. Zhang, R. Ganguly, and C. M. Megaridis, “Enhancing dropwise condensation through bioinspired wettability patterning,” Langmuir, vol. 30, no. 43, pp. 13103–13115, Nov. 2014.

[20] P. Birbarah, Z. Li, A. Pauls, and N. Miljkovic, “A Comprehensive Model of Electric-Field-Enhanced Jumping-Droplet Condensation on Superhydrophobic Surfaces,” Langmuir, vol. 31, no. 28, pp. 7885–7896, Jul. 2015.

[21] X. Yan, J. Li, L. Li, Z. Huang, F. Wang, and Y. Wei, “Droplet condensation on superhydrophobic surfaces with enhanced dewetting under a tangential AC electric field,” Appl. Phys. Lett., vol. 109, no. 16, p. 161601, Oct. 2016.

[22] T. Foulkes, J. Oh, P. Birbarah, J. Neely, N. Miljkovic, and R. C. N. Pilawa-Podgurski, “Active hot spot cooling of GaN transistors with electric field enhanced jumping droplet condensation,” Conf. Proc. - IEEE Appl. Power Electron. Conf. Expo. - APEC, pp. 912–918, May 2017.

[23] A. Shahriari, P. Birbarah, J. Oh, N. Miljkovic, and V. Bahadur, “Electric Field–Based Control and Enhancement of Boiling and Condensation,” https://doi.org/10.1080/15567265.2016.1253630, vol. 21, no. 2, pp. 102–121, Apr. 2016.

[24] E. D. Wikramanayake and V. Bahadur, “Electrowetting-based enhancement of droplet growth dynamics and heat transfer during humid air condensation,” Int. J. Heat Mass Transf., vol. 140, pp. 260–268, Sep. 2019.

[25] F. Mugele and J. C. Baret, “Electrowetting: From basics to applications,” J. Phys. Condens. Matter, vol. 17, no. 28, Jul. 2005.

[26] V. Bahadur and S. V. Garimella, “An energy-based model for electrowetting-induced droplet actuation,” J. Micromechanics Microengineering, vol. 16, no. 8, p. 1494, Jun. 2006.

[27] N. Kumari, V. Bahadur, and S. V. Garimella, “Electrical actuation of electrically conducting and insulating droplets using ac and dc voltages,” J. Micromechanics Microengineering, vol. 18, no. 10, p. 105015, Sep. 2008.

[28] J. Kim and M. Kaviany, “Purging of dropwise condensate by electrowetting,” J. Appl. Phys., vol. 101, no. 10, 2007.

[29] L. Chen and E. Bonaccurso, “Electrowetting — From statics to dynamics,” Adv. Colloid Interface Sci., vol. 210, pp. 2–12, Aug. 2014.

[30] D. Baratian, R. Dey, H. Hoek, D. Van Den Ende, and F. Mugele, “Breath Figures under Electrowetting: Electrically Controlled Evolution of Drop Condensation Patterns,” Phys. Rev. Lett., vol. 120, no. 21, pp. 1–5, 2018.

[31] M. Shakeri Bonab, R. Kempers, and A. Amirfazli, “Determining transient heat transfer coefficient for dropwise condensation in the presence of an air flow,” Int. J. Heat Mass Transf., vol. 173, p. 121278, 2021.

[32] A. Razzaghi, S. A. Banitabaei, and A. Amirfazli, “Shedding of multiple sessile droplets by an airflow,” Phys. Fluids, vol. 30, no. 8, p. 087104, 2018.

[33] A. J. B. Milne and A. Amirfazli, “Drop Shedding by Shear Flow for Hydrophilic to Superhydrophobic Surfaces,” Langmuir, vol. 25, no. 24, pp. 14155–14164, 2009.

[34] D. Baratian, R. Dey, H. Hoek, D. Van Den Ende, and F. Mugele, “Breath Figures under Electrowetting: Electrically Controlled Evolution of Drop Condensation Patterns,” Phys. Rev. Lett., vol. 120, no. 21, May 2018.

[35] R. Kempers, P. Kolodner, A. Lyons, and A. J. Robinson, “A high-precision apparatus for the characterization of thermal interface materials,” Rev. Sci. Instrum., vol. 80, no. 9, p. 095111, Sep. 2009.

[36] S. Danilo, C. Dominique, and P. Frédéric, “Experimental dropwise condensation of unsaturated humid air – Influence of humidity level on latent and convective heat transfer for fully developed turbulent flow,” Int. J. Heat Mass Transf., vol. 102, pp. 846–855, 2016.

[37] S. J. Kline and F. A. McClintock, “Describing uncertainties in single-sample experiments,” Mech. Eng., vol. 75, no. 1, pp. 3–8, 1953.

[38] E. D. Wikramanayake, J. Perry, and V. Bahadur, “AC electrowetting promoted droplet shedding on hydrophobic surfaces,” Appl. Phys. Lett., vol. 116, no. 19, 2020.

[39] R. Dey, J. Gilbers, D. Baratian, H. Hoek, D. Van Den Ende, and F. Mugele, “Controlling shedding characteristics of condensate drops using electrowetting,” Appl. Phys. Lett., vol. 113, no. 24, p. 243703, Dec. 2018.

[40] D. K. Mandal, A. Criscione, C. Tropea, and A. Amirfazli, “Shedding of Water Drops from a Surface under Icing Conditions,” Langmuir, vol. 31, no. 34, pp. 9340–9347, 2015.

[41] A. Alshehri, J. P. Rothstein, and H. P. Kavehpour, “Improving heat and mass transfer rates through continuous drop-wise condensation,” Sci. Reports 2021 111, vol. 11, no. 1, pp. 1–15, Oct. 2021.

Chapter 5 Conclusions and Suggestions for Future Work

5.1 Summary and conclusions

This work investigated dropwise condensation of water in humid air when subjected to air shear flow under various environmental conditions. This research was primarily experimental and consisted of two distinct mini closed-loop wind tunnels. The first setup was designed to investigate the influence of various airflows on the condensation heat transfer coefficient of humid air on a horizontal surface. Transient and instantaneous heat flux measurements were required to study the relationship between condensate morphology and HTC. To facilitate this, a transient inverse heat conduction method was used to characterize the time-varying surface heat flux and associated HTC. The results clearly show that the condensate shedding process resulted in a low average droplet size and doubled heat transfer performance improvement. Also, it was found that the rate of condensation from the leading edge of the horizontal substrate was high, leading to a larger average droplet size. The shedding initiated with large droplets at the leading edge, and the large droplets removal resulted in the removal of smaller droplets in their way. Therefore, it is possible to use EW locally to manipulate the arrangement of droplets that control shedding (i.e., at the leading edge or any location with critical droplet size for shedding). Therefore, this setup was also used to investigate the effect of EW-based surfaces on droplet shedding and heat transfer enhancement during humid air condensation. An AC electric field with different frequencies was applied and compared with the control case (no voltage).

A second setup was developed to investigate the shedding kinematics of water droplets in a condensation environment when exposed to aerodynamic forces in microgravity. A robust experimental setup was designed and manufactured for the parabolic campaign. This campaign

was part of the November 2020 European Space Agency (ESA) 73rd PF campaign framework and was used to simulate a microgravity environment. A wide range of contact angles (60˚–160˚) were tested to find balance between the vertical and horizontal adhesion forces. The experiments determined the coating which was observed to provide the minimal required air velocity for the shedding of the droplets without causing the droplet to lift off the surface. This knowledge can inform the design of condensers that work under microgravity conditions and dropwise condensation mode. The findings of this work can be summarized as follows:

- The transient inverse heat conduction method was used to characterize the surface HF and associated HTC. It took approximately 5 s for the system to respond: i.e., a 5-fold decrease in time for the steady-state method. Also, it took approximately 30 s (~6-fold decrease) for the system to detect an HTC change within 95%. Thus, using the transient inverse conduction method, time-varying HTC can be measured reasonably accurately to within 30 s.
- The effect of RH on condensation was investigated, and higher HTC was found for higher RHs. Also, it was found that the effect of RH is significant in the DWC regime compared with the FWC regime. When coverage ratio and droplet size increase (finally reach FWC), HTC decreases significantly more for higher RHs than for lower RHs.
- HTC for the subcooling of T = 0°C is smaller than for 5 and 10 °C. Subcooling changes the circularity of the forming condensate and the coverage ratio. A twig-shaped droplet was found for subcooling of 0°C; however, it was more circular for higher subcooling.
- HTC for condensation contribution increased with increasing air velocity. However, for the velocities at which shedding was not seen, the rate of increase in intensity decreased. In the case of shedding, the slope of the HTC increment increased by increasing airflow velocity.

The results clearly show that condensate shedding enables maintenance of a low average droplet size and, consequently, doubles HTC.

- Droplet shape analysis was conducted to develop an understanding of shedding behaviour. In microgravity, the same droplet has lower adhesion (wetting length) and undergoes higher drag force (frontal area). Both factors favor early shedding in microgravity. Therefore, the droplet in microgravity was shed in an airflow 7% lower than normal gravity.
- The effect of droplet size was investigated for both microgravity and normal gravity. The results clearly show that the shedding velocity is lower for microgravity, and it decreases according to the size of the droplet.
- Increasing hydrophobicity decreases critical velocity. This is because the droplet undergoes lower adhesion forces when hydrophobicity increases. Also, the droplet develops a specific shape for higher hydrophobicity: i.e., a higher height for the same volume. Therefore, the drag force increases when hydrophobicity increases. As a result of lower adhesion and higher drag, a droplet on PTFE coating experiences a lower shedding velocity.
- For superhydrophobic surfaces in microgravity, the droplet was found to detach.
- An AC electric field with the frequencies of 1 and 10 kHz was applied and compared with the control case (no voltage). The results show that, after 45 mins for 1 m/s airflow, the area-weighted average radius was increased by 61% and 84% for 1 kHz and 10 kHz, respectively, compared with the control case. High frequencies facilitate the movement and coalescence of droplets due to the associated reduction of CAH.
- The 10 kHz case results in shorter shedding time, which became significant by increasing of airflow. Furthermore, lower shedding time causes a higher frequency for condensation, which enhances heat transfer performance.

- HTC was found to be higher at 10 kHz in the presence of shedding, and the difference became significant when an airflow of 15 m/s was applied: shedding was prominent, and HTC increased by 35% compared to the control case.

5.2 Scope for research and future work

The present work provides a fundamental basis for future condensation experiments with the aim of designing surfaces to optimize heat transfer performance and provides a basis for understanding the effects of different coatings and electrowetting. A list of potential future research work and enhancements to this study are as follows:

- *Using Particle Image Velocimetry (PIV) to better understand the shedding behaviour of DWC under shear flow*

  In current study, airflow velocity was measured by a hot-film anemometer providing free stream velocity. However, the velocity near the droplet might be different from the free stream velocity. PIV is likely the most promising and accurate technique for characterizing the flow field over condensate. It is a non-intrusive measurement method that can provide a whole flow field inside the test section and over the condensate. Critical velocity for the shedding of condensate can be measured accurately using PIV.

- *Using infrared temperature sensors to measure substrate temperature for HTC characterization*

  In current work, resistance temperature detectors (RTD) were used to measure the substrate temperature. Although RTDs provide reasonable accuracy, they should be embedded inside the substrate as close as possible to the condensing surface. This method can be intrusive and affects measurements. Also, heat conduction interpolation was used to

determine the temperature of the condensing surface because direct measurement is not possible using RTDs. However, an infrared temperature sensor is a non-intrusive method that could provide better accuracy; these sensors could be used to characterize HTC more accurately.

- *Investigation of different arrangements and shapes for interdigitated electrodes of EW-based substrate to promote condensate shedding under shear flow*

  In the current study, condensation experiments were carried out on a single EW-based substrate: a silicon plate coated with a dielectric polymer film that is hydrophobic. This work provides insight into EW's utilization of condensate shedding under shear flow. However, it is known that different interdigitated electrodes can affect condensate shedding and heat transfer performance. Therefore, different interdigitated electrode shapes and arrangements could be trialed in order to optimize droplet shedding under shear flow.

Appendices

Appendix A: Flow quality evaluation

For evaluating the flow quality inside the test section, the velocity profile at different locations was measured using the hot wire anemometer (TSI, T1.5 boundary layer probe). The origin of the coordinates was considered in the middle of the upstream edge of the test surface as seen in **Error! Reference source not found.**3. Three different positions in the Y direction (-12, 0 and 12 mm) were considered at the upstream and downstream edge of the surface (X = 0 and 75 mm). In the Z direction, 10 points were considered i.e.,1, 2, 3, 4, 5, 10, 15, 20, 25, and 30 mm above the surface. Because of the boundary layer near the surface, more points were chosen near the surface. Measurements were done at 1, 5, 10, and 15 m/s. Characteristic velocity profiles in the different positions of width at the downstream edge for the velocity of 15 m/s are shown in *Figure A.1*. The results show the uniformity of the airflow by 94% inside the test section.

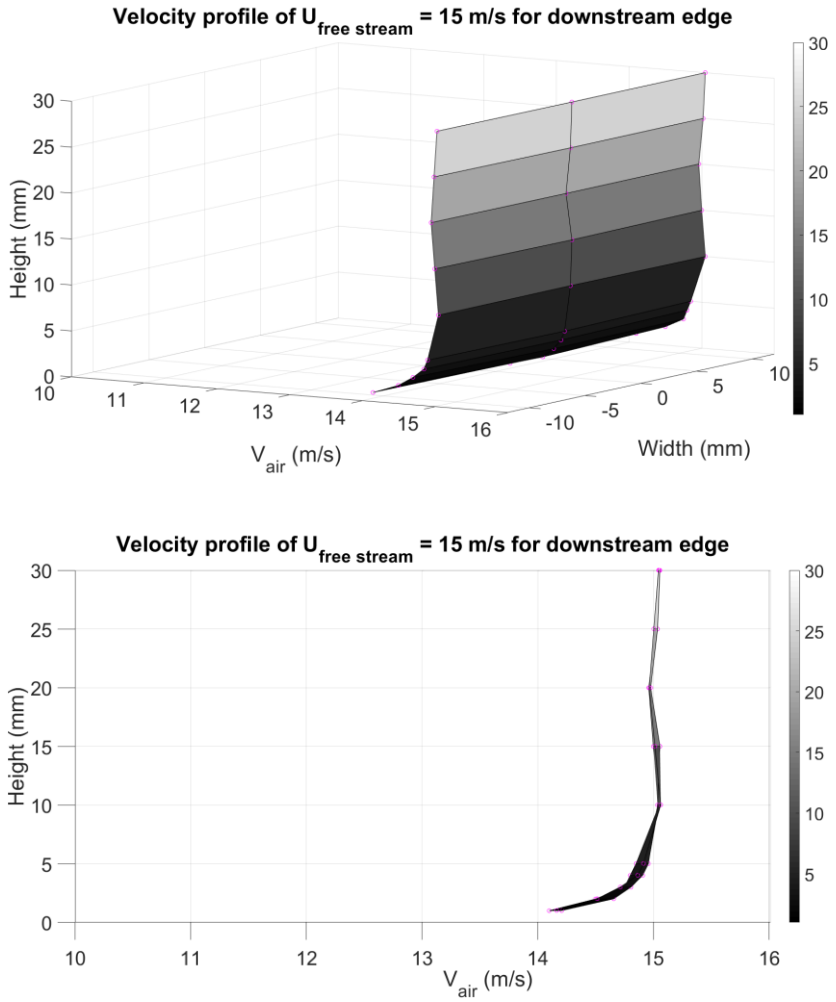

Figure A.1. Characteristic velocity profiles in the different positions of width at the downstream edge of the substrate for the velocity of 15 m/s.

Appendix B: Single-phase convection

Experiments were conducted to validate the applied transient method for measurements. Single-phase convection was performed firstly in the T_{sc} of 0, 5, 10°C and RH of 10% (i.e., considered as dry air) for airflow velocities of 1, 5, 10, 15 m/s to compare the results with the literature. Single-phase HTC is a function of airflow velocity (Re number; calculated using the hydraulic diameter of the test section, free stream velocity and air properties) and thermal properties of the fluid at mean temperature (such as Pr number). The results are plotted in *Figure*

A.2. as Nu versus Re and compared with a well-recommended correlation for turbulent heat transfer from VDI-Wärmeatlas. A good agreement was found with a maximum deviation of 8%. To make sure that the applied methodology is correct, different T_{sc} were tested and since HTC is not function of the T_{sc}, results yielded similar values at the same airflow velocities (as seen in *Figure A.2.*). The reason for the small differences in Nu and Re numbers is that the film temperature was used to estimate fluid properties which vary slightly with T_{sc}.

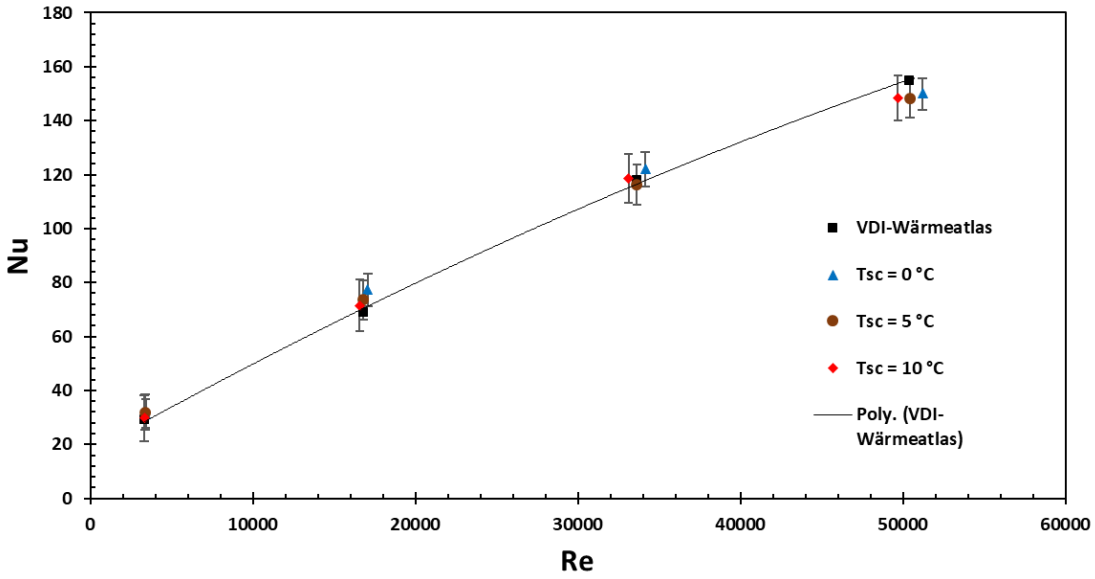

Figure A.2. Nu number of the single-phase convention versus Re number. The results for different airflow velocities and T_{sc} are compared with a well-recommended correlation for turbulent heat transfer from VDI-Wärmeatlas.

Appendix C: Fluctuations in the results

To find the source of the fluctuations in the results for HTC vs. time, Fourier Transform (FFT) and Power Spectral Density (PSD) concepts were used. The FFT is an efficient algorithm used to compute a discrete Fourier transform (DFT). This Fourier transform outputs variation amplitude as a function of frequency which enables the analyzer to understand what is causing the variation. The frequency resolution in an FFT is directly proportional to the signal length and sample rate.

The PSD shows the strength of the variations (energy) as a function of frequency. In other words, it shows at which frequencies variations are strong and at which frequencies variations are weak. The unit of PSD is energy (variance) per frequency (width) and energy within a specific frequency range can be obtained by integrating PSD within that frequency range.

The raw data for the temperature measurements have been analyzed. Among the temperature readings, the ambient temperature is fluctuating as illustrated in *Figure A.3.*. Also, the portion of the result for HTC is provided in *Figure A.4.* as well.

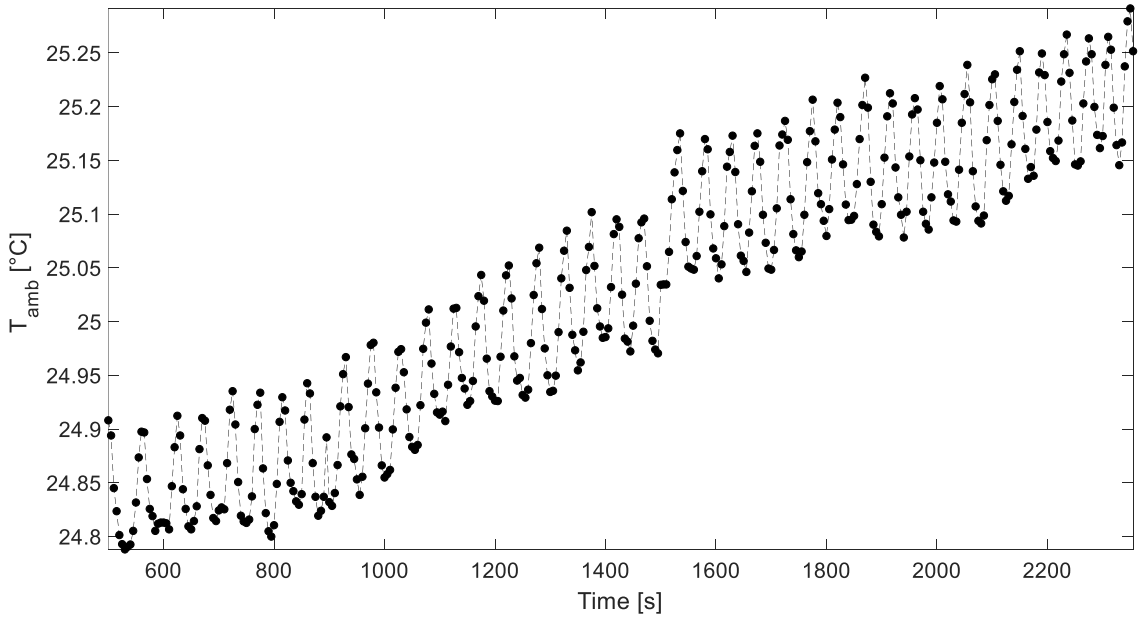

Figure A.3. Ambient temperature versus the time at V=10 m/s, RH=80% and T_{sc}=0°C. The source of fluctuations is adding water to air periodically to control the RH.

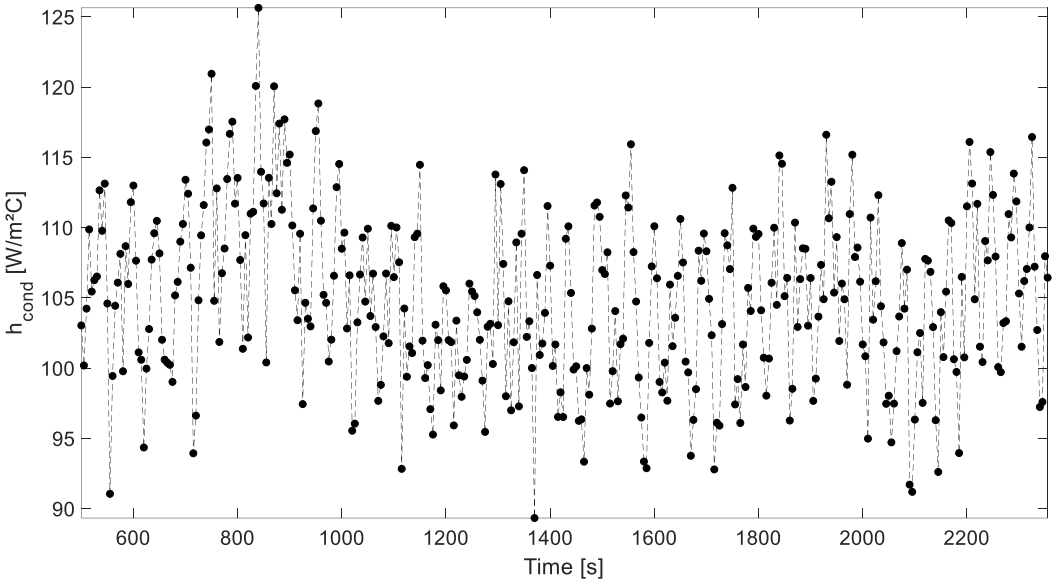

Figure A.4. HTC versus the time at V=10 m/s, RH=80% and Tsc=0°C.

The reason for the fluctuations of ambient temperature is on/off system for controlling RH. There are two ways for increasing relative humidity which are adding water or adding vapour. In the current experimental setup, water was added to control RH using the on/off controller. In the case of adding water to the air without any heat supply, the state of the air follows a constant enthalpy line in the psychrometric chart (*Figure A.5.*) which results in decreasing dry air temperature. Also, the reason for the small increase in the trend of ambient temperature is the heat dissipated from the fan during the experiment.

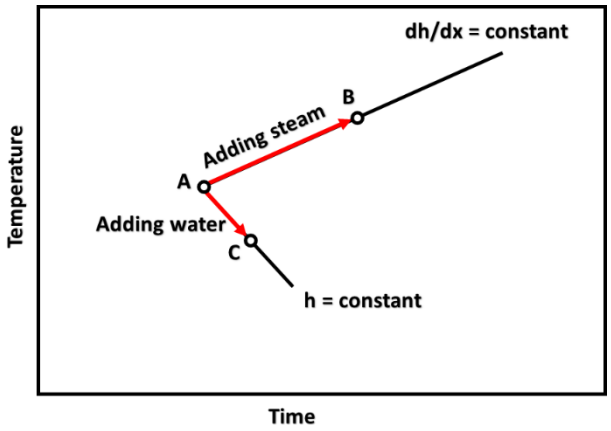

Figure A.5. There are two ways for increasing relative humidity which are adding water or adding vapour. Adding water is h constant process.

PSD was applied for the results of HTC as well as ambient temperature at V=5 m/s, RH=80% and Tsc=0°C to compare the frequency of fluctuations. The PSD plots for both ambient temperature and the HTC are shown at *Figure A.6.*.

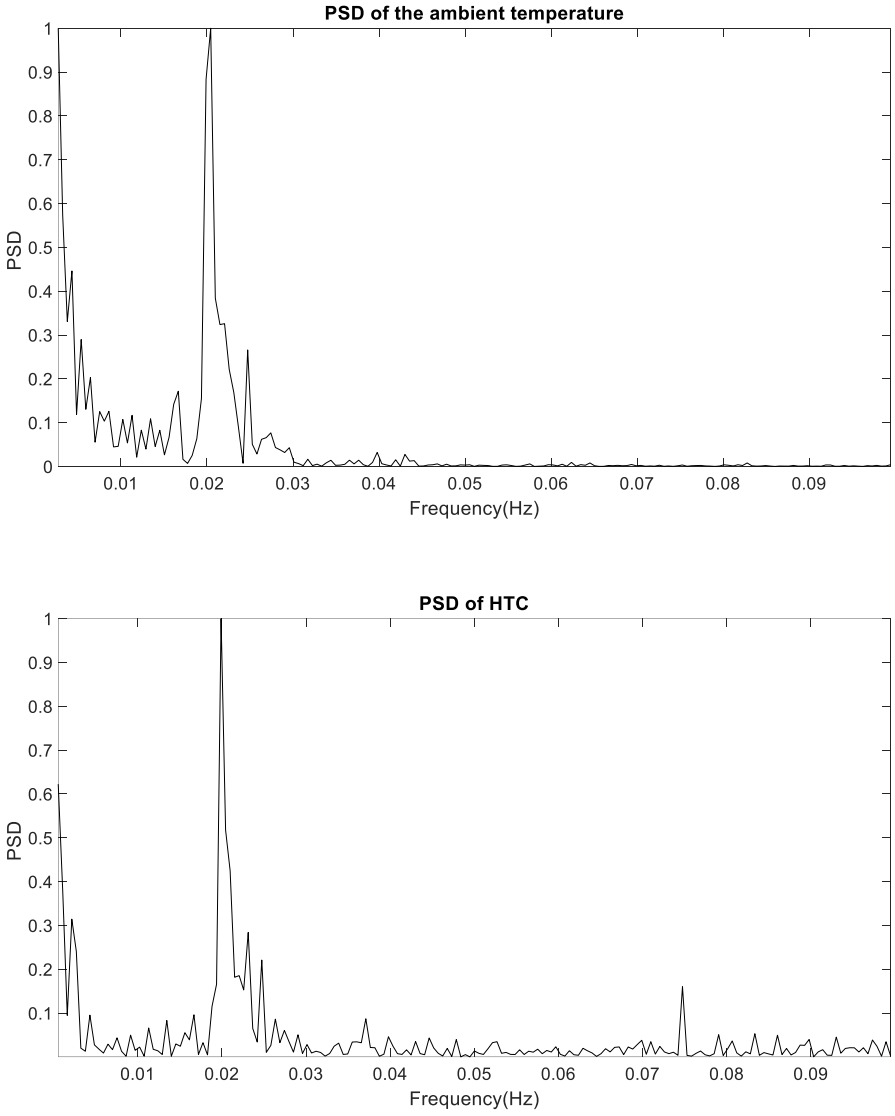

Figure A.6. Comparison of PSD vs frequencies for ambient temperature and HTC. The results showed that both have the same frequency for fluctuation.

As seen in *Figure A.6.*, both raw data for ambient temperature and HTC have the same frequency of 0.02 Hz. It is also consistent with the on/off time for the controller which was approximately 50 s.

Appendix D: Test section

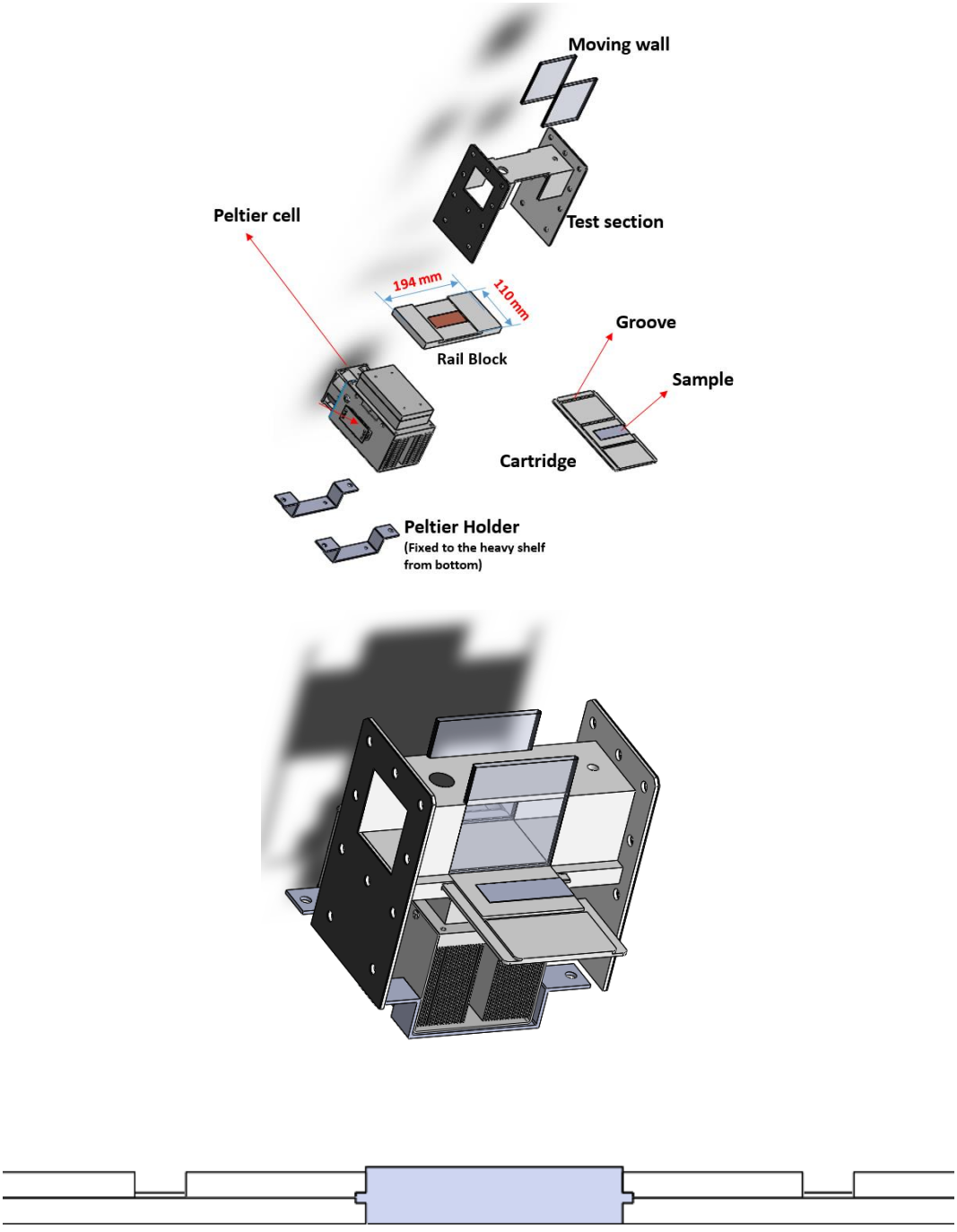

Figure A.7. The system for changing the substrate. This system consists of a test section, sample, cartridge for holding the sample, moving walls, copper block to cool down the sample and Peltier cell. The system was designed to change the substate during flight quickly.

Appendix E: Velocity control system (VCS)

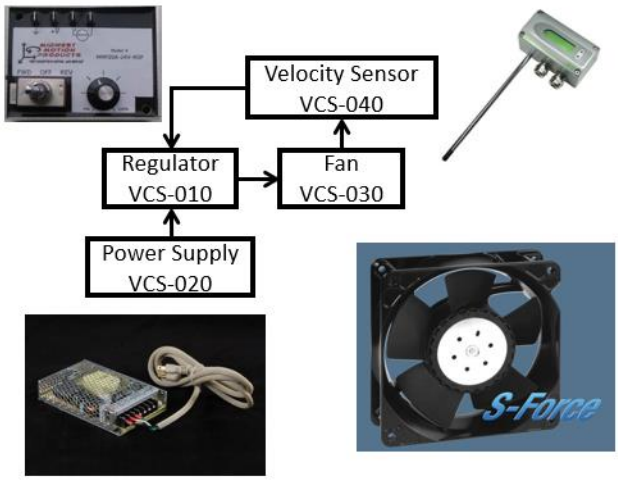

Ref	Items	Function	Related parameter	Expected value	Mass [g]	Power [W]	Remarks
VCS-020	DC Power supply+Regulator	Supply power to fan	Fan power	48V 1.8A	700	N/A	IPS-603-60V-3.5A
VCS-025	Fuse	Protection	N/A	6 A 250VAC 125VDC			AGC 6 Derate at 50% for DC
VCS-030	Axial fan	Create airflow	Droplet shedding	$\leq 30\ m/s$	1600	120	MM1865H24B-FSR
VCS-040	Anemometer	Velocity control	Fan velocity	N/A	<100	0.2	EE75,E+E Elektronik Ges.m.b.H

Figure A.8. Functional diagram of the velocity control system. Connections are necessarily electrical unless specified.

Appendix F: Humidity control system (HCS)

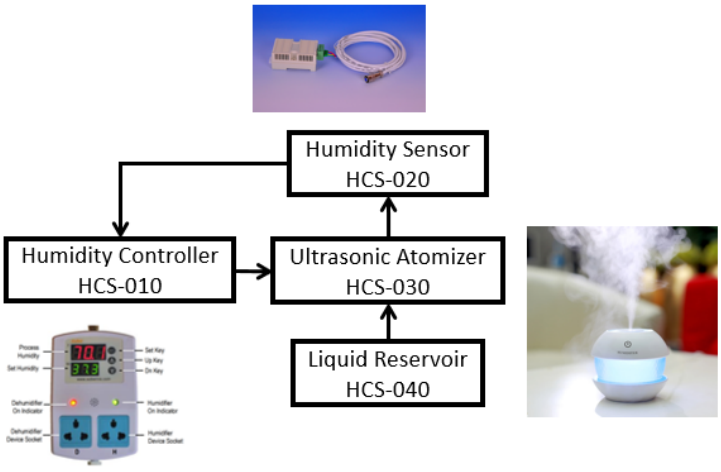

Ref	Items	Function	Related parameter	Expected value	Mass [g]	Power [W]
HCS-010	Humidity controller	On/off control. Humidifying	To control the HCS-030	N/A	200	
HCS-020	Humidity sensor	Measure relative humidity	Input data to HCS-10	N/A	50	<1
HCS-030	Ultrasonic atomizer	Produce water vapour	Increase relative humidity	450 ml/hr	230	2
HCS-040	Water reservoir	Store water	Supply water to the ultrasonic atomizer by capillary wick	200 mL	1000	N/A

Figure A.9. Functional diagram of the humidity control system. Connections are necessarily electrical unless specified.

Appendix G: Temperature control system (TCS)

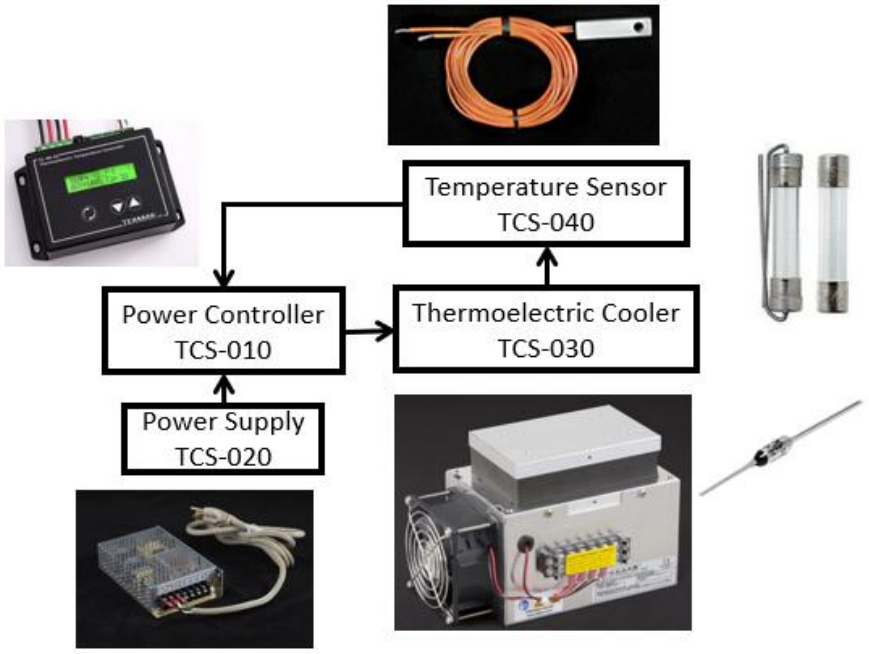

Ref	Items	Function	Related parameter	Expected Value	Mass [g]	Power [W]	Remarks
TCS-010	Power controller	Control power to thermoelectric unit	Control cold side temperature of Peltier cell	N/A	600	1.8	TETech TC-48-20
TCS-020	DC power supply	Supply power to the thermoelectric unit and hot side fan	Surface temperature of samples	24V 6.5A	600	N/A	TETech PS-24-6.5A
TCS-025	Fuse	Protection	N/A	10 A 250VAC 125VDC	NA	N/A	AGC-10 Derate at 50% for DC
TCS-030	Thermoelectric cooler	Control interface temperature	Surface temperature of samples	$\Delta Q \leq 61\ W$	2300	140	TETech CP-061HT
TCS-040	Thermistor	Temperature feedback	Surface temperature of samples	0°C	< 10	N/A	TeTech MP-3193
TCS-050	Thermal fuse	Prevent overheating	Temperature control	Max 50°C	< 10	N/A	Selco SWTC-171-3535

Figure A.10. Functional diagram of the temperature control system. Connections are necessarily electrical unless specified.

Appendix H: Droplet injection system

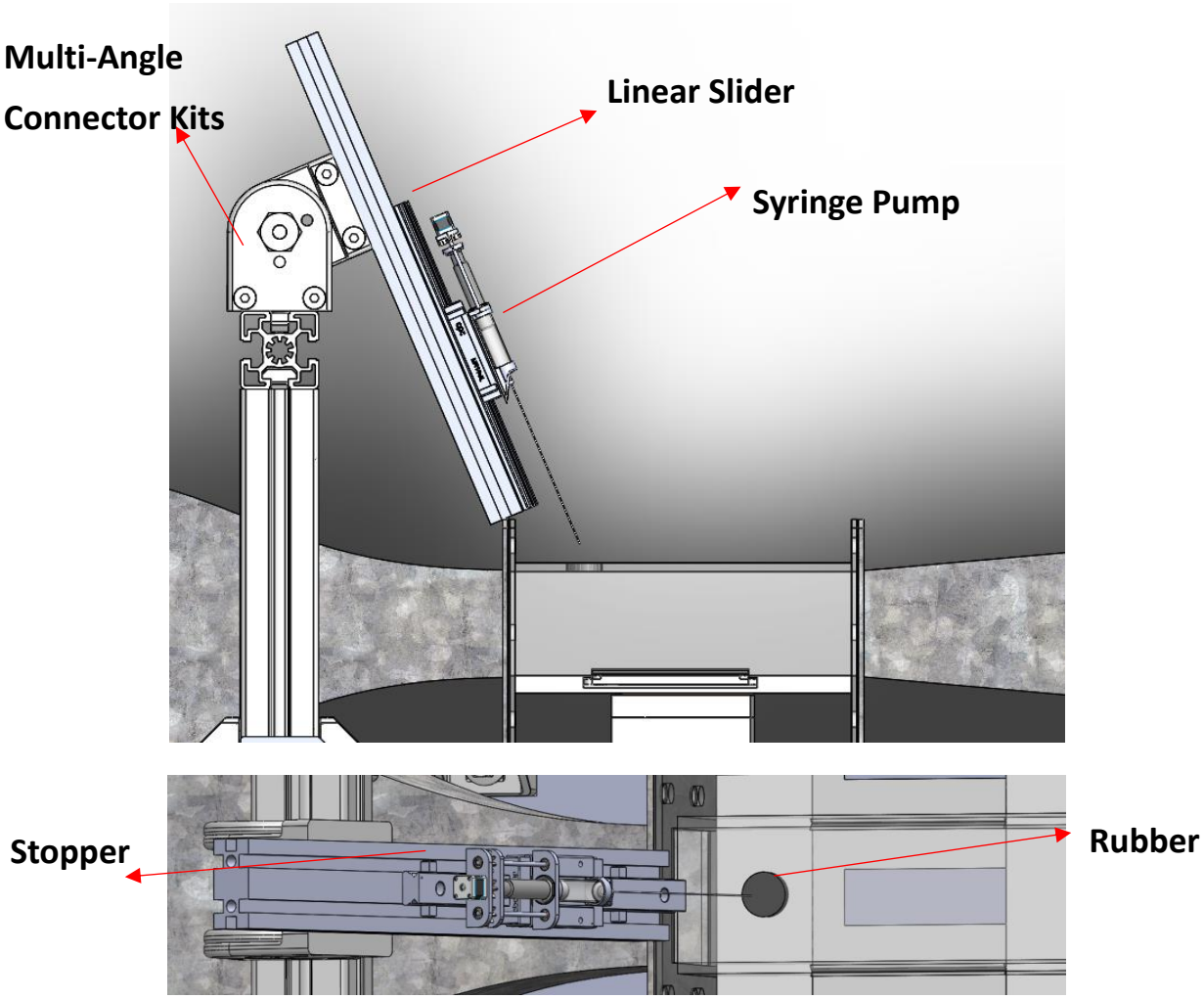

Figure A.11. Diagram of the droplet injection system. This system was designed to deposit a droplet on the surface in a condensation environment. It consists of a syringe and linear slider to deposit a drop in the test section and leave it.